Neutral Beam Excitation of Alfvén Continua in the Madison Symmetric Torus Reversed Field Pinch

by

Jonathan Jay Koliner

A dissertation submitted in partial fulfillment of

the requirements for the degree of

Doctor of Philosophy

(Physics)

at the

University of Wisconsin – Madison

2013

Defended on 22 October 2013

Dissertation approved by the following members of the Final Oral Committee:

Cary Forest · Professor of Physics

John Sarff · Professor of Physics

Jan Egedal · Professor of Physics

Paul Terry · Professor of Physics

Carl Sovinec · Professor of Engineering Physics

Abstract

Alfvén continua and Alfvén eigenmodes (AEs) have been generated for reversed-field pinch (RFP) plasma equilibria in Madison Symmetric Torus (MST). Data gathered from the extensive suite of diagnostics on MST was used to generate equilibria using MSTFIT and VMEC. Three dimensional equilibria for spontaneous helical states were generated using the equilibrium reconstruction code V3FIT. The reduced-MHD codes AE3D and STELLGAP were run on all generated equilibria to calculate the continua and AEs. All continuum solutions contain a toroidicity-induced Alfvén gap at $200 - 400$ kHz, within which AE solutions appear by coupling of $m = 0, 1$ at medium n.

The first observation of beam-driven instabilities on the RFP was performed using MST magnetics during neutral beam injection (NBI). Spatially coherent bursts with $n = 5, m = 1$ were observed in plasmas with edge safety factor $q_a = 0$. The bursts oscillate at 65 kHz, and reach maximum amplitude and decay away within 100 μs. These bursts persist for the duration of NBI. Secondary $n = -1$ and $n = 4$ bursts are coupled in time, reaching maximum amplitude with 50 μs after the $n = 5$ peak amplitude. While the $n = 5$ bursts scale weakly with the electron density n_e and strongly with the beam velocity v_{beam}, the $n = 4$ bursts scale with the Alfvén speed v_A. The burst frequencies are well below those of the calculated AEs and the modes are driven even with $v_{\text{beam}} < v_A$, suggesting that the bursting modes are EPMs exciting continuum resonances.

Burst characteristics were examined in a variety of plasmas. In reversed plasmas, the temporally changing q profile changes the burst resonances, bringing $n = 6$ into resonance halfway through the sawtooth cycle. The $n = 5$ mode switches from its frequency in non-reversed plasmas to a higher frequency at the end of the sawtooth cycle. In deeply reversed plasmas, the bursts are weaker and display chirping behavior as the plasma reversal increases. During the transition to a helical state, the bursts increase in frequency as q on-axis changes, altering the parallel wavenumber $k_{\|}$. When the helical state is established, the bursts terminate.

Acknowledgements

I would like to sincerely thank all of the people who took time to make this work possible. Firstly, thank you to Cary Forest for being patient with me as my work spun off on a tangent from our initial plans. I wasn't always communicative, but I appreciate the freedom with which I was able to pursue the topics that interested me.

Thank you to John Sarff, Brett Chapman, Karsten McCollam and Jay Anderson for your guidance and support at various points along my graduate career. Without your help and experience I surely would not have completed the projects I started.

Thank you to Liang Lin, whose interest and insight lent my initial observations so much more credibility than they would have had on their own. I learned something every time I talked to you, and we talked quite a bit.

To Don Spong and Jim Hanson, thank you both for hosting me and teaching me to run your respective codes. Auburn and Oak Ridge stand out as truly positive moments in my graduate career, and our discussions guided the future of my research. Your sustained interest and support after I left kept me afloat at times when I got stuck.

To the beam group, including Josh Reusch, Deyong Liu, Jeff Waksman, and Mark Nornberg, thank you for making my work possible. You dealt with the intricacies and frustrations of the neutral beam so that I could focus on the wonderful waves it was generating. You ran the beam many days in that unpleasant beam control room for my experiments, and you have my deepest thanks for that.

To the MST group in general, scientists and graduate students alike, thank you for the passing conversations, for your interest in my subject, and for keeping the machine running so I could do this work. I will be sad to have to leave such an excellent working environment with so many great minds.

Thank you Tracey Holloway for giving me the opportunity to dip into the world of sustainability for a year. I not only learned a lot, but I was kept sane through my discussions with you and through instructing the students of our class. I think we made a great course and I had fun doing it.

To my officemates, Noam Katz, Kian Rahbarnia, Chris Cooper and James Titus, thank you for making my time at work so much more fun. I spent a year in that office alone, and while it's nice to have your own office, I preferred it with you guys in it. Thank you for not kicking me out due to the eyesore that is my desk.

To Matt Billmire, Ian Ross, Doug Diamond, Scott Eilerman and Zak Walter, thank you for making my time in Madison so awesome. Even if my PhD had no impact on my career prospects or my skills, my time here would have been worth it because I was surrounded by wonderful people. Gaming, beer, frisbee, soccer and food have never been in short supply thanks to you guys, and that has kept me going.

Finally, thank you to my lovely little family. Quinn, you're a terrible dog sometimes, but your friendship has been consistent and abundant, and I wouldn't trade you for even the most well-behaved, purebred dog. Lennox, you may not have given me any extra time, but you sure gave me motivation. It's easier to do the work that needs to be done when I'm doing it for you. Sara, Spearmint, my wonderful wife, thank you for all of your patience and love. You've got your own stuff to do, but you made it work to support my extremely unhealthy work and study habits while I hammered this dissertation out. Thank you for being there and for being mine. It's probably my turn to hold the baby.

Contents

Abstract i

Acknowledgements iii

List of Figures **viii**

List of Tables **xi**

1 Introduction **1**

1.1 Outline 3

1.2 Plasma Equilibria 5

1.3 Alfvén Eigenmodes and Energetic Particle Modes 8

1.4 Madison Symmetric Torus 15

1.4.1 Tearing Modes and Sawtooth Events 19

1.4.2 Neutral Beam Injector 22

2 Relevant Diagnostics for Mode Analysis and Equilibrium Reconstruction **26**

2.1 Magnetics 27

2.1.1 Magnetic Arrays 27

2.1.2 Dense Array and Probes 34

2.1.3 Single Loops 35

2.2 Passive Diagnostics 37
2.2.1 Soft X-Ray (SXR) 37
2.2.2 D-Alpha Array 40
2.2.3 Advanced Neutral Particle Analyzer 41
2.3 Laser and Wave-based Diagnostics 43
2.3.1 Far Infra-Red Interferometer-Polarimeter 43
2.3.2 CO2 Interferometer 46
2.3.3 Thomson Scattering 47
2.4 Particle Beam Diagnostics 51
2.4.1 Charge Exchange Recombination Spectroscopy and Diagnostic Neutral Beam 51
2.4.2 Motional Stark Effect 54
2.4.3 Rutherford Scattering 56
2.4.4 Heavy Ion Beam Probe 58
2.5 Summary 60

3 Equilibrium Reconstruction **62**
3.1 History of Equilibrium Reconstruction on MST 63
3.2 Variational Moments Equilibrium Code (VMEC) 64
3.2.1 Modifications for the RFP 65
3.2.2 AE3D and STELLGAP 66
3.3 3D Equilibrium Reconstruction 72
3.3.1 Newcomb Toroidal Code 74
3.3.2 V3FIT 76
3.4 Summary 86

4 Alfvén Eigenmodes and Continua **87**

4.1 Methodology . . . 88
4.2 Axisymmetric Continua and Eigenmodes . . . 89
4.2.1 Non-Reversed Plasmas . . . 90
4.2.2 Standard Plasmas . . . 93
4.2.3 Deeply Reversed Plasmas . . . 96
4.2.4 Summary . . . 98
4.3 Three Dimensional Continuum and Eigenmodes . . . 99
4.3.1 V3FIT Equilibrium Reconstruction Results . . . 99
4.3.2 3D Alfvén Continuum and AEs . . . 106
4.4 Summary . . . 108

5 Characteristics of observed Alfvénic modes 109
5.1 Numerical Methodology . . . 110
5.1.1 Fourier Transform of Array Data . . . 111
5.1.2 Wavelet Transform of Time Series . . . 113
5.1.3 Event Tagging and Analysis . . . 118
5.2 Burst Characteristics, Scaling, and Prevalence . . . 120
5.2.1 Non-Reversed Plasmas . . . 120
5.2.2 Standard Reversed Plasmas . . . 130
5.2.3 Deeply Reversed Plasmas . . . 134
5.2.4 Helical Plasmas . . . 134
5.3 Macroscopic Effects on MST Plasmas . . . 138
5.4 Internal Characteristics . . . 142
5.5 Summary . . . 144

6 Conclusion 146

Bibliography **149**

List of Figures

1.1 Cylindrical flux surface picture 6
1.2 Helical flux surface picture 8
1.3 Alfvén continuum in a cylinder 11
1.4 TAE gap in the Alfvén continuum 13
1.5 Energy decrease by flattening of the distribution function 14
1.6 Inverse Landau damping by bump-on-tail distribution 15
1.7 Resonant drive by a fast ion spatial gradient 16
1.8 Madison Symmetric Torus 17
1.9 Magnetic field and safety factor profiles 18
1.10 Iron core transformer inducing electric field 19
1.11 Typical MST discharge 20
1.12 MST islands and stochastic fields 21
1.13 The Neutral Beam on MST 23
1.14 Fast ion distribution from 2 ms of beam injection 23
1.15 Fast ion guiding center overlaying MST field lines 24
1.16 Fast ion and plasma safety factor 25

2.1 Array coil forms and graphite covers 28
2.2 MST Magnetic Arrays 30

2.3 Coil form offsets on MST . . . 31
2.4 Toroidal array coil gains . . . 33
2.5 Rogowski loop diagram . . . 36
2.6 Old and new SXR camera viewing chords . . . 38
2.7 Advanced Neutral Particle Analyzer layout . . . 42
2.8 FIR layout . . . 46
2.9 Thomson scattering off of an electron . . . 48
2.10 Thomson scattering system layout . . . 49
2.11 Diagram of the DNB . . . 53
2.12 A diagram of the DNB and MSE views . . . 55
2.13 Rutherford scattering set-up on MST . . . 57
2.14 Heavy Ion Beam Probe mock-up . . . 59
2.15 Heavy Ion Beam Probe on MST . . . 60

3.1 Axisymmetric VMEC and MSTFIT comparison . . . 67
3.2 Stellgap before and after fixing Jacobian . . . 69
3.3 Example Alfvén continuum mode . . . 72
3.4 Example TAE structure . . . 73
3.5 SXR emissivity compared to NCT-SHEq equilibrium . . . 74
3.6 $\bar{n}_e$ from FIR Interferometry compared to NCT-SHEq equilibrium. . . . 75
3.7 Helical plasma core in a diagram of MST . . . 82
3.8 Diagram of diagnostic and mode rotation before running V3FIT . . . 83
3.9 Flux surfaces closed by the conducting shell . . . 84
3.10 B_θ offset from MSTFIT Green's Tables . . . 85

4.1 300 kA $q_a = 0$ Alfvén continuum . . . 89
4.2 $q_a = 0$ Alfvén continuum, $n = 5$ at multiple I_p . . . 90

4.3 300 kA $q_a = 0$ Alfvén continuum, $n = 5$ at multiple $\bar{n}_e$ 91

4.4 300 kA $q_a = 0$ Alfvén continuum, $n = 5$ at multiple q_0 92

4.5 $n = 4$ through $n = 8$ TAE structures for 300 kA $q_a = 0$ case 93

4.6 400 kA $q_a = -0.06$ Alfvén continuum, with $q_0 = 0.205$ 94

4.7 400 kA $q_a = -0.06$ Alfvén continuum, with $q_0 = 0.18$ 95

4.8 $n = 4$ through $n = 6$ TAE structures in the 400 kA $q_a = -0.06$ case . . . 95

4.9 300 kA $q_a = -0.15$ Alfvén continuum for $q_a = -0.15$ 96

4.10 q profile during PCCD 97

4.11 $n = 5$ through $n = 6$ TAE structures in the 300 kA $q_a = -0.15$ case . . . 98

4.12 Example parameterized profile with a 5-point spline 100

4.13 Last closed flux surface variables in VMEC 102

4.14 Comparison of p and q for two SHAx cases 104

4.15 Flux surfaces generated by V3FIT reconstruction 105

4.16 Output $n_e(s)$ and $\epsilon(s)$ mapping to flux surfaces from V3FIT 105

4.17 V3FIT synthetic vs. measured values for Interferometer-Polarimeter measurements 106

4.18 500 kA $q_a = 0$ Alfvén continuum with SHAx 107

4.19 $n = 5$ and $n = 6$ TAEs in a 500 kA $q_a = 0$ plasma with SHAx 108

5.1 The Morlet wavelet with differing scale and wavenumber 116

5.2 Wavelets of $n = 4$ and $n = 5$ bursts in the base case 121

5.3 A single burst resolved into n components 122

5.4 Time evolution of $\dot{B}$ on all coils during a burst 123

5.5 Burst amplitudes resolved by m and n 125

5.6 Scaling of the $n = 5$ frequency with magnetic field and density 126

5.7 Scaling of the $n = 5$ bursts with v_{beam} 126

5.8 Scaling of the $n = 5$ and $n = 4$ bursts with v_A 127
5.9 $q_a = 0$ continuum calculation with burst frequencies marked 128
5.10 Mechanism of excitation: multiple flattenings 129
5.11 q profile evolution during the sawtooth cycle 131
5.12 Wavelets of $n = 5$ and $n = 6$ bursts in a standard plasma 132
5.13 $q_a = -0.06$ continuum calculation with burst frequencies marked 133
5.14 Wavelets of $n = 5$ and $n = 6$ bursts in a deeply reversed plasma 135
5.15 Fast ion confinement time vs. the helical mode amplitude. 136
5.16 Wavelet of $n = 5$ bursts in a plasma transitioning into SHAx 137
5.17 Core tearing mode ($n = 5$) amplitude and velocity during NBI 139
5.18 Ensemble of bicoherence, ANPA signal and tearing mode amplitude during bursts 140
5.19 Burst limit cycle at two beam currents 141
5.20 Ensembled interferometry and polarimetry measurements of the $n = 5$ mode structure 143
5.21 Interferometry measurements of burst locations in time 144

List of Tables

1.1 MST Parameters 16
1.2 MST NBI Parameters 22

2.1 Toroidal and Poloidal Array locations 32

2.2 MST Equilibrium Reconstruction Diagnostics 61

2.3 MST Alfvén wave Diagnostics 61

3.1 V3FIT and VMEC parameters 79

Chapter 1

Introduction

In order to achieve sustained fusion, a hot, dense plasma must be confined for long enough to begin self-heating. Although simply stated, this goal is tremendously difficult in practice because plasma is a reactive and dynamic medium. Powerful magnetic fields in a torus can confine plasmas, but large scale collective processes such as plasma waves and small scale local processes such as particle collisions can work against confinement. Fluid dynamics, electromagnetism and particle kinetics conspire in often unexpected ways to confound efforts at achieving a burning plasma. Nonetheless, for 60 years plasma physicists have been steadily improving plasma confinement as they build new machines.

Sometimes the plasma processes work in favor of confinement, offering a clear way forward for researchers. The "bootstrap current" that is crucial in tokamaks is one example [1]. Subsequent tokamak design efforts sought to maximize this effect so that less external current drive was necessary.

The reversed-field pinch (RFP) configuration was likewise stumbled upon. In 1974, six years after the ZETA pinch was shut down, analysis of its ramp-down phase led to the realization that its confining magnetic fields had self-organized [2]. The plasma had determined its own stable equilibrium, and it was drastically different than the equilibrium the researchers had planned for. In this new equilibrium, the toroidally-oriented field reverses direction, possessing opposite chirality in the interior and at the edge of the plasma. In this configuration, the plasma is in a minimum energy state where the lines of current are aligned with the internal magnetic fields. The plasma-generated field significantly reduces the need for external field generation. From analysis of the "off" phases of a machine that been shut-down for six years, a new type of plasma confinement device was born.

At the time of writing, Madison Symmetric Torus (MST), an RFP, has the fourth largest magnetic confinement program in the United States. The three largest experiments are tokamaks. The first RFP devices aimed at plasma confinement were constructed in the late 1970's, and the RFP community has been working to replicate stellarator and tokamak advances in the context of the configuration's unique field structure. RFP research has benefitted significantly from collaboration and discussion with the greater magnetic confinement community, but many gaps exist. The relatively small amount of resources available have been used to study the properties of this fascinating equilibrium, dividing the focus of research between interesting basic physics and fusion-relevant experiments.

The first neutral beam injection (NBI) system for current drive and heating was installed and operated in 1972 [3], five years before the first RFP finished construction. The first such system on an RFP was installed in 2010 on MST [4]. As such, beam-driven instabilities arising from the presence of a small fast ion population are one area where the tokamak and stellarator communities have performed considerably more research than the RFP community [5, 6]. This research is highly relevant to fusion reactors as beam ions may interact with the plasma in a similar manner to fusion-produced alpha particles. In fact, the ratio of the MST fast ion orbit size to the machine size was chosen to be comparable to these fusion-produced particles in a reactor. The instabilities are often resonant interactions determined by the distribution of fast ions and the geometry of the magnetic fields in the equilibrium. Because the field direction is crucial to determination of the excited waves, the uniqueness of the RFP configuration precludes the immediate application of knowledge gained from other machines.

The pitch of the magnetic fields around the machine axis changes with the distance from the axis. The inverse shear length quantifies the degree to which the pitch changes. As expected, the RFP has a significantly larger inverse shear length than tokamaks and stellarators. High shear tends to eliminate instabilities by shrinking the domain of a given resonant interaction. What the eigenmodes of an RFP look like has been an open question in plasma physics. Moreover, whether beams can drive large instabilities in such high shear conditions has also been unknown.

This thesis addresses both the question of the continuum and eigenmode structures in RFP plasmas, and whether beam-driven instabilities exist. It presents the first observation of beam-driven Alfvén waves in the RFP, performed on Madison Symmetric Torus.

1.1 Outline

The remainder of Chapter 1 presents background necessary to interpret the presented results and discussion. The basics of plasma equilibria, Alfvén eigenmodes and energetic particles modes, and the overall configuration of the MST experiment are presented.

Chapter 2 describes the plasma diagnostics that are relevant both for analysis of high frequency waves and for equilibrium reconstruction. Diagnostics are divided into several categories and evaluated based on their relevance for these two tasks. Particular attention is paid to the magnetic diagnostics, whose properties have not been catalogued in one place prior to this work. The intent of this section is both to set up the necessary understanding for later results, and to compile a sufficient summary of relevant diagnostics for future researchers to continue the studies presented here. *Section 2.1.1 contains a table with the location of probes in the magnetic arrays. Section 2.5 contains a table that summarizes the locations of diagnostics relevant to equilibrium reconstruction.*

Chapter 3 describes the methods used to perform 3D equilibrium reconstructions and to determine the Alfvén resonances on MST. VMEC and V3FIT, the equilibrium solver and reconstruction code, respectively, are introduced. The Alfvén continuum solver STELLGAP and the Alfvén eigenmode solver AE3D are described.

Chapter 4 catalogues the Alfvén continua and eigenmodes for many MST plasma equilibria. The non-reversed base case is examined with varied parameters. Continuum solutions for reversed and deeply reversed cases are presented. Finally, continuum solutions for helical plasmas are shown. *In Section 4.2, continuum solutions and eigenmodes for a wide variety of MST plasmas are presented. In Section 4.3.1, the first fully 3D equilibrium reconstruction results are presented. In Section 4.3.2, continuum solutions corresponding to these results are shown.*

Chapter 5 deals with the observation of bursting modes during discharges with NBI. The computational algorithm used to resolve high frequency periodic bursts is described. The first observation of beam-driven instabilities in an RFP are presented. Results from non-reversed operation, including magnetic polarization and frequency scaling are shown. Finally, the internal characteristics of the bursting modes and the relevance to MST plasmas is connected. A discussion of the identity of the modes follows. *In Section 5.2.1, time-spectrograms showing the first observation of magnetic* *bursts due to beam injection are shown. In the following sections, various related bursts of interest are presented.*

1.2 Plasma Equilibria

A plasma is in magnetohydrodynamic (MHD) equilibrium when its magnetic field and pressure profiles are static [7]. In other words, a plasma is in MHD equilibrium when it is neither expanding nor contracting. A physical description of such a state follows, informed heavily by the Miyamoto text, *Controlled Fusion and Plasma Physics* [8].

In a given fluid element, no electric fields $\mathbf{E}$ and no local velocities $\mathbf{V}$ can exist to satisfy this condition in the simplest case. In practice, global flows are often present. The equation of motion for fixed element in a magnetofluid is

$$\rho_m \left(\frac{\partial \mathbf{V}}{\partial t} + (\mathbf{V} \cdot \nabla) \mathbf{V} \right) = -\nabla p + \mathbf{j} \times \mathbf{B}, \tag{1.1}$$

where ρ_m is the plasma mass density, $\mathbf{V}$ is the velocity of a fluid element, p is the pressure, $\mathbf{j}$ is the current density vector, and $\mathbf{B}$ is the magnetic field vector. On the left-hand side is the rate of change of momentum of the fluid element, which in the fixed frame of reference must include a spatial gradient $(\mathbf{V} \cdot \nabla) \mathbf{V}$. The right-hand side includes the forces due to a pressure gradient and Ohm's law. Setting $\mathbf{V} = 0$ satisfies the equilibrium condition, resulting in

$$\nabla p = \mathbf{j} \times \mathbf{B}. \tag{1.2}$$

This is the fundamental force balance equation for equilibrium. The addition of Ampère's Law,

$$\nabla \times \mathbf{B} = \mu_0 \mathbf{j}, \tag{1.3}$$

Gauss's Law for magnetism,

$$\nabla \cdot \mathbf{B} = 0$$

Figure 1.1: Visualization of cylindrical flux surface coordinates and plasma quantities

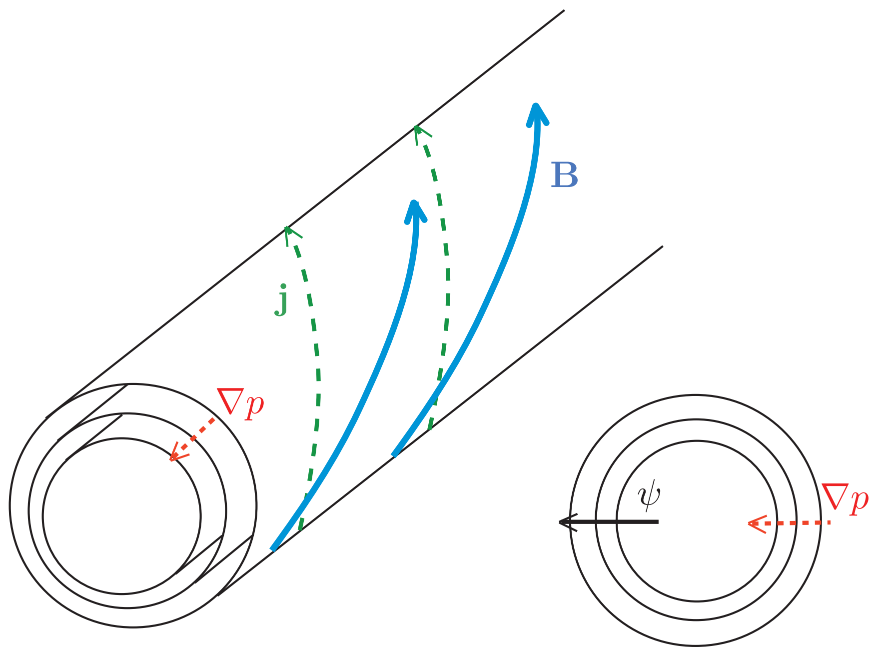

and the time-invariant continuity equation for current density,

$$\nabla \cdot \mathbf{j} = 0$$

complete the picture for a plasma in equilibrium. The cross product in Eq. 1.2 implies that the pressure gradient is perpendicular to both the magnetic field and the current density everywhere. This does not imply that $\mathbf{B}$ and $\mathbf{j}$ are perpendicular to each other, but it does imply that they lie parallel to a surface of constant pressure. A plasma in equilibrium consists of a set of surfaces of constant pressure, parallel to which lie the magnetic field lines and current density lines, Fig. 1.1.

The surfaces as determined by Eq. 1.2 are surfaces of constant ψ, where

$$(\nabla\psi) \cdot \mathbf{B} = 0. \tag{1.4}$$

In a torus with cylindrical coordinates such that $\psi = \psi(R, \phi, Z)$, where Z is normal to the hole in the torus, the magnetic field components are determined by $\mathbf{B} = \nabla \times \mathbf{A}$,

$$\begin{aligned} B_R &= \frac{1}{R}\frac{\partial A_Z}{\partial \phi} - \frac{\partial A_\phi}{\partial Z} \\ B_\phi &= \frac{\partial A_R}{\partial Z} - \frac{\partial A_Z}{\partial R} \\ B_Z &= \frac{1}{R}\frac{\partial}{\partial R}(RA_\phi) - \frac{1}{R}\frac{\partial A_R}{\partial \phi}. \end{aligned} \tag{1.5}$$

An equilibrium that is invariant in the ϕ direction, $\partial/\partial\phi = 0$, is called axisymmetric or two-dimensional. In that case,

$$\psi(R, Z) = RA_\phi(R, Z). \tag{1.6}$$

A helically symmetric system has some helical pitch α, such that $\psi = \psi(R, \phi - \alpha Z)$. The solution in this case is

$$\psi(R, \phi - \alpha Z) = A_Z(R, \phi - \alpha Z) + \alpha R A_\phi(R, \phi - \alpha Z). \tag{1.7}$$

In the axisymmetric case, the surfaces are a nested set of toruses. In the helical case, the nested surfaces are noncircular and have a rotational transform, Fig. 1.2. The value of ψ scales directly with amount of flux through two types of surface. The first is a two dimensional surface in the (R, Z) plane, through which B_ϕ passes. ψ_t defined by this flux is referred to as the toroidal flux function. The second is an annulus in the (R, ϕ) plane whose ring begins at the magnetic axis (the point of zero flux) and extends outward radially. B_Z passes through this surface, and ψ_p is then referred to as the poloidal flux function.

The determination of flux surface locations is performed by solving Eq. 1.2 according to the constraints provided. $\mathbf{j} \times \mathbf{B}$ is recast as $\frac{1}{\mu_0}\nabla \times \mathbf{B} \times \mathbf{B}$ using Eq. 1.3, resulting in a differential equation that can be solved iteratively. In the axisymmetric case, the Grad-Shafranov equation is arrived at by examining the radial component of this force balance[9]. In the case of a plasma with helical symmetry in a torus,

Figure 1.2: Visualization of helical flux surface coordinates and plasma quantities

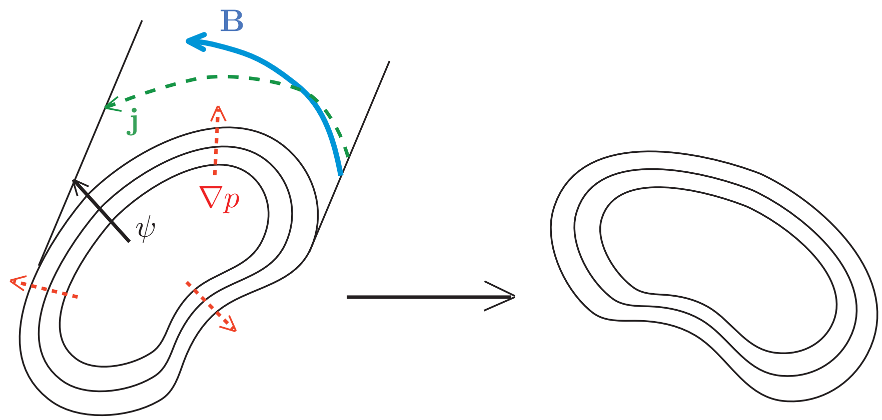

an analytical solution can be found, but does not approximate most real systems well[10].

1.3 Alfvén Eigenmodes and Energetic Particle Modes

The shear Alfvén wave is a fundamental plasma wave that propagates along a magnetic field line, with perturbed **B** and **E** components perpendicular to the field [11]. From Faraday's Law and Ampère's Law,

$$\nabla \times \mathbf{E} = -\frac{\partial \mathbf{B}}{\partial t}$$

$$\nabla \times \mathbf{B} = \mu_0 \left(\mathbf{J} + \epsilon_0 \frac{\partial \mathbf{E}}{\partial t} \right),$$

the well-known wave equation can be constructed,

$$\nabla \times \nabla \times \mathbf{E} = -\nabla \times \dot{\mathbf{B}} = -\mu_0 \left(\frac{\partial \mathbf{J}}{\partial t} + \epsilon_0 \frac{\partial^2 \mathbf{E}}{\partial t^2} \right). \tag{1.8}$$

We care about the perturbed quantities, so $\mathbf{E} \to \tilde{\mathbf{E}}$, $\mathbf{J} \to \tilde{\mathbf{j}}$. We choose $\mathbf{k} \parallel \mathbf{B}_0$ for an incompressible shear wave, and assume $\tilde{\mathbf{E}}$ is linearly polarized and $\tilde{\mathbf{E}} \perp \mathbf{k}$, $\tilde{\mathbf{E}} \perp \tilde{\mathbf{B}} \perp \mathbf{k}$.

Linearizing the equation by assuming fluctuating quantities $\tilde{\mathbf{u}} = \tilde{\mathbf{u}} \exp\left[i\mathbf{k}\cdot\mathbf{x} - \mathbf{i}\omega\mathbf{t}\right]$ replaces $\nabla \to i\mathbf{k}$, $\partial/\partial t \to -i\omega$. The result is

$$-\mathbf{k}\left(\mathbf{k}\cdot\tilde{\mathbf{E}}\right) + k^2\tilde{\mathbf{E}} = \frac{\omega^2}{c^2}\tilde{\mathbf{E}} + \frac{i\omega}{\epsilon_0 c^2}\tilde{\mathbf{j}}. \tag{1.9}$$

Solving along the direction of $\tilde{\mathbf{E}}$ with $\tilde{j} = q_i n_0 \tilde{v}_i$, this equation becomes

$$\epsilon_0\left(\omega^2 - c^2k^2\right)\tilde{E} = -i\omega n_0 e\tilde{v}_i, \tag{1.10}$$

where the ion motion can be shown to be dominant and the electrons follow due to charge neutrality. $\tilde{v}_i$ is found by solving the ion equation of motion for an electromagnetic perturbation in a uniform magnetic field,

$$m_i\frac{\partial\tilde{\mathbf{v}}_i}{\partial t} = e\tilde{\mathbf{E}} + e\tilde{\mathbf{v}}_i \times \mathbf{B}_0 \tag{1.11}$$

which results in

$$\tilde{v}_i = \frac{ie}{m_i\omega}\tilde{E}\left(1 - \frac{\omega_{ci}^2}{\omega^2}\right)^{-1}, \tag{1.12}$$

where $\omega_{ci} = eB/m_i$. The velocity perturbation parallel to $\tilde{\mathbf{B}}$ contains information about the $\mathbf{E}\times\mathbf{B}$ drifts of the ions and electrons caused by $\tilde{\mathbf{E}}$, and will be neglected in pursuit of the Alfvén speed. For the relatively low-frequency Alfvén wave, $\omega \ll \omega_{ci}$. Taking this into account and substituting into the linearized wave equation,

$$\omega^2 - c^2k^2 = -\frac{n_0e^2}{m_i}\frac{\omega^2}{\omega_{ci}^2} = -\omega^2\frac{m_in_0}{\epsilon_0B_0^2} = -\omega^2c^2\frac{\mu_0m_in_0}{B_0^2}. \tag{1.13}$$

Preemptively, we will designate the Alfvén speed $v_A = B_0^2/\mu_0\rho_m$, where $\rho_m = m_in_0$. We solve for $\omega/k_\parallel$, where the $k_\parallel$ denotes that $k \parallel \mathbf{B}_0$, and we assume $c^2/v_A^2 \gg 1$.

$$\frac{\omega^2}{k_\parallel^2} = \frac{c^2}{1 + c^2/v_A^2} \tag{1.14}$$

$$\frac{\omega}{k_\parallel} = v_\phi = v_A \tag{1.15}$$

The Alfvén speed is then the phase velocity of a wave with $\tilde{\mathbf{E}} \perp \mathbf{B}_0$, $\tilde{\mathbf{B}} \perp \mathbf{B}_0$, $\mathbf{k} \parallel \mathbf{B}$. A shear Alfvén wave propagates along the magnetic field with a restoring force provided by $\mathbf{v} \times \mathbf{B}$. This type of wave is analogous to a magnetic field line being plucked like a string.

The remaining discussion of Alfvén waves in toroidal systems is informed primarily by the Heidbrink 2008 review [6] and the Wong 1999 review [5]. In a cylinder with axial symmetry, the magnetic field lines can have an axial component B_ϕ and an azimuthal component B_θ. Assuming a characteristic length $2\pi L$ and designating the distance from the axis as r, the waves will be periodic along field lines. The parallel wave vector is resolved in azimuthal mode number m and axial mode number n,

$$k_\parallel = \frac{mB_\theta}{r|B|} - \frac{nB_\phi}{L|B|}. \tag{1.16}$$

Introducing the safety factor describing the pitch of the field lines, $q = rB_\phi/LB_\theta$, the above equation can be condensed to

$$k_\parallel = \frac{m - nq}{r}\frac{B_\theta}{|B|}. \tag{1.17}$$

When the cylinder is bent into a torus, L is replaced with the distance from the torus center, R, but the above $k_\parallel$ equation is unaffected to first order. m becomes the poloidal mode number that designates the periodicity around a circular cross section of the torus. n becomes the toroidal mode number, designating the periodicity along the torus ring. As $q = q(r)$ and $\mathbf{B} = \mathbf{B}(r)$, the value of $k_\parallel$ changes across the minor radius of the plasma. This implies that under most conditions, $\omega = k_\parallel v_A$ is also a function of the minor radius. The continuous solution $\omega_{mn}(r)$ is referred to as the Alfvén continuum for a given couple of poloidal and toroidal mode numbers.

For a given flux surface, a single frequency corresponds to to the Alfvén resonance. As $k_\parallel$ changes across the minor radius, so does this frequency, Fig. 1.3. If a packet of energy is deposited in a region of finite width with central resonant frequency ω,

Figure 1.3: The Alfvén continuum in a cylinder. The crossing of m and $m-1$ for a given n is plotted in frequency vs. radius.

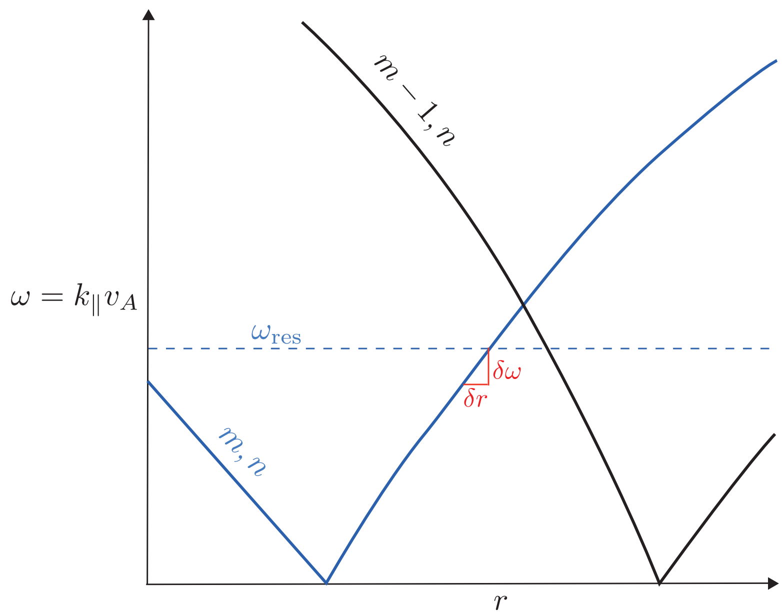

the nearby surfaces resonant at $\omega = \omega_{\mathrm{res}} \pm \delta\omega$ will shear apart the wave. The phase mixing must necessarily happen because shear waves must have finite radial extent in order to propagate. The wave is dispersed with a magnitude $\gamma_{\downarrow} \propto d\omega/dr$. The Alfvén continuum forms a continuous set of resonances which lose wave energy rapidly in practice.

The $\gamma_{\downarrow}$ term is zero at any point where the continuum contains an extremum. The relatively coherent clustered frequencies form a potential well within which an eigenmode solution exists. One extremum is in the core of the plasma, where the magnetic axis creates an extremum in the safety factor. The waves that arise from this condition are Global Aflvén Eigenmodes (GAEs). Another extremum can occur if the dq/dr reverses direction, creating a $k_{\|}$ extremum that generates Reversed-Shear Alfvén Eigenmodes (RSAEs). A phenomenon that is general to toroidal confinement devices is the set of extrema created by toroidicity, which lead to the Toroidicity-induced Alfvén Eigenmodes (TAEs). All of these Alfvén Eigenmodes (AEs) have been observed on tokamak and stellarator devices [12, 13, 14, 15].

A field line traveling in a torus encounters a periodic variation of the magnetic field B_0 as its helical path takes it inboard and outboard of the magnetic axis. The background field periodicity is in the poloidal direction, $B_0 \propto \cos\theta$. The wave speed is $v_A \propto B_0$ and the periodic amplitude of the perturbation is $\tilde{B} \propto \cos(m\theta - n\phi)$. The factor of $(1/R)$ in the toroidal portion of the gradient, $(1/R)d/d\phi$, along with the variation in wave velocity $v_A \propto \cos(\theta)$, couple $m \pm 1$ waves with the same n. At the point where the frequencies of $m \pm 1$ surfaces cross, a gap in the continuum is formed. This crossing occurs at $k_{\parallel,m,n} = -k_{\parallel,m\pm1,n}$, where the negative sign refers to a wave propagating in the opposite direction. Because $k_\parallel$ is a function of q, this sets a condition on q for a crossing to occur,

$$q = \frac{2m \pm 1}{2n}. \tag{1.18}$$

The lowest q value for crossing is therefore $q = 1/2n$. The solutions bifurcate into a low frequency maximum with a phase difference between the background and perturbed field $\delta(\tilde{B}_0, \tilde{B}_\omega) = \pi$, and a high frequency minimum with $\delta(\tilde{B}_0, \tilde{B}_\omega) = 0$, both of which have $d\omega/dr = 0$, Fig. 1.4. It should be noted that for this thesis, $k_\parallel = |k_\parallel|$ is used in order to display the coupling of the Alfvén continuum in an intuitive manner. In reality, $\partial\omega/\partial r < 0$ corresponds to $k_\parallel < 0$ or $n < 0$ solutions, depending on preference. The $\pm n$ terminology will be recovered when it is necessary to distinguish between directions of propagation. The potential well created in the gap between these two extrema is the locus of the TAE, and its frequency is bounded by the gap.

One of the most widely observed sources of energy transfer to the waves is a population of energetic particles. Three conditions must be met in order for energy transfer from particles to the Alfvén waves to occur[6]. First, some component of the fast ion motion point transverse to field lines, such that $\mathbf{v}_i \cdot \tilde{\mathbf{E}} \neq 0$, where $\tilde{\mathbf{E}}$

Figure 1.4: A TAE gap opening in the Alfvén continuum from the coupling of m and $m-1$ at a given n. The TAE frequency lies within the gap, above and below which $\partial\omega/\partial r = 0$.

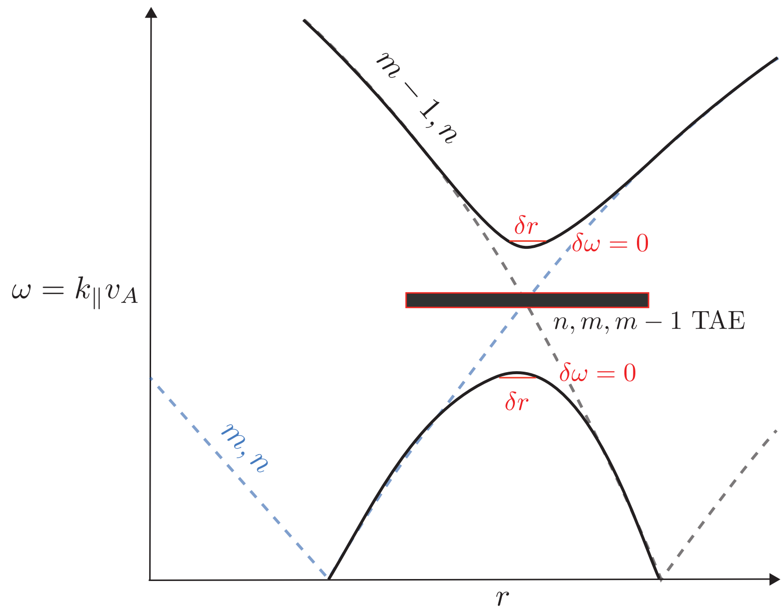

is the expected oscillating transverse field of an Alfvén wave and v_i any component of the fast ion motion. In many devices, this component is the radial drift velocity $\mathbf{v}_D$ of a population of circulating ions, and in others it is the radial component of trapped ion orbits. Second, the fast ion energy transfer must not phase-average to zero, $\oint \tilde{\mathbf{E}} \cdot \mathbf{v}_i \neq 0$. This is equivalent to the average alignment of $k_{\|}$ vectors, or

$$\frac{m+l-nq}{r}\frac{B_\theta}{|B|}v_{\|} = \frac{m-nq}{r}\frac{B_\theta}{|B|}v_A \tag{1.19}$$

where l is any integer and $v_{\|}$ is the component of the beam velocities parallel to the magnetic field line.

Third, there must exist some gradient in energy space for the beam ions such that the total energy of the ion population decreases by its flattening Fig. 1.5. The ion population is characterized by a distribution function f, and the condition for energy transfer to the wave is $\gamma_{\uparrow} > 0$, where $\gamma_{\uparrow} \propto \omega\, \partial f/\partial W$. A "bump-on-tail" distribution is generated from neutral beam injection, where a small group of particles are injected

Figure 1.5: The flattening of the distribution function f at a resonance. The total energy is decreased by particles moving from right to left.

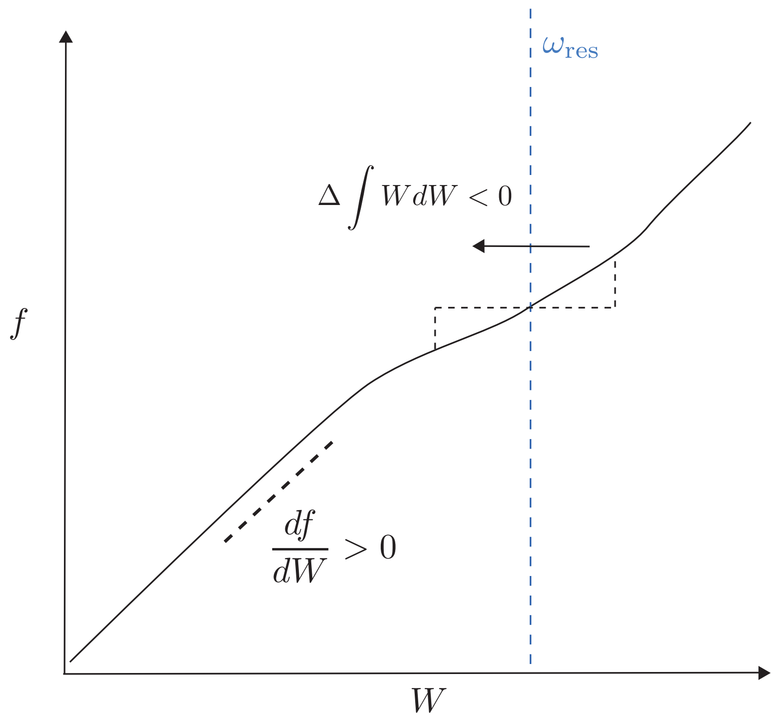

at high velocity, appears as a bump in velocity space so that its low-velocity side has $\partial f/\partial W > 0$, Fig. 1.6. This situation is known as Inverse Landau damping. After a short period of time, the bump-on-tail tends to evolve into a slowing-down distribution with $\partial f/\partial W < 0$, causing wave damping instead of drive.

Another energy gradient, however, exists in real space. A population of beam ions injected on-axis has a radially-peaked distribution. The toroidal angular momentum is

$$P_\zeta = m_i R V_\zeta - q_i \psi, \tag{1.20}$$

where ψ is the flux given by Eq. 1.6. As discussed before, ψ increases with minor radius, so P_ζ decreases in the same direction. Because $W_{i,\zeta}$ increases with the kinetic energy P_ζ^2/m_i, a distribution of ions that is peaked on-axis will have $\gamma_\uparrow \propto \partial f/\partial P_\zeta^2 \propto \partial f/\partial W > 0$, Fig. 1.7. Fast ions with peaked density gradients at the magnetic axis

Figure 1.6: Inverse Landau damping from a bump-on-tail distribution in velocity space. The low-velocity side of the bump flattens analogously to Fig. 1.5.

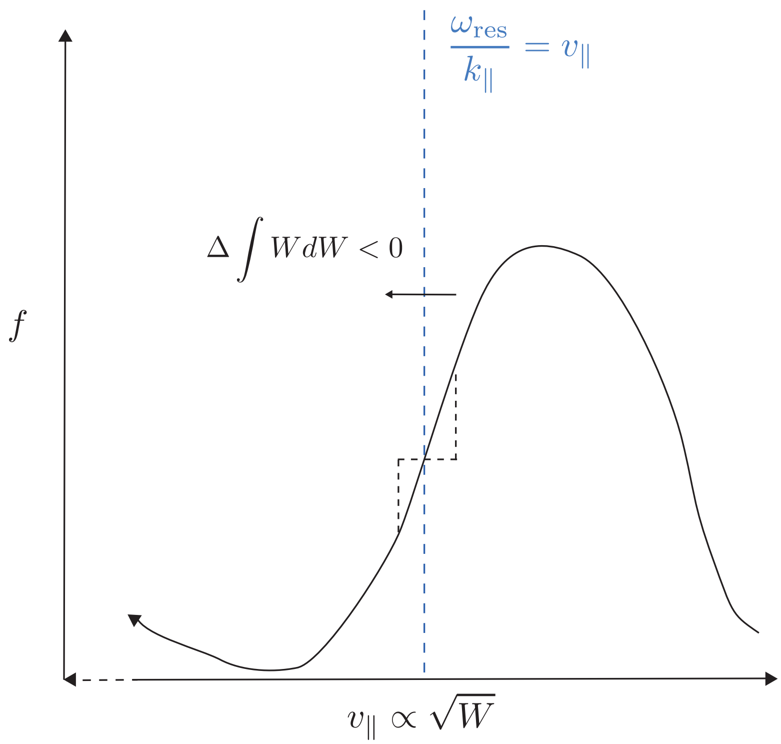

are an energy source to drive instability. For the Alfvén eigenmodes (AEs), the radial density gradient of fast particles is a ready source of drive.

Energetic particle modes (EPMs) arise when the drive from the fast ion population is sufficient to overcome continuum damping. If $\gamma_\uparrow > \gamma_\downarrow$ and the conditions for particle resonance are satisfied, resonant frequencies in the Alfvén continuum will be driven unstable. Coherent waves with ω, n and m specified by a compromise between the continuum and the beam ions will grow.

1.4 Madison Symmetric Torus

Madison Symmetric Torus is an RFP with plasma parameters as specified in Table 1.1 [16]. The machine has a major radius of 1.5 m and a minor radius of 0.52 m,

Figure 1.7: Resonant drive by a fast ion spatial gradient. As the flux ψ and radial coordinate r increase away from the axis, the toroidal angular momentum P_ζ decreases. Particles moving outward decrease the total energy.

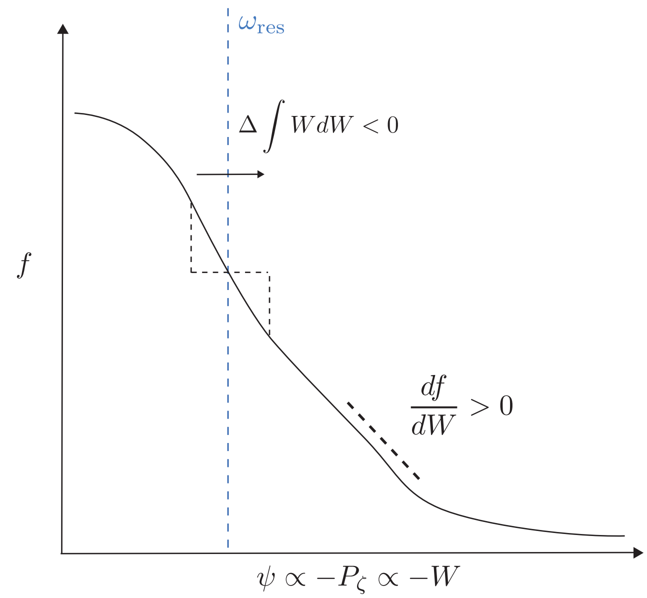

giving an aspect ratio $R_0/a \approx 3$, Fig. 1.8. The conducting shell is 5 cm thick, and its inner wall has graphite tiles that cover the toroidal extent at $\theta = 0°, 180°$.

Table 1.1: MST Parameters

Parameter	Abbreviation	Minimum	Maximum
Plasma Current (MA)	I_p	0.2	0.6
Toroidal Field On-Axis (T)	$B_\phi(0)$	0.2	0.55
Axis Safety Factor	q_0	0.167	0.23
Edge Safety Factor	q_a	-0.15	+0.01
Electron Density (m^{-3})	$\bar{n}_e$	0.3×10^{19}	1.6×10^{19}
Electron Temperature (keV)	T_e	0.1	2
Discharge Duration (ms)		30	75

The RFP configuration can be approximated by a Taylor State [2], a minimum

Figure 1.8: Madison Symmetric Torus

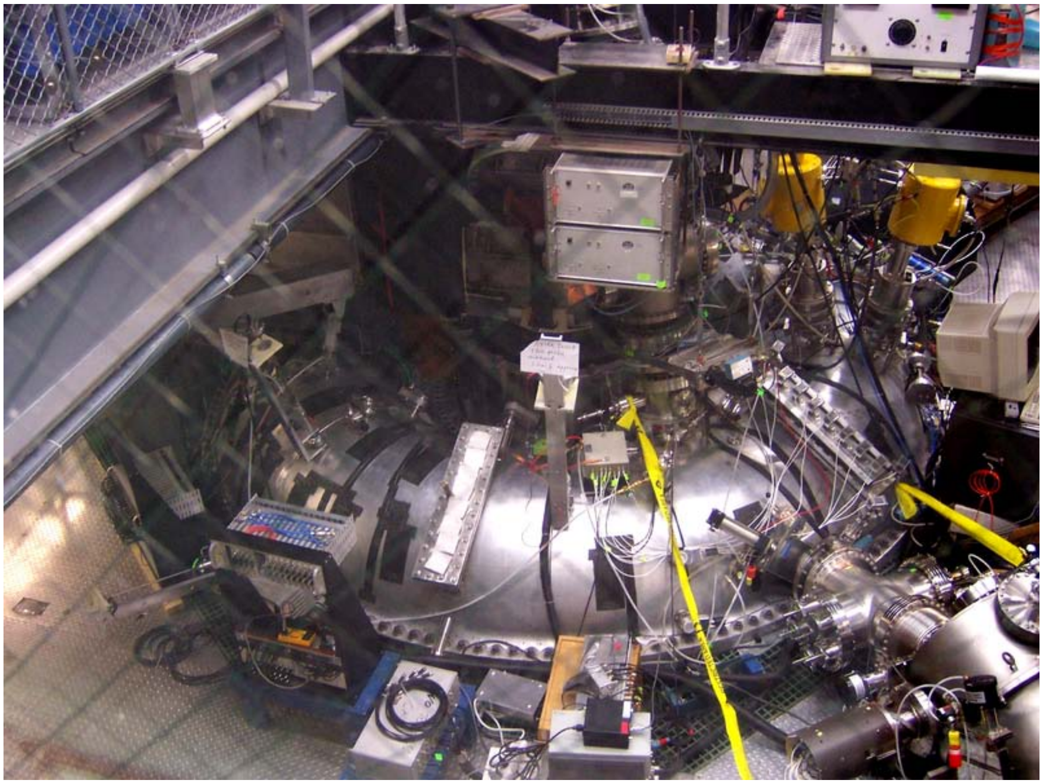

energy state of the current and magnetic fields, which are prescribed by

$$\nabla \times \mathbf{B} - \lambda \mathbf{B} = 0, \tag{1.21}$$

where λ is the magnitude of the parallel current $j_{\|}$. The solution to this equation is a Bessel function model (BFM) whose notable features are that λ is constant and $\langle B_\phi \rangle \sim \langle B_\theta \rangle$. In practice, $\lambda = 0$ at the boundary, so near the boundary it sharply decreases, a feature that is not captured by the BFM. The q profile is small and monotonically decreasing, passing through zero and into negative values at the edge, Fig. 1.9.

The RFP configuration is generated on MST through a few steps. First, a toroidal field B_ϕ is produced by driving poloidal current in the conducting shell. Deuterium gas is puffed into the vessel through holes in the shell. The gas is ionized by a toroidal electric field E_ϕ induced by the iron core transformer, Fig. 1.10. The field

Figure 1.9: Magnetic field and safety factor profiles for an MST discharge. The toroidal field and safety factor go to zero at the edge.

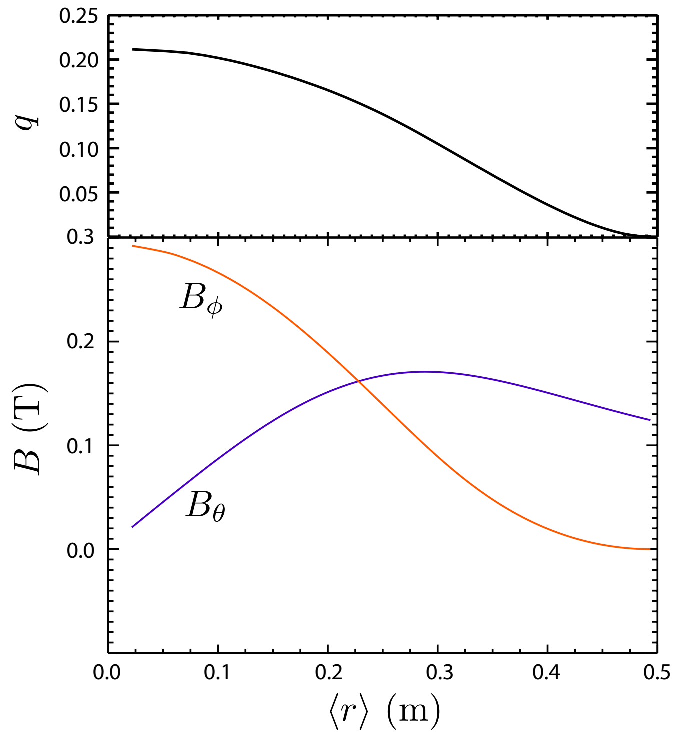

also causes initial current to flow toroidally, which generates the poloidal magnetic field B_θ. The resulting twisted fields act as conduits for the ions and electrons to flow along, generating a progressively more twisted field farther from the magnetic axis. As the configuration relaxes into a minimum energy state, B_ϕ at the edge goes to zero or reverses direction from its core value. This reversal is maintained by the sawtooth cycle, which regenerates toroidal flux. The resultant magnetic fields are shown in Fig. 1.9. The plasma sustains the configuration by acting as the transformer secondary, converting poloidal flux from the transformer to toroidal current in the magnetic shell. The discharge is limited by the number of $V \cdot s$ available to drive E_ϕ.

A typical discharge for MST is shown in Fig. 1.11. The line-averaged electron density $\bar{n}_e$ spikes at the ionization point, then flattens as the discharge stabilizes. The plasma current I_p ramps up continuously and reaches a flat-top at 15 ms before

Figure 1.10: The iron core transformer is used to drive toroidal electric field.

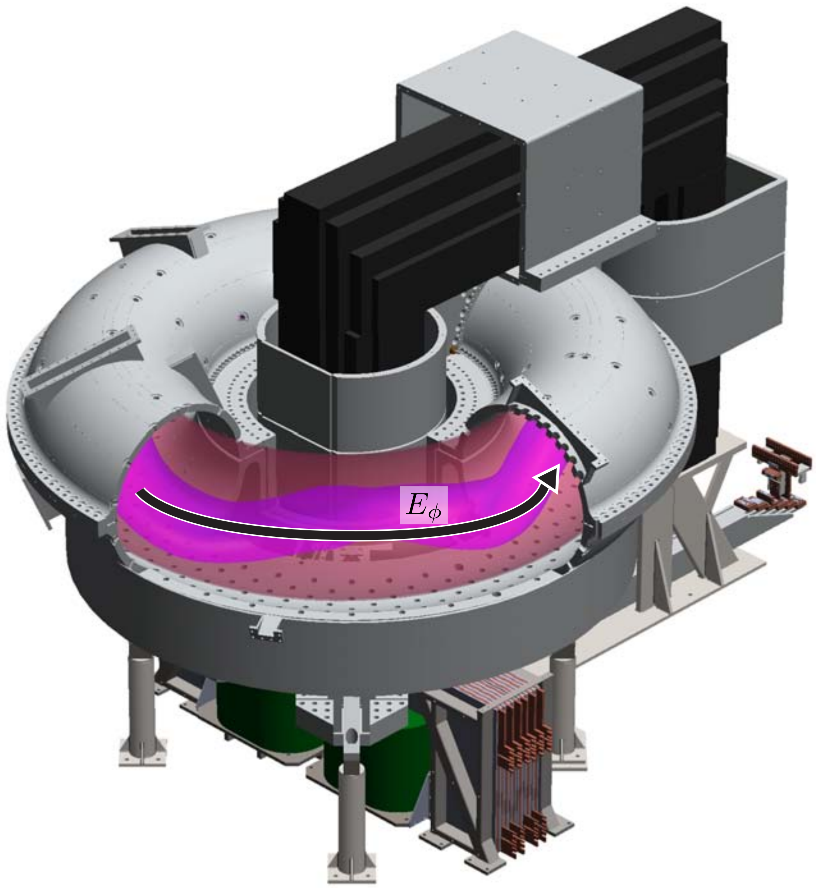

ramping down at 35 ms. The toroidal field at the wall $B_{\phi w}$ starts high and reverses as the RFP configuration develops, while the average toroidal field $\langle B_\phi \rangle$ tracks roughly with I_p. Most of the physics research requiring steady-state operation is performed during the flat-top of I_p, when the field evolution is only governed by the sawtooth cycle.

1.4.1 Tearing Modes and Sawtooth Events

The iron core transformer drives current toroidally by inducing a toroidal electric field E_ϕ. At the edge of the plasma, $B_\theta \gg B_\phi$, restricting the ion and electron motions in

Figure 1.11: Time traces of plasma current, electron density, edge safety factor, toroidal magnetic field at the wall, and average toroidal magnetic field. Experiments are traditionally performed from 20 to 40 ms, in the "flat top" portion of the discharge.

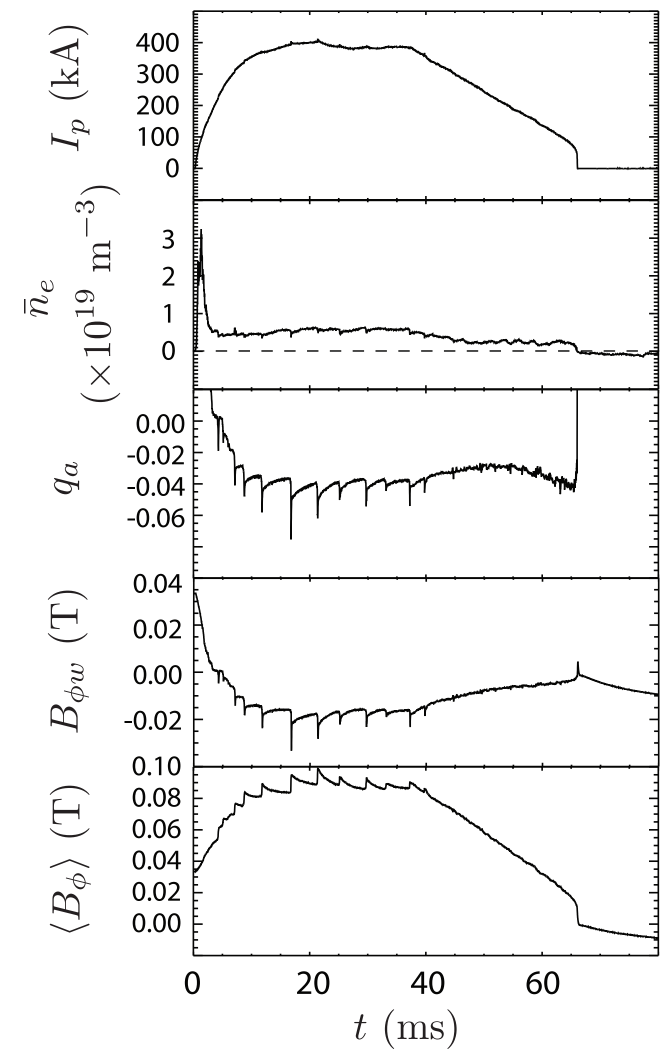

Figure 1.12: Core $n = 6$ islands and stochastic magnetic fields past mid-radius for MST. Multiple overlapping islands outside the core cause the field lines to wander across from mid-radius to the reversal surface. From [17]

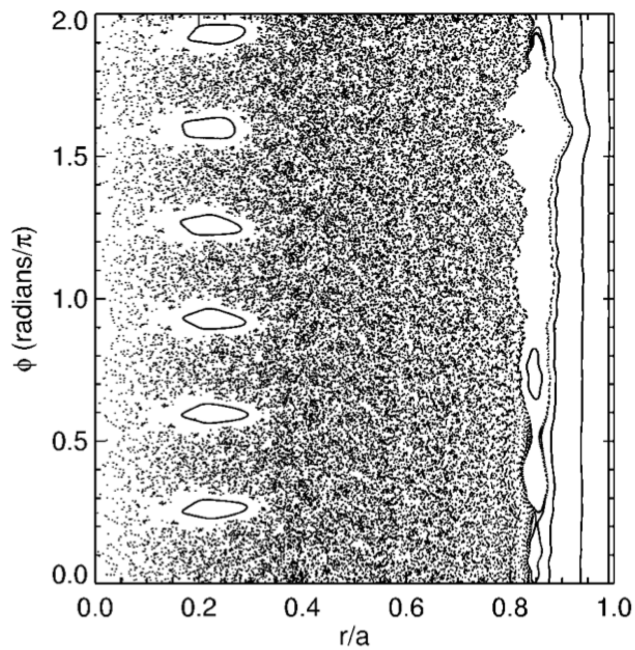

the toroidal direction. Current is driven principally in the core of the plasma, altering the λ profile. Concurrently, finite resistivity permits growth of tearing modes located on rational surfaces, $q(r) = m/n$. The core tearing mode island grows and saturates as q_0 decreases over time. Tearing mode islands outside the core overlap, creating a stochastic field that degrades energy confinement, Fig. 1.12[17].

When the current in the core reaches a critical threshold, the flux surfaces deform globally. Nonlinear coupling of the $m = 1$ tearing modes in the interior of the plasma with $m = 0$ modes at the $q = 0$ reversal surface enables a rapid relaxation of the peaked current profile. The plasma regenerates toroidal flux, resetting to a state closer to the Taylor state. These events are referred to as "sawteeth" for their characteristic form on the $\langle B_\phi \rangle$ signal. They are evident in the B_ϕ traces on Fig. 1.11.

1.4.2 Neutral Beam Injector

In 2010, a 1 MW neutral beam injector NBI was installed on MST, Fig. 1.13. The injector fires 25 keV ($v_{B,H} = 2.2 \times 10^6$ m/s, $v_{B,D} = 1.6 \times 10^6$) atomic hydrogen and deuterium tangentially to the core magnetic field. The beam is typically run with 97% H and 3% D, but can be run with other mixtures of gasses, including 100% deuterium. The neutral beam particles are ionized by collisions along the beam path, predominantly in the core of the plasma. Beam parameters are listed in Table 1.2.

Table 1.2: MST NBI Parameters

Parameter	Abbreviation	Value
Beam Power (MW)	P_{beam}	0.35 - 1
Neutral Energy (keV)	E_{beam}	17 - 25
Beam Current (A)	I_{beam}	20 - 40
Pulse Length (ms)		5-20

Previous calculations using the Transp[18] code for beam deposition were performed to determine the fast ion profile. The fast ion distribution builds up in the core of the plasma with pitch relative to field lines of $v_{\|}/v = 0.9$, Fig. 1.14. Previous work has established that the fast ion confinement time is significantly longer than the energy and particle confinement times of thermal ions, $\tau_{fi} = 5 - 30$ ms [19]. This classical confinement is a product of the pitch of the injected ions, which orbit-average over the tearing mode islands and stochastic fields, Fig. 1.15, resulting in $\oint \tilde{\mathbf{E}} \cdot \mathbf{v} = 0$. The deposited fast ions have an inverse rotational transform q_{fi} which is boosted off of the plasma safety factor by the fast ion pitch, 1.16.

With a steadily-increasing population of fast ions in the core whose density gradient is sharp in radius, there is opportunity for TAE and EPM excitation by $\partial f/\partial P_\zeta^2 > 0$. MST plasmas with beam injection are excellent test beds for investigations into beam-driven instabilities. This work describes the results of those investigations.

Figure 1.13: Neutral Beam Injector installed on MST. The beam passes through the core of the plasma tangentially. The diagnostic neutral beam is also depicted passing through the plasma radially.

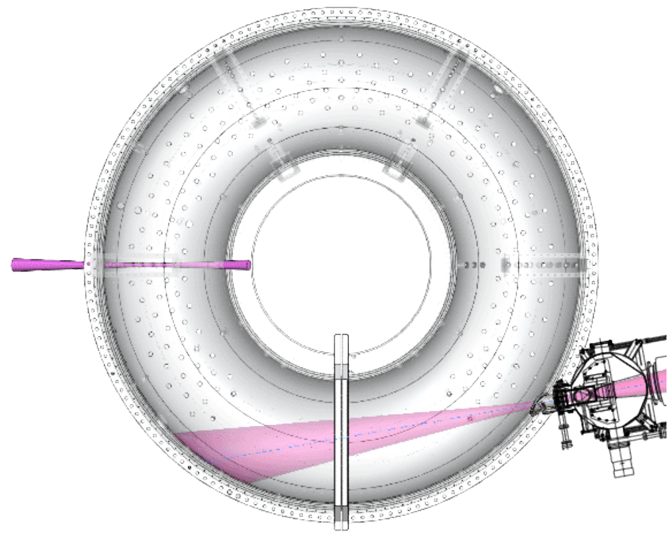

Figure 1.14: Fast ion density n_{fi} after 2 ms of beam injection. The fast ions are highly core-localized, with high $v_{\|}$.

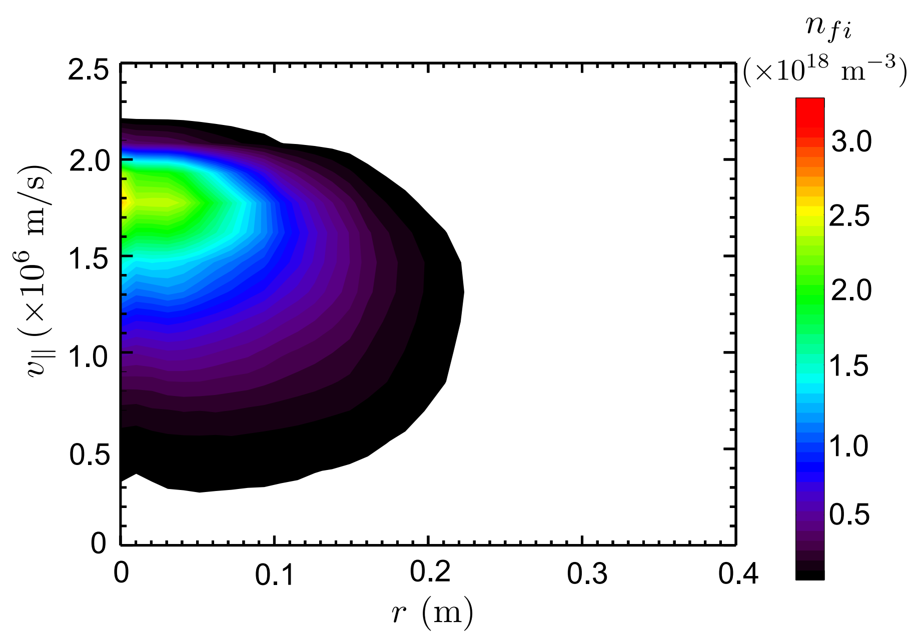

Figure 1.15: Fast ion guiding center puncture plot overlaying field line puncture plot for MST. The fast ions are insensitive to islands and stochastic fields, localizing them to the core of the plasma.

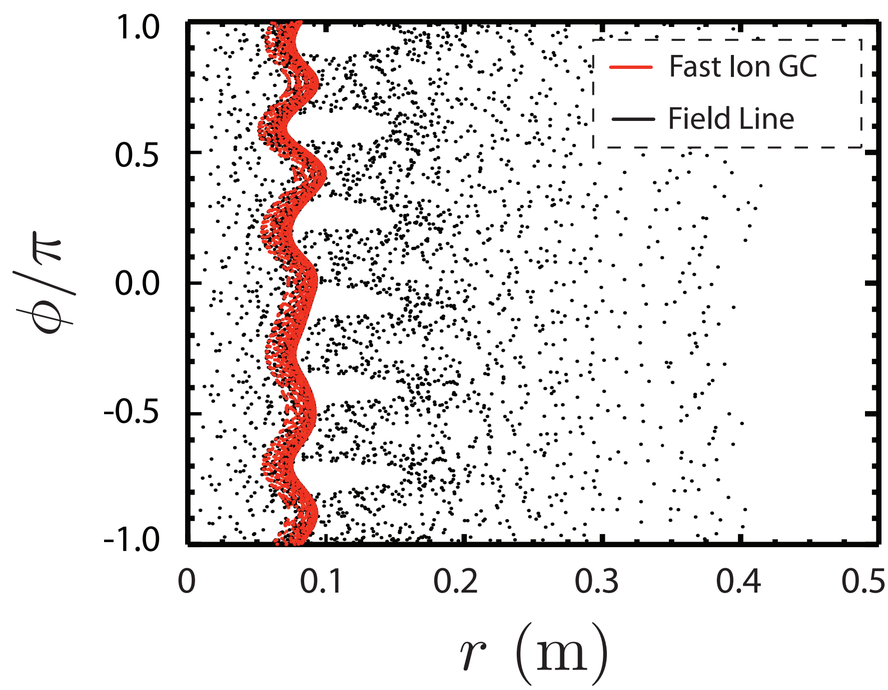

Figure 1.16: Fast ion and plasma safety factor. The fast ion safety factor is boosted off of the plasma safety factor due to the high pitch of injected ions.

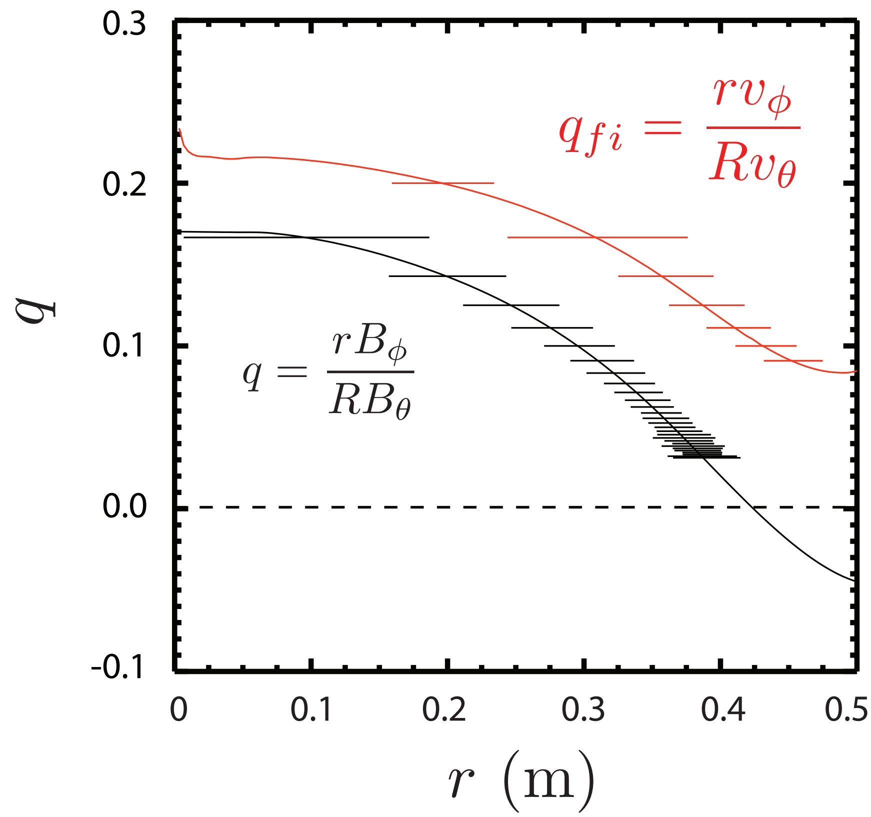

Chapter 2

Relevant Diagnostics for Mode Analysis and Equilibrium Reconstruction

In order to examine physical characteristics of plasma equilibria inside MST and to diagnose MHD activity at Alfvénic frequencies, a host of diagnostics are employed. This chapter inventories the diagnostic suite on MST at the time of writing, briefly outlines the physics associated with each tool, and assesses its viability for 3D equilibrium reconstruction and mode characterization from the standpoint of information content, temporal and spatial resolution, and position. Particular attention is paid to the magnetic diagnostics. The focus is on the necessary information to work with the diagnostic outputs. Discussion of the diagnostics methods upstream and downstream of MST is left to the cited publications.

2.1 Magnetics

By Faraday's Law, a changing magnetic flux through an area induces an EMF along the edge of the loop. The magnitude of this EMF is $\epsilon = -d\Phi/dt$, where the magnetic flux $\Phi = BA\cos(\phi)$, B is the magnetic field strength, A is the area of the loop, and ϕ is the angle between the loop and the average field line direction. With a conducting loop of known area A and resistance R, N turns can be included to multiply the total induced EMF. If the loop is at a fixed orientation, $\hat{\mathbf{e}}$, and one includes Ohm's law, $I = \epsilon/R$, one can calculate the magnitude of change in magnetic field normal to the coil area as:

$$\frac{dB_e}{dt} = \hat{\mathbf{e}} \cdot \hat{\mathbf{b}} \left(\frac{I}{ANR} \right) \tag{2.1}$$

where $\hat{\mathbf{b}}$ is the normalized vector corresponding to the orientation of the magnetic field. Integration of this quantity over time with the correct constant of integration ($t = 0$, $B = 0$) will provide the total magnetic field at the coil at a point in time.

2.1.1 Magnetic Arrays

On MST, most of the magnetic diagnostics are affixed to the inside of the conducting shell, between the shell and the plasma boundary set by the 1.3 cm limiter. Eddy currents in the shell cancel out the magnetic fields inside at a skin depth of $\delta \approx 2$ cm on the timescale of a 60 ms pulse, making measurement of internal fields implausible outside of the vessel.

In order to resolve all 3 components of the perturbed magnetic field vector $\tilde{\mathbf{B}}$ at a point in space, 3 loops with orthogonal facings, $\hat{\mathbf{e}}_\mathbf{i} \cdot \hat{\mathbf{e}}_\mathbf{j} = \mathbf{0}$, are used. This configuration is known as a Mirnov triplet. Ceramic coil forms for the Mirnov triplets were fabricated such that they could be attached to the vessel wall while protecting the coils from plasma interactions, Fig. 2.1 [20]. The forms are 3.8×2.5 cm,

Figure 2.1: Array coil forms and graphite covers. B_r, B_θ and B_ϕ coils are located at different places in the coil form. The wires exit through a port on one side of the coil form.

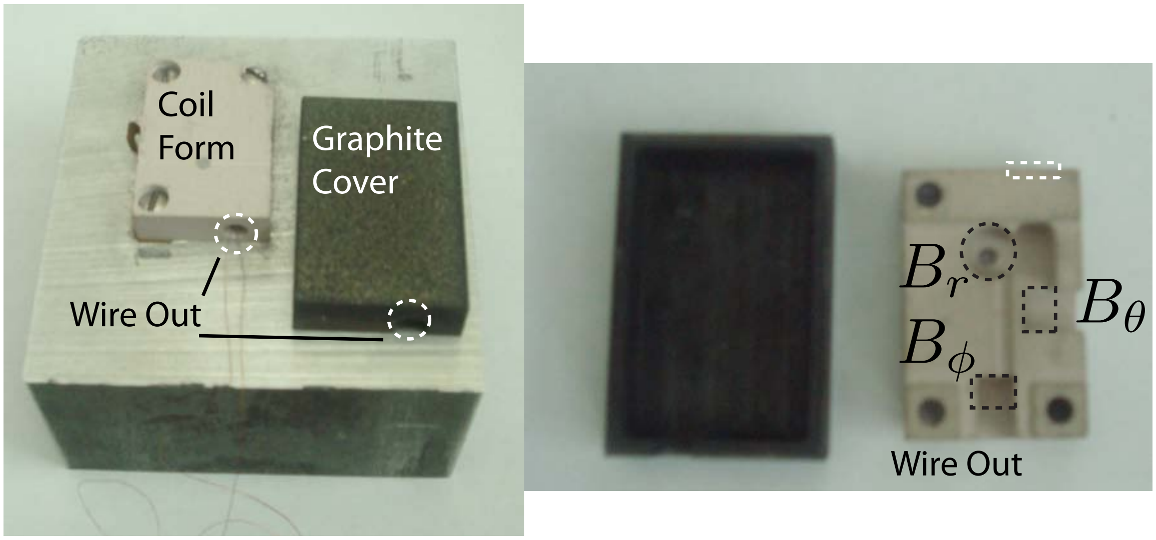

with 5-turn coils of 32-gauge HML-coated wire and effective areas of $1.5 \pm .1$ cm^2. Because of the need for compactness in the radial direction, the coil forms could not accommodate all coils in a 3D geometry. They are designed with the radial-facing coil serving as the basis for positioning, with the poloidal-facing coil offset by 8 mm and the toroidal-facing coil offset by 22 mm, both in the same direction. The plasma-facing side of the coil form is fitted with a 3/32" graphite cover to protect the coils while minimally impacting any detectable magnetic fields.

In order to resolve perturbations that are periodic in the toroidal direction, a set of evenly-spaced Mirnov triplets with resolution on relevant scales for the system in question is desired. Dominant tearing modes on MST are $n = 5$ or $n = 6$ perturbations, requiring at least 10 triplets to resolve by the Nyquist-Shannon sampling theorem[21]. However, secondary modes exist up to arbitrarily high mode numbers due to a safety factor q profile that passes through 0. Experimentally, $< 1\%$ of the total tearing mode energy is contained in the $n > 10$ modes. 64 locations were chosen for three reasons. First, many digitizer boxes have 4, 8 or 16 inputs. Factors of 2 are preferable for Fast Fourier Transforms[22]. Finally, 64 locations leads to a Nyquist resolution of $n = 32$, providing the capability to analyze ≈ 27 higher-n secondary modes in addition to the dominant tearing mode. $n = 32$ corresponds to a resonant location at $q = 0.03125$ for $m = 1$ modes, close to the reversal surface.

The formula for toroidal location (in degrees) of the triplets is:

$$\phi_i = 5.625 \cdot i + 2.813, i = 0 - 63$$

All coil forms in the toroidal array are located at $\theta = 241°$ and $r = 0.5165 \approx 0.993 \cdot a$. They are attached to the vessel inner wall on the inboard side, 61° below the midplane, Fig. 2.2.

A small offset in coil locations must be accounted for in mode analysis codes. The centerline of each coil form, aligned with the radial-facing coil, sits at ϕ_i as calculated by the formula. However, due to the necessary flatness of the coil forms, the B_θ and B_ϕ coils have a toroidal offset. For the B_θ coil, the offset is 8 mm, or $\phi_{\text{off}} = 0.393°$. For the B_ϕ coil, the offset is 22 mm, or $\phi_{\text{off}} = 1.0°$. Although the offset is a small distance compared to the transit length of the torus at $\phi = 241°$ (7.85 m), for high-n modes this leads to a phase offset of up to 32°. Wire leads enter each coil form from the opposite side as the offset, and exit the torus near $\phi = 180°$. In order to avoid bending the wires unnecessarily, the wires exit facing this location, causing opposed offsets on either half of the torus, Fig. 2.3. This leads to a new equation for the coil locations:

$$\phi_i = \begin{cases} 0 \leq i \leq 31 & : 5.625 \cdot i + 2.813 - \phi_{\text{off}} \\ i > 32 & : 5.625 \cdot i + 2.813 + \phi_{\text{off}} \end{cases} \tag{2.2}$$

where ϕ_{off} is the number quoted in the above paragraph.

Three poloidally symmetric arrays of coils were installed to resolve poloidal mode numbers (m) in addition to toroidal mode numbers (n). Dominant tearing modes

Figure 2.2: MST magnetic array locations. Three poloidal arrays, one toroidal array, a flux loop and a Rogowski coil comprise most of the internal magnetic diagnostics on MST.

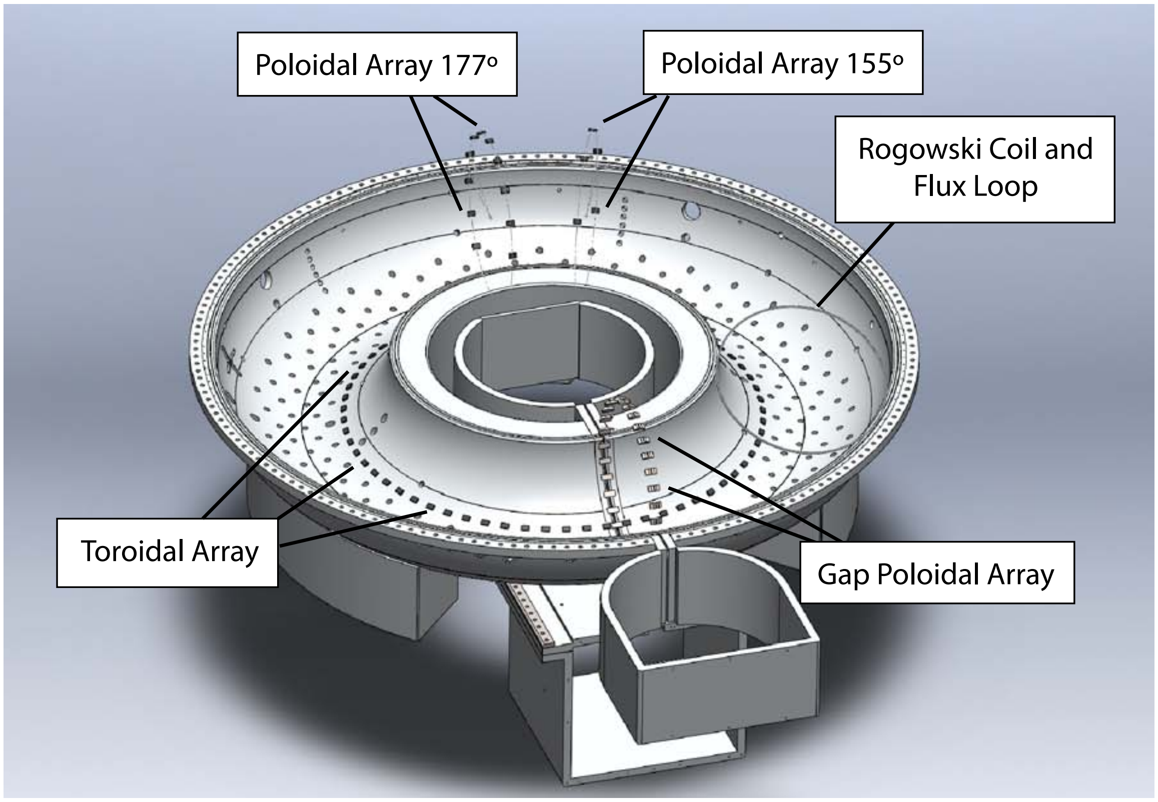

have $m = 0$ or $m = 1$, so a small number of coils were required to resolve even-odd asymmetry. Like the toroidal array, the number of coils in each array is factorable by 2, and the coils are evenly spaced. For the arrays of 8 coils at $\phi = 155°$ and 16 coils at $\phi = 177°$, the coil configurations are the same as those in the toroidal array. Each has a triplet of coils in the same type of coil form, Fig. 2.3. However, because the coil forms are aligned in the same direction, long side toroidally parallel with all offsets in the same direction, there is no relative offset to correct.

The formulas for the poloidal locations (in degrees) of each set of triplets are:

$$\theta_{155,i} = 45.0 \cdot i + 16.0, i = 0 - 7 \tag{2.3}$$

$$\theta_{177,i} = 22.5 \cdot i + 16.0, i = 0 - 15 \tag{2.4}$$

Figure 2.3: Illustration of the coil form offsets on MST. The offsets arise because the B_r coil is below the centering line, and the wire exits opposite the B_ϕ and B_θ coils displacements.

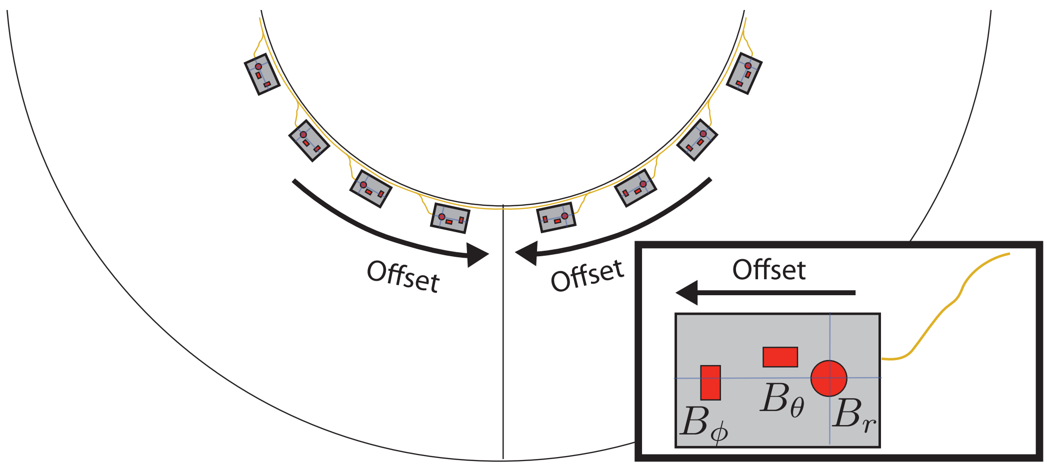

The poloidal magnetic array at $\phi = 0°$ is different than the other two due to its special function. It is located at the poloidal gap, where radial magnetic field can penetrate. At 32 locations, radially-facing coils monitor this radial field to inform the active feedback system, enforcing $\mathbf{B} \cdot \hat{\mathbf{n}} \approx 0$. These coils have many more turns than the other arrays, giving them an effective area of 25 cm^2.The field correction improves confinement and reduces rotational locking, an undesirable effect [23]. These measurement locations are:

$$\theta_{B_r,i} = 11.25 \cdot i + 5.625, i = 0 - 31$$

No toroidally-facing coils are placed in the gap array, but poloidal field coils are located at every other coil form. These 16 coils are used primarily to determine the Shafranov shift in axisymmetric plasmas [24]. They have 10 turns, giving them an effective area of 3 cm^2 Their locations are:

$$\theta_{B_p,i} = 22.5 \cdot i + 5.625, i = 0 - 15$$

Table 2.1: Toroidal and Poloidal Array locations

Measurement	ϕ	θ	offset	$\mathrm{A_{coil}}$ (cm^2)
Toroidal $\mathbf{B}_\phi$	$64 \times 5.625°$	241°	1°	1.5
Toroidal $\mathbf{B}_\theta$	$64 \times 5.625°$	241°	0.39°	1.5
Toroidal $\mathbf{B}_r$	$64 \times 5.625°$	241°	0°	1.5
Gap $\mathbf{B}_\theta$	0°	$16 \times 22.5°$		3
Gap $\mathbf{B}_r$	0°	$32 \times 11.25°$		25
Poloidal $\mathbf{B}_{r,\theta,\phi}$	155°	$8 \times 45°$		1.5
Poloidal $\mathbf{B}_{r,\theta,\phi}$	177°	$16 \times 22.5°$		1.5

A table is included for ease of reference in the future, Table 2.1.

Array signals are passed through integrator circuits to determine $\tilde{\mathbf{B}}(t)$ or solely through amplifiers to preserve the $d\mathbf{B}/dt$ signal. Absolute calibration of the $\mathbf{B}_\phi$ signals is performed just before $t = 0$ in each shot, when a known vacuum toroidal field is present. Relative calibration of the $\mathbf{B}_\theta$ coils is performed during the shot by comparison of the average signal in each coil over a large averaging window. These signals are assumed to be the same average amplitude, provided that any tearing modes are continuously rotating throughout the averaging window, and no static perturbations are dominant. This assumption can be easily checked on either the $\mathbf{B}_\phi$ or $\mathbf{B}_\theta$ signals for any shot.

The fixed toroidal and poloidal magnetic coil arrays provide the backbone of periodic perturbation analyses, whether at high frequency or for static perturbations. The arrays have seen extensive use in tearing mode analysis [25, 26, 27].

For Alfvénic frequency activity (100's of kHz), 32 $\mathbf{B}_\theta$ signals from the toroidal array and 8 of both $\mathbf{B}_\phi$ and $\mathbf{B}_\theta$ signals from the poloidal array at $\phi = 155°$ were digitized at f =2 MHz, corresponding to a Nyquist frequency of $f = 1$ MHz. In order to do this, 250 kHz low-pass filters were jumpered out in the amplifier-only portion of the integrator-amplifier boxes. These filters screen high-frequency noise

Figure 2.4: Toroidal array coil gains and time offsets on $\dot{B}$ signals at three different gain settings.

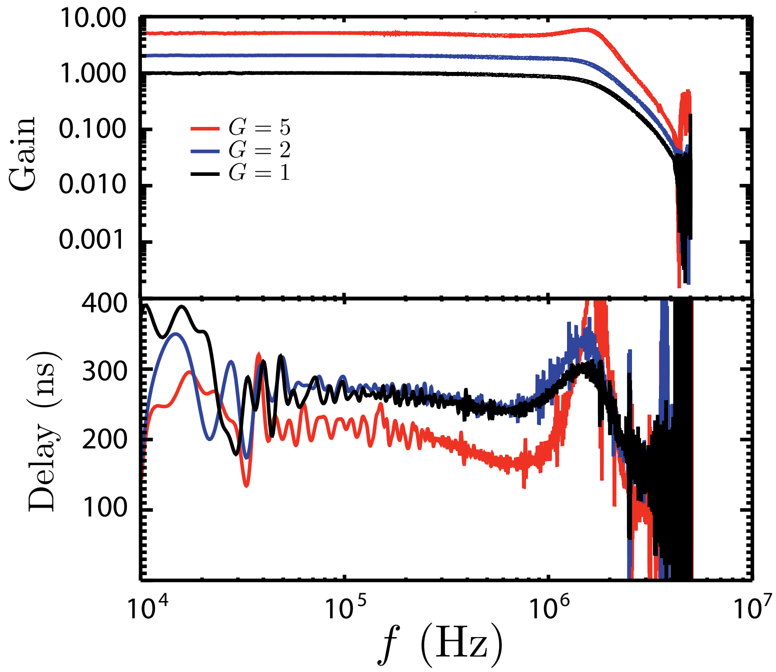

from the magnetics signals, providing a cleaner signal for tearing mode studies. As tearing mode frequencies are generally below 50 kHz, filters are practical for that application. Unfortunately, they preclude easy access to toroidally-resolved high frequency signals. Additional signals or higher-frequency digitization could provide yet more information, but 32 $\mathbf{B}_\theta$ signals was considered adequate for mode analysis, and both hardware and digital storage constraints limited further modification. Toroidal array frequency response was measured up to 5 MHz and shown to be relatively flat up to 1 MHz, Fig. 2.4.

A number of features allow the toroidal and poloidal arrays to be easily used for high frequency mode analysis. Coil spacing is nearly ideal for analysis in Fourier space, and spatial decomposition is a well-documented and computationally robust process on MST. At higher digitization frequencies, this process is identical because it is done at each time point individually. Because of the wide coverage of the arrays, they are ideal for determining phase for use in pseudospectral analysis [26], allowing correlation with chord or point measurements.

For three-dimensional equilibrium reconstruction, the toroidal and poloidal arrays are essential. The integrated signals provide a strong constraint on the phase of a helical equilibrium, as well as its perturbation amplitude at the wall. While toroidally-localized chord measurements provide strong constraints on internal mode structure, poloidal phase is often weakly constrained due to uncertainties and symmetry along chords. This strong constraint from the magnetics arrays forces reconstructions to fit internal measurements via adjustment of internal values for magnetic field and pressure.

2.1.2 Dense Array and Probes

In addition to coil arrays that span a full toroidal or poloidal transit, there are a number of other possible coil sets for detecting magnetic perturbations. There is an additional "dense array" of 32 $\vec{\mathbf{B}}_\phi$ and 16 $\vec{\mathbf{B}}_\theta$ coils, designed to measure high-frequency, short wavelength fluctuations and turbulent spectra [20]. There are also many portholes through which probes with magnetic or electrostatic sensors may be inserted.

The dense array is a structure centered at $\phi = 246°, \theta = -32°$. It is shaped like a "plus" sign, with four extended arms. The ϕ-direction arms have 8 $\mathbf{B}_\phi$ coils separated by 1 cm, and the θ-direction arms are similar, albeit with $\mathbf{B}_\theta$ coils. The coils are constructed from 25 turns of 38 gauge HML coated copper wire, with an effective area of 1.4 cm^2 each. The center of the structure is a graphite block similar in appearance to those on the magnetic arrays, and it acts as both a limiter and a router of wires coming from the coils. The signal from these coils is amplified but not integrated.

Using bi-spectral analysis, the dense array can resolve the wavenumber spectrum of high frequency fluctuations on time scales up to 3 MHz and spatial scales down to ≈ 100 m^{-1}. Although it must be correlated with the toroidal array in order to determine whether oscillations are periodic throughout the torus, the dense array is nonetheless a useful tool for detecting transient and high frequency waves. Its resolution is adequate well above Alfvénic frequencies. Dense array signals could be digitally-integrated to provide an outboard magnetic constraint on three dimensional equilibria, but this is not done at present.

Probes are constructed regularly for insertion into MST through its many port-holes. Probes containing magnetic loops can be used to detect $\dot{B}$ at many locations. They can be inserted ~ 5 cm to obtain magnetic field measurements inside the plasma. For both mode analysis and equilibrium reconstruction, they could provide additional spatial resolution. At present, neither insertable probes nor the dense array are used in MSTFIT or V3FIT.

2.1.3 Single Loops

By applying Faraday's Law to a loop surrounding the plasma poloidally, Eq. 2.1 and integrating, one measures the total toroidal magnetic flux Φ. If this number is divided by the area enclosed, the result is the average toroidal field in the plasma, $\langle \mathbf{B}_\phi \rangle = \Phi/A$. One such flux loop is located at 60° toroidal. The average toroidal field is an important constraint for helical equilibrium reconstruction. It is a highly accurate measurement that prevents solutions from arbitrarily modifying the toroidal magnetic field to scale perturbation amplitudes.

If the loop enclosing an area is a solenoid of constant solenoidal area A_S and n turns per unit area instead of a solid wire, Fig. 2.5, application of the same formula

Figure 2.5: Measuring the flux through the bent coil is equivalent to measuring the current enclosed.

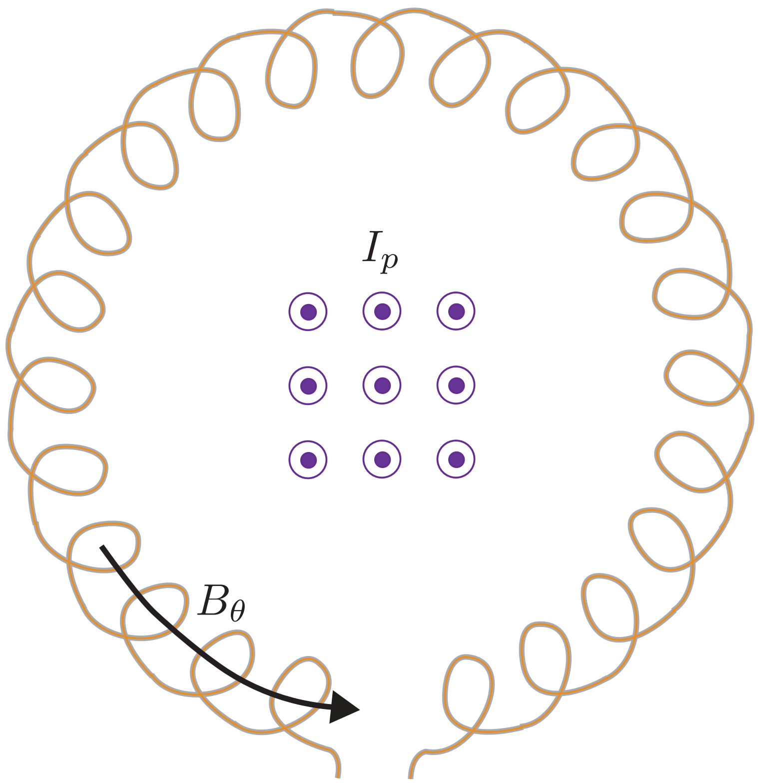

gives:

$$\Phi = nA_S \oint_l \vec{\mathbf{B}} \cdot d\vec{\mathbf{l}}$$

Where $\vec{\mathbf{l}}$ is vector in the $\hat{\theta}$ direction around the circumference of the plasma. By Ampère's Law, $\oint_l \vec{\mathbf{B}} \cdot d\vec{\mathbf{l}} = \mu_0 I_{\text{plasma}}$, where I_{plasma} is the current in the plasma that the solenoid surrounds. Applying Faraday's law again and integrating, the total current in the plasma can be found:

$$\Phi = nA_S \mu_0 I_{\text{plasma}}$$

$$-\frac{d\Phi}{dt} = \epsilon = -\frac{d\left(nA_S \mu_0 I_{\text{plasma}}\right)}{dt}$$

$$I_{\text{plasma}} = -\frac{1}{nA_s\mu_0} \int \epsilon \cdot dt$$

Integration of the voltage generated in the solenoid over time, multiplied by geometric factors and constants, provides the total plasma current enclosed. This measurement apparatus is known as a Rogowski coil. MST has one such internal coil, located next to the flux loop at 60° toroidal. The total plasma current provides a similar constraint to the flux loop, limiting the how much an equilibrium reconstruction code can change global plasma values.

2.2 Passive Diagnostics

Plasmas radiate light and eject particles through a variety of processes, offering ample opportunity to diagnose plasma conditions without perturbative methods. Magnetic loops as discussed previously are one type of passive diagnostic, but others include cameras for light collection or holes in the wall that lead to particle analyzers. Often passive diagnostics will be set up in arrays or coupled to active diagnostics in order to exert more control over the conditions of measurement.

2.2.1 Soft X-Ray (SXR)

Bremsstrahlung radiation, or "braking radiation," occurs when a fast-moving electron accelerates through an electric field. The electron emits radiation via conservation of energy. In plasmas, this happens when electrons come into proximity of the much more massive ions. This type of interaction is ubiquitous in the plasma, so light is produced throughout the plasma volume. For a single electron's deceleration, the power radiated (P) is given by the Larmor equation:

$$P = \frac{e^2 a^2}{6\pi\epsilon_0 c^3}$$

where e is the electron charge, a is the acceleration, and c is the speed of light. If one assumes a Maxwellian distribution of electrons slowing on a similarly-distributed

Figure 2.6: Old thin-filter and new 4-camera SXR systems using for equilibrium reconstruction. From [28].

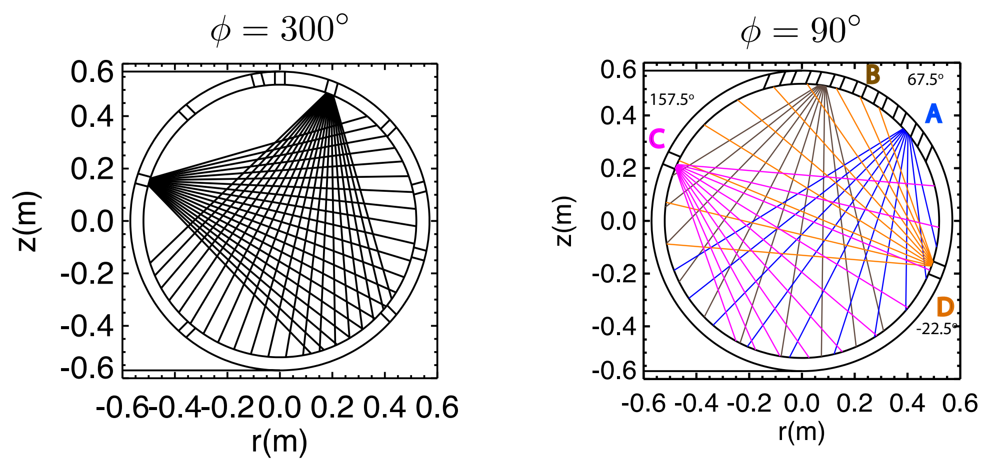

background of ions, it has been shown that power radiated from a unit volume at a given energy E goes as:

$$P\left(E\right) \propto n_e^2 Z_{eff} T_e^{1/2} e^{-E/T_e}$$

where n_e is the electron density, T_e is the electron temperature and Z_{eff} is the effective charge per ion for background ions. Z_{eff} quantifies the effect of impurities on the observed properties of the ion population.

By using a double filter method [28], the energy-independent effects on radiated power from Z_{eff} and n_e can be corrected for simultaneously, allowing for a measurement of T_e alone. Even without this correction, soft x-ray measurements can provide information about the flux surfaces. If Z_{eff} is assumed to either be a flux function or be flat across the plasma volume, $P\left(E\right)$ can be assumed to be a flux function itself. In this case, the measured brightness f along a chord is a suitable reconstruction parameter.

On MST, soft x-ray camera systems have undergone two major iterations relevant to equilibrium reconstructions. Prior to June 2011, a system with 408 μm thin filters on two cameras and 821 μm thick filters on two cameras was in place at 300° toroidal.

The cameras with thick filters were located at $-45°$ and $+45°$ poloidal, and the cameras with thin filters were at $+75°$ and $+165°$ poloidal, Fig. 2.6. Each camera housed an array of 20 diodes, corresponding to 20 viewing chords per camera, or 80 chords total. The system is useful for brightness measurements and tomographic emissivity, but uncertainties made it insufficient for tomographic reconstruction of temperatures. The system was redesigned and moved to $90°$ toroidal, with cameras at $-22.5°$, $45.5°$, $87.5°$ and $157.5°$, Fig. 2.6. The new set of cameras has 80 individual diodes, with two filters for each of 40 viewing chords, allowing both tomographic emissivity of the whole plasma and two full-diameter T_e profiles for the whole plasma. The entire system is digitized at 500 kHz, but the practical bandwidth is limited to < 20 kHz by the signal-to-noise ratio. The amplifier circuits also impose a limit at higher frequency, between 30 and 100 kHz.

Although Soft X-Ray camera systems have been used to study high frequency mode activity in the past [12], such systems require detection frequencies at greater than twice the mode frequency. Such a thing is feasible, as the primary theoretical limitation of most camera systems is the signal-to-noise ratio. This ratio decreases with the width of temporal binning Δt, but increases with $P(E)$ and decreases with filter thickness. With high bandwidth amplifiers, and at high plasma temperature and thin filter thickness, high frequency $\tilde{\mathbf{T}}_e$ could be observed and correlated with magnetic fluctuations.

The high density of viewing chords makes SXR an ideal diagnostic for equilibrium reconstruction. Direct brightness reconstruction of 2D temperature profiles is under development, and temperature reconstruction can be combined with density profiles to determine pressure profiles for equilibria. If the equilibrium reconstruction model does not adequately handle the two-filter technique, f may still be utilized to determine flux surface shapes, so long as it is a flux function. On MST, this assumption is generally held to be true.

2.2.2 D-Alpha Array

The H-alpha transition is the drop of an electron bound to a hydrogen or deuterium nucleus from excitation level $n = 3$ to $n = 2$. This transition isotropically emits red-colored light at the coherent wavelength of 656.28 nm. Because the dominant fueling gas for MST plasmas is Deuterium, the observed light is at $\lambda = 656.1$ nm, and is referred to as D-Alpha (D_α). The D_α line intensity is described by the equation:

$$\gamma_{D_\alpha} = n_e n_0 \langle \sigma \nu \rangle_{\text{excitation}} \tag{2.5}$$

where n_0 is the neutral deuterium density and $\langle \sigma \nu \rangle_{\text{excitation}}$ is the electron impact excitation reaction rate.

On MST, an array of 16 filtered photodiodes detects D_α light and uses Eq. 2.5 to calculate chord-averaged neutral deuterium density. This output can be inverted to find the two dimensional density profile of background neutrals. Because MST neutral density is heavily edge weighted, 10^{18} m^{-3} in the edge versus 10^{15} m^{-3} in the core, standard Abel inversions have high uncertainties. The neutral particle following code NENE[29] is used to generate several characteristic neutral density profiles based on plasma equilibria and several realistic neutral sources. These profiles are linearly combined to obtain a best fit to the measured D_α emission profile.

While not directly applicable to either Alfvénic frequency mode analysis or equilibrium reconstruction, determination of n_0 is crucial for other diagnostics. The neutral particle analyzers discussed below and the recombination spectroscopy system all measure the products of charge exchange, a process whose reaction rate is governed by neutral density. As the neutral density changes across a plasma shot, the D_α array is used to normalize the signals from these diagnostics, providing better relative calibration.

2.2.3 Advanced Neutral Particle Analyzer

Ions in the plasma can pick up an electron from the background neutral gas, neutralizing them in a process known as charge exchange. The former ion retains its velocity and orientation, but is no longer sensitive to electromagnetic effects, causing it to exit the plasma in a straight line. The particle analyzer is oriented to allow particles with a predetermined pitch, γ_c, to enter. It is also restricted to "fast" particle detection, or ions with $E > 5$ keV, above the high plasma temperature achieved in the machine. After taking into account the fraction that reionize before reaching the wall, f_r, the predicted flux of particles into the detector is [30]:

$$\Gamma_{\text{meas}} = \int_L n_0 n_{fi} \langle \sigma \nu \rangle_{cx} \delta \left(\gamma - \gamma_c \right) \left(1 - f_r \right) dl d\gamma$$

where integration takes place along a line extending from the detector, n_{fi} is the density of fast ions, and γ is the pitch of fast ions along the line. $\langle \sigma \nu \rangle_{cx}$ is the local cross section for charge exchange. The intent of the measurement is to determine $n_{fi} \left(\gamma_c \right)$ along the measured line. Proper interpretation requires knowledge of n_0 and of the orientation of field lines along the chord. Because of this requirement, a full equilibrium reconstruction is necessary. With this information determined, $\langle \sigma \nu \rangle_{cx}$ and f_r can be estimated and a value for $n_{fi} \left(\gamma_c \right)$ can be extracted.

The Advanced Neutral Particle Analyzer (ANPA) is a 20-channel $\mathbf{E} \parallel \mathbf{B}$ analyzer whose energy range is ≈5-40 keV. Its layout is shown in Fig. 2.7. The system is set up to measure hydrogen neutrals and deuterium neutrals simultaneously, each with 10 channels that span the full energy range. This provides an energy resolution of $\approx 1 - 4$ keV, although the energy range and thus the resolution is tunable. The

Figure 2.7: Advanced Neutral Particle Analyzer layout with particle trajectories plotted in purple. From [30].

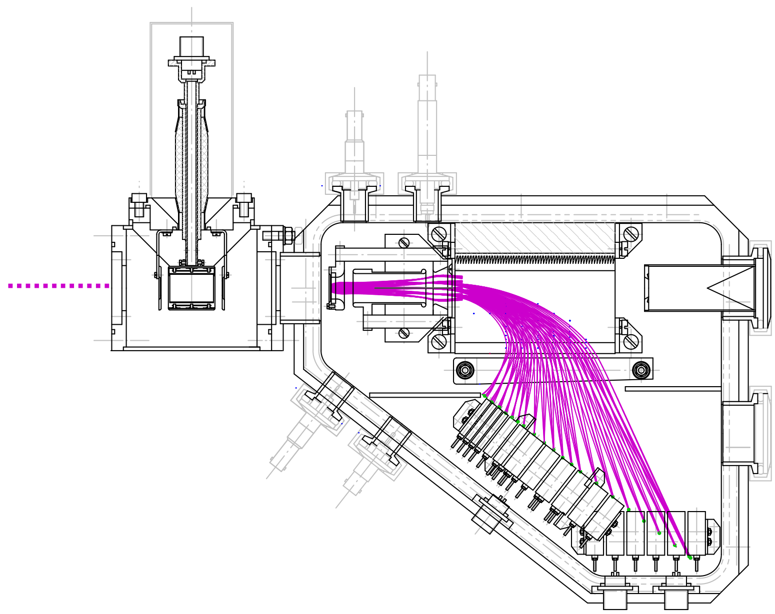

ANPA reionizes incoming neutrals with thin foil stripping cell. A magnetic field perpendicular to the ions' motion causes the ions to bend with different gyroradii due to their energies, according to $r_g = mv_\perp / (|q|B)$. A uniform electric field oriented in the same direction separates deuterium and hydrogen ions due to their different masses. Detector channels are spaced to collect the incoming ions.

The ANPA has been placed at two viewing angles to sample fast ions with different γ_c. The original mount was a radial view at $\phi = 180°, \theta = 7°$. This was used to capture ions moving perpendicular to equilibrium field lines. The second location was at $\phi = 220°, \theta = -19°$, oriented along the magnetic axis. This view was used to study NBI-sourced fast ions traveling parallel to the core magnetic field lines. The frequency of digitization is 1 MHz, but the amplifier circuits have a practical frequency response of 100 kHz.

The pitch-resolved fast ion content is an important quantity for mode analysis. As indicated in Section 1.3, fast ions can couple to waves in the plasma via resonant motion. Although the amplifier response for the ANPA is too slow to resolve Alfvénic frequencies, depletion or enhancement of fast ions on a slower timescale could be indicative of resonant interaction. By performing a measurement in time at several pitches and locations, understanding could be gained about the mechanism and location of mode excitation.

2.3 Laser and Wave-based Diagnostics

Characteristics of plasmas can be determined by launching electromagnetic radiation through them. EM waves may be reflected, absorbed or change phase as they propagate because plasmas have variable indices of refraction. At the atomic level, light may scatter off of the electrons which form one component of the plasma. By injecting EM waves in either form and detecting their properties as they are scattered or exit the machine, values for plasma quantities can be determined.

2.3.1 Far Infra-Red Interferometer-Polarimeter

For a wave with $\omega \gg \omega_c, \omega_p$ propagating perpendicular to the background magnetic field (wave vector $\mathbf{k} \perp \mathbf{B}$) in a plasma, the index of refraction is:

$$\mu_{(k \perp B)} \approx 1 - \frac{1}{2}\left(\frac{\omega_{pe}^2}{\omega^2}\right)$$

where $\omega_{pe}^2 = n_e e^2/\epsilon_0 m_e$ is the plasma frequency and ϵ_0 is the free space permittivity. The wave vector for a given wave is defined as $k = \mu\omega/c$. If one wave is launched through vacuum and another through the same distance in plasma, the different indices of refraction will result in a cumulative phase difference of:

$$\Delta\Phi = \int \left(k_{\text{vac}} - k_{\text{plasma}}\,(l)\right) dl \approx \frac{1}{2\omega c}\int \omega_{pe}^2(l) dl = \frac{\lambda e^2}{4\pi c^2 m_e \epsilon_0}\int n_e(l) dl.$$

Replacing constants with numbers, this equation becomes simple:

$$\Delta\Phi = 2.814 \times 10^{-15} \lambda \int n_e(l) dl$$

If a wave of known vacuum wavelength λ is passed through the plasma, it will undergo a phase shift relative to passing through vacuum. The shift will be due solely to the density of free electrons that it passes through. By subtracting the phases, one determines the line-averaged density $\bar{n}_e = \int n_e(l)dl / \int dl$. With multiple chords and some assumptions about symmetry or additional phase information, $\bar{n}_e$ can be inverted to determine $n_e(r)$.

In a plasma, the index of refraction is not only dependent on plasma density, but varies based on magnetic field strength, light polarization and propagation direction. This quality of optical anisotropy is known as birefringence. When it is associated with a magnetic field, it is known as circular birefringence, and arises due to the Faraday effect. Propagation of any circularly polarized wave along a parallel magnetic field results in a rotation of the wave polarization. The difference in polarization rotations for a right and left handed circularly polarized wave is

$$\Psi = \frac{2\pi}{\lambda} \int \frac{(n_R - n_L)}{2} dl$$

$$= 2.62 \times 10^{-13} \lambda^2 \int n_e(l) \, \vec{\mathbf{B}} \cdot d\vec{\mathbf{l}}$$

If such a measurement is performed in tandem with an interferometry measurement, the inverted $n_e(r)$ profile can be used to find the line-averaged magnetic field parallel to the chord of measurement, $\int \vec{\mathbf{B}} \cdot d\vec{\mathbf{l}}$. In order to measure the Faraday rotation and phase shift simultaneously from the same beamline, two oppositely-polarized beams of slightly different frequency can be launched. The beam polarizations will be rotated in opposite directions. Taking only one component of the polarization, the mean phase change for both beams will be related directly to the index of refraction of the plasma. The difference in phase change will be related to the degree of Faraday rotation as the wave vectors are rotated oppositely.

The Far Infra-Red (FIR) Interferometer-Polarimeter on MST uses a $\lambda = 432\ \mu$m laser, split into 11 vertically-oriented chords[31]. Six of these chords enter the plasma at $\phi = 255°$, at impact parameters $(R - R_0)$ of -32, -17, -2, +13, +28 and +43 cm. Five chords enter the plasma at $\phi = 250°$, at $(R - R_0)$ = -24, -9, +6, +21 and +36 cm, Fig. 2.8. The phase signals are digitized at 6 MHz, but operating in 3-beam mode to obtain simultaneous Faraday rotation and interferometry limits bandwidths to $<$ 300 kHz. The phase resolution for the interferometer is $\approx$ 0.03 radians, which corresponds to $\bar{n}_e \approx 3.5 \times 10^{10}$, less than 0.05% of equilibrium density. Error in the Faraday rotation measurement is $\approx 0.1°$, compared to total rotation of $\Psi < 5°$. Spatial resolution is the spacing between channels, or 7-8 cm. This is adequate to resolve the structure of global perturbations, but may be insufficient for fine structure of local perturbations.

Both capabilities of the FIR system are useful in high frequency mode analysis and equilibrium reconstruction. For mode analysis, the interferometer is capable of measuring line-averaged internal density fluctuations $\tilde{\bar{n}}_e$ in the low Alfvénic frequency range, $f \leq 250$ kHz. With 11 chords, the structure of the density fluctuations can be determined across the plasma. Via correlation analysis, the polarimetry system can determine fluctuating magnetic fields. From internal fluctuations, n and m numbers can be found.

The FIR system provides essential information for 3D equilibrium reconstruction. It is currently used in MSTFIT[24]. 11 chords producing both $\bar{n}_e$ and $\int \vec{\mathbf{B}} \cdot d\vec{\mathbf{l}}$ provide strong constraints on the magnetic field and pressure profiles. While these measurements could be inverted or used to determine the current profile before reconstruction, these processes are equivalent to using them to constrain the equilibrium. Each chord

Figure 2.8: FIR layout with chords passing through the plasma. Image provided by Liang Lin.

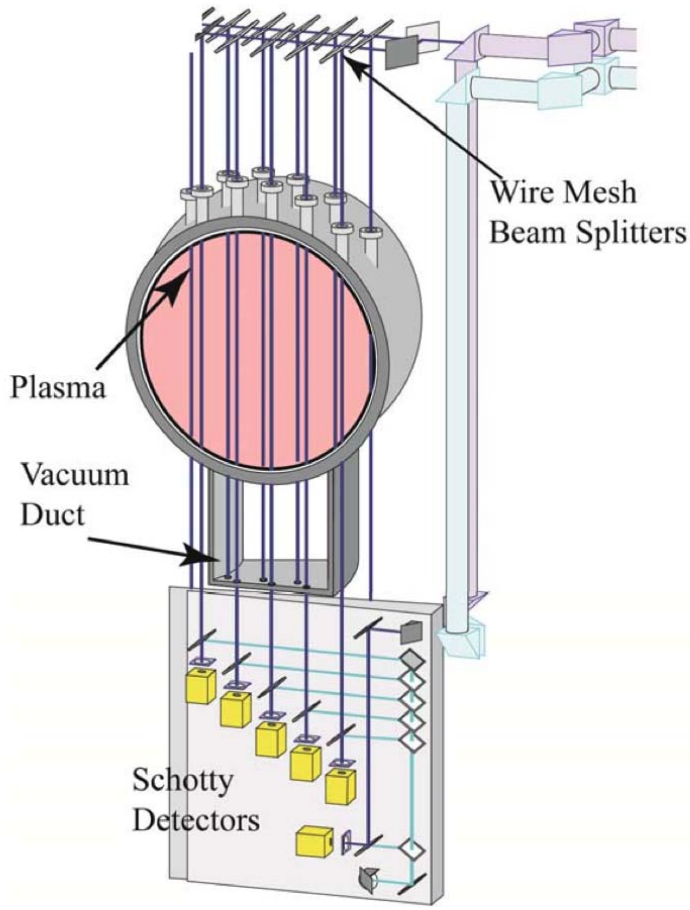

in 3-beam mode provides 2 signals to constrain the fit. The addition of values calculated from those signals (such as the current profile) would be redundant. $n_e \approx n_i$ is a good assumption due to electron motion mirroring charge distribution of ions, so n_i can be inferred from interferometer data. Both the polarimeter and interferometer are included in MSTFIT and V3FIT reconstructions.

2.3.2 CO2 Interferometer

Via the same mechanism as the FIR Interferometer, an additional CO2 interferometer system with $\lambda = 10.6\ \mu$m measures line-averaged density $\bar{n}_e$. A single double-pass laser is located at $\phi = 40°, \theta = -75°$. Due to its shorter wavelength, the CO2 laser has better temporal resolution than the FIR Interferometer, and is digitized at 300 kHz. No polarimetry is measured on the CO2 system, and the reduced complexity from fewer measurements and fewer chords allows it to be operated as a standard diagnostic for all runs. However, as the entire system sits close to the machine itself, offsets and harmonic modulations to the $\bar{n}_e$ signal arise from shaking of the optics board. These offsets are corrected by comparison with a Helium Neon laser.

As it is the same type of measurement, the CO2 laser inhabits the same parameter space as the FIR system. In principle, it can be used to search for $\tilde{n}_e$ in the same fashion, and can be used to constrain the density profile for equilibrium reconstruction. In practice, uncertainty from vibration of the optics board leads experimenters to rely solely on the FIR system for precise measurement. Nonetheless, with a proper pre-run calibration of the two systems, they could be operated simultaneously to acquire an additional toroidally separated data point. The CO2 interferometer is included in MSTFIT reconstructions.

2.3.3 Thomson Scattering

When an electron is struck by a photon with energy well below the rest mass energy of the electron, it is accelerated along the direction of the photon's electric field. An electron initially at rest oscillates along this same direction, forming a dipole oscillator that radiates light with intensity $I \propto \sin^2(\chi)$, where χ is the angle between the incident and scattered wave vectors, Fig. 2.9. The cross section for this interaction is

$$\sigma_{\text{Thomson}} = \frac{8\pi}{3}\left(\frac{e^2}{4\pi\epsilon_0 m_e c^2}\right)^2 = 6.65 \times 10^{-29}\ \text{m}^2$$

where the term in parentheses is the classical electron radius [32]. When passing a beam of light through a plasma, many photons are interacting with many electrons,

Figure 2.9: Thomson scattering off of an electron. The light strikes the electron, accelerating it along the direction of the electric field. The electron then re-emits the light with the same polarization.

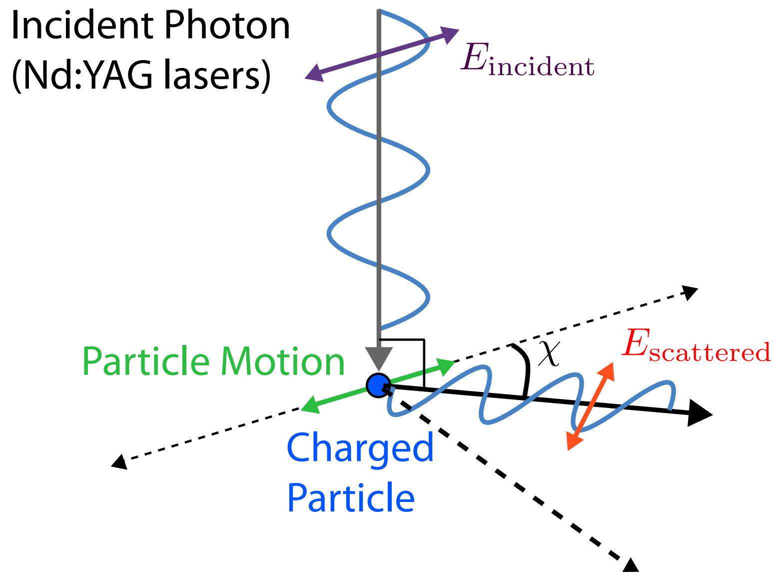

resulting in a total scattered power of $P_{\text{total}} = \sigma_{\text{Thomson}} I_{\text{beam}} N_e$, where I_{beam} is the energy flux per area per time, and N_e is the total number of electrons within the beam path.

If the electrons responsible for scattering are in motion, the emergent light will be Doppler-shifted from its source by an amount proportional to the electron velocity. If the beam of light is sufficiently intense to pass all the way through a plasma, viewing this beam at different locations along its length will yield light that is Doppler-shifted by the local electron velocity. The velocity of electrons is assumed to be isotropic, and the resulting Doppler shift corresponds to the local plasma temperature. From a single beam, multiple $T_e(r)$ may be measured at an arbitrary number of locations, provided there is sufficient viewing resolution to distinguish between scattering volumes.

On MST, the Thomson scattering system uses a fast pulse, high intensity beam generated by one of two collinear laser beams. The beam enters at $\phi = 222°, \theta = 90°$,

Figure 2.10: The trajectories for the scattering light from Thomson scattering through the collection lens and into the collection fibers. From [32].

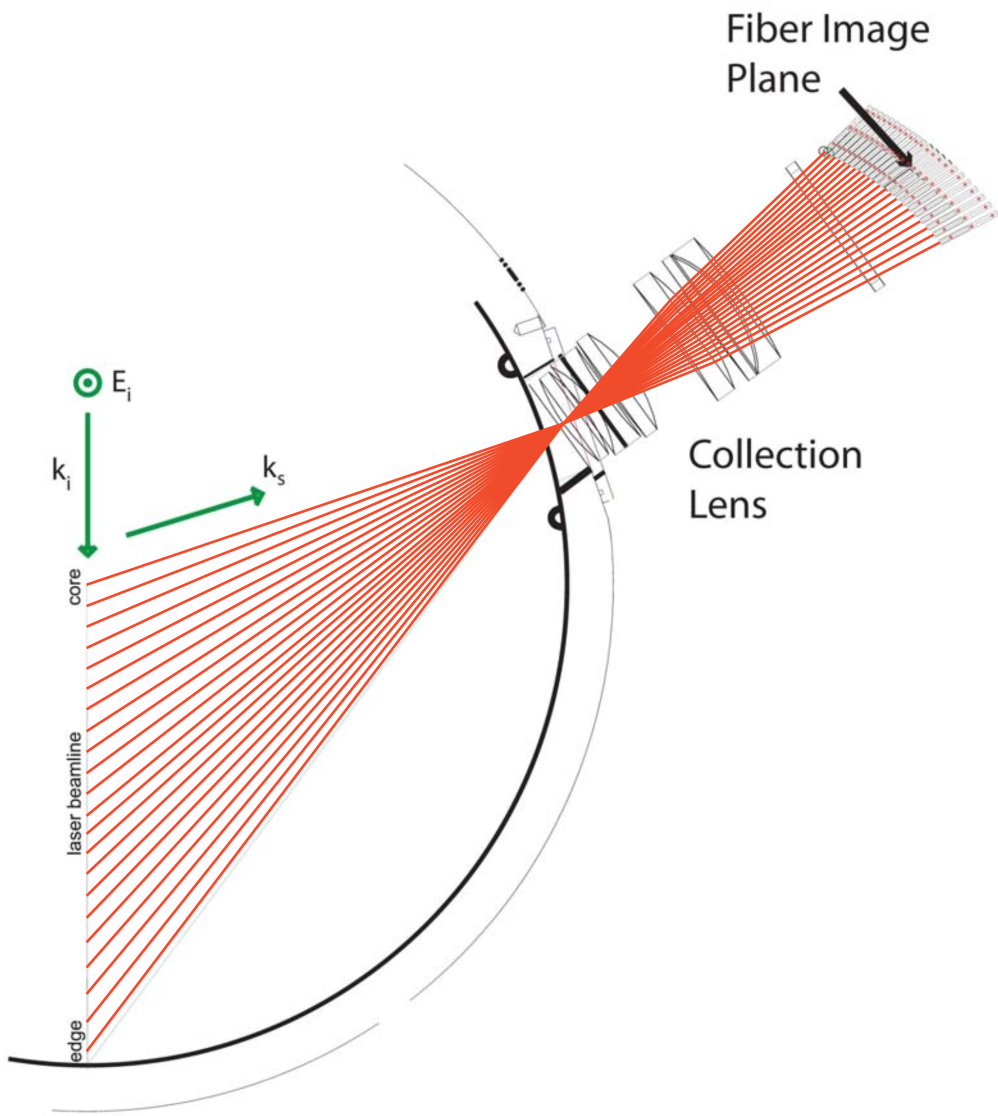

at the top of the machine. 21 fibers monitor locations vertically, going from $r \approx 0$ to $r = a$ at $\theta = 270°$, in a line below the magnetic axis. The viewing port is located at $\theta = 20°$, where a lens focuses scattered light from all viewing angles onto fibers to be piped to polychromators, Fig. 2.10. The system can operate at multiple speeds. As pulse length of the laser is only 9 ns and the resolution of the amplifying avalanche photodiodes (APDs) is 200 ns, temporal resolution of measurements in a single plasma discharge is limited by the repetition rate of the lasers and not the temporal width of the measurement[32]. With the current Thomson scattering system, this speed is 80 μs, or 40 μs by interleaving the two laser beams. This corresponds to a frequency of 25 kHz for ≤ 8 laser pulses in a row. Temperature resolution varies from 10-100 eV depending on signal level.

The Thomson scattering system can measure at frequencies high enough to detect high frequency temperature fluctuations, $\tilde{T}_e$, although correlation with the toroidal array is necessary. The measurement location is a point and not a chord, so information can be readily used to generate $\tilde{T}_e(r)$ without inversion. Along with $\tilde{n}_e$, by the ideal gas law,

$$\tilde{p}_e = k_B \left(T_e \cdot \tilde{n}_e + \tilde{T}_e \cdot n_e + \tilde{T}_e \cdot \tilde{n}_e \right)$$

provides the magnitude of electron pressure fluctuations. Although the described waves are incompressible shear waves, they will cause will cause measurable $\tilde{p}_e$ on surfaces with finite ∇p_e . Alfvénic waves result from the movement of ions, so electron pressure fluctuations are assumed to be coupled to ion motions through charge balance. The waves are sufficiently slow that this is a good assumption.

As with density, temperature is an important quantity for equilibrium reconstruction. The ∇p term in the magnetic pressure balance equation requires knowledge of both T and n, both of which refer to the full (ion and electron) quantities. Although $n_e \approx n_i$ is a good assumption due to charge balance, $T_e = T_i$ can only be achieved through many ion-electron collisions and thus is not always a good assumption. Other diagnostics must be used in concert with Thomson scattering to determine the full pressure. Thomson scattering is included in both MSTFIT and V3FIT reconstructions.

2.4 Particle Beam Diagnostics

In addition to beams of light, beams of particles can be used to measure plasma properties. Much like the photons in light beams, neutral particles have a multitude of ways in which the plasma might affect them. Charge exchange stimulates light emission with electrons from previously neutral atoms and makes the newly-created ions sensitive to the plasma potential, changing their paths. Neutral atoms can be scattered off of the background plasma, or can pass through but emit light from energy level jumps of their electrons. The emitted light or particles themselves can be collected in large numbers to build a picture of the plasma.

2.4.1 Charge Exchange Recombination Spectroscopy and Diagnostic Neutral Beam

Each charge exchange not only produces a fast neutral particle that exits the plasma rapidly, but this particle also generates light as the electron de-excites in its new bound state. The wavelength of emitted light from this electron is governed by the mass of the receiving ion and the available energy levels, a proxy for the degree of ionization. These lines are well-known and documented for all relevant ion species to MST plasmas [33]. By filtering light to detect only one line, a diagnostic of charge exchange for a single ion species is produced. A photomultiplier array viewing the plasma receives a chord-averaged brightness of this particular line, similar to the SXR measurements.

When the emitter is in motion relative to the point of observation, the observed light is Doppler-shifted from its rest wavelength by $\Delta\lambda = \lambda_0 (v/c)$, where v is the relative velocity of the emitter along the line of observation, λ_0 is the rest wavelength, and c is the speed of light. Emitters moving away from the point of observation will increase λ, and emitters moving towards it will decrease λ. A population of emitters in isotropic motion, as in a gas at thermal equilibrium, would then broaden the distribution of observed wavelengths. A coherent directional motion along the line of sight would shift them uniformly. Because the wavelengths are a direct proxy for a velocity distribution, the observed distribution is a Gaussian function,

$$f(\lambda) \propto \exp \frac{-(\lambda - \lambda_c)^2}{2\sigma^2}$$

where λ_c and σ provide the flow velocity and temperature, respectively. The first term,

$$\lambda_c = \lambda_0 + \Delta\lambda = \lambda_0 \left(1 + \frac{v}{c}\right)$$

comes from the Doppler-shifted wavelength due to flow, and determines the peak shift. The second term,

$$\sigma = \frac{\lambda_0}{c}\sqrt{\frac{kT}{m}}$$

is a result of the Doppler-broadening due to the average particle temperature, T, and determines the peak width.

In a plasma, a high level of background light emission complicates the measurement, making a passive system impractical. By simultaneously viewing off and along the path of a beam of neutral particles whose cross section for Carbon VI charge exchange peaks at the beam injection energy, comparison of the two measurements yields a more readily distinguishable set of lines. On MST, a hydrogen-atom neutral

Figure 2.11: A diagram of the DNB and both toroidal and perpendicular CHERS views. Images created by Steve Oliva and Rich Magee.

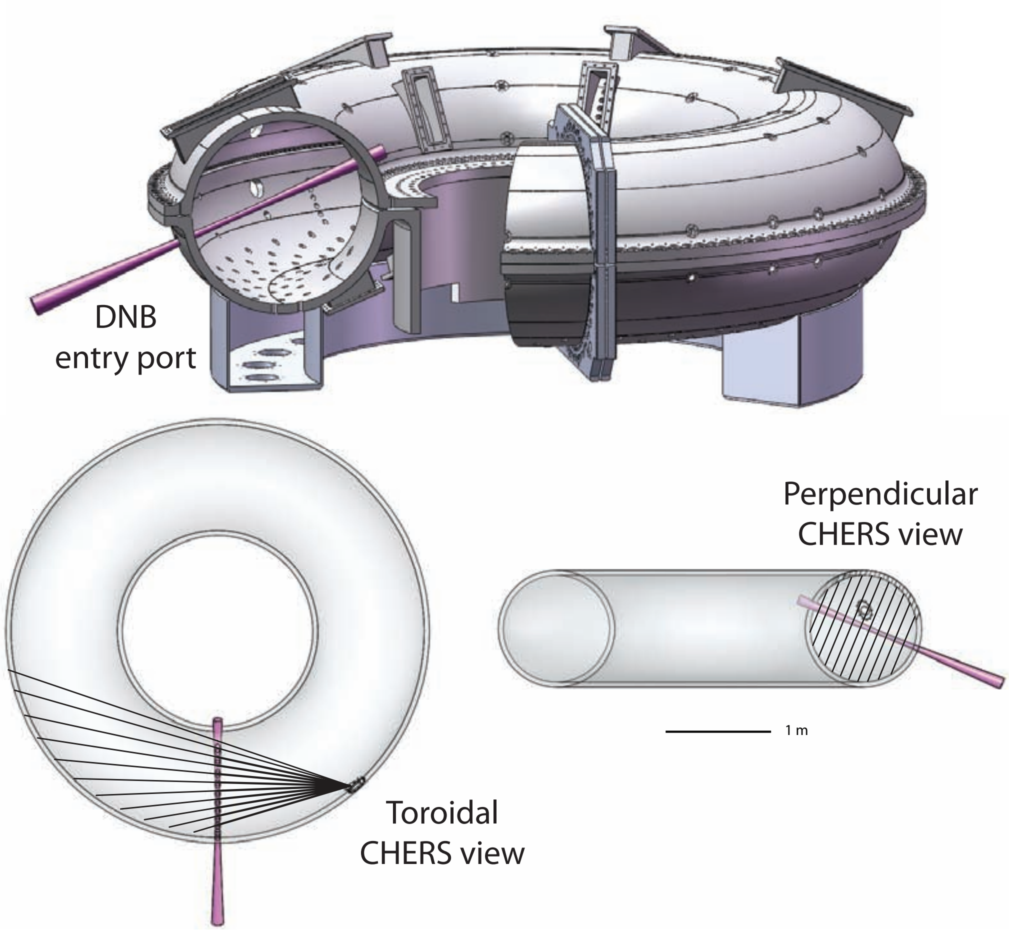

beam is injected radially from $\phi = 270°, \theta = -22.5°$, with a beam energy of $E = 50$ keV and a current of $I_{\mathrm{beam}} = 5$ A. There are 11 viewing locations oriented perpendicular to the beam, each location containing one view along the beam and one view just off the beam for comparison, Fig. 2.11 [34]. At present the system has only 2 photomultiplier arrays, so only one location may be monitored per shot. The most common measurement has been the Carbon VI line at $\lambda_0 = 343.38$ μm, although other wavelengths have been examined[35]. A last location views the magnetic axis tangentially from $\phi = 312°$, Fig. 2.11, with the off-beam view passing just below the active view. The combination of beam and views is referred to as the Charge

Exchange Recombination Spectroscopy (CHERS) system on MST.

The CHERS system has some use for diagnosing 3D fields, but its function in equilibrium reconstruction is not easily implemented. Impurity ions are sensitive to magnetic islands, which are not included in the flux surface representation presented in Section 1.2. A chord viewing the predicted location of the helical axis could be used as an independent confirmation of the phase of a helical equilibrium. In tokamaks, a second impurity ion species with temperature T_z and density n_z has been used as a component of the total pressure. Well-calibrated charge exchange systems have been used to constrain the equilibrium in a similar fashion to the electron temperature and density[36]. This diagnostic is not implemented as a constraint for MSTFIT or V3FIT.

2.4.2 Motional Stark Effect

Traversing magnetic fields alters the wavelength of light emitted due to electron energy transitions. As the neutral atoms from the DNB impact background plasma electrons, the bound electrons in the atoms gain energy and jump into new shells. A charge moving across a magnetic field, as in MST, sees an effective electric field of $\vec{\mathbf{E}}_{\text{eff}} = \vec{\mathbf{v}} \times \vec{\mathbf{B}}$. Due to the Stark effect produced by E_{eff}, the many spectral lines of light emitted from dropping down in energy will separate in wavelength. These lines will have a wavelength separation proportional to the strength of $\vec{\mathbf{E}}_{\text{eff}}$ and thus of $\vec{\mathbf{B}}_{\perp v}$. If $\vec{\mathbf{v}}$ is known, a camera observing a single point along the beam could determine $\vec{\mathbf{B}}_{\perp v}$, where in an axisymmetric plasma with a radially-injected beam, $\vec{\mathbf{B}}_{\perp v} \approx \vec{\mathbf{B}}$.

The effective electric field $\vec{\mathbf{E}}_{\text{eff}}$ is a vector, and its orientation alters the overall polarization of emitted light. By measuring this polarization, additional information about the pitch of the magnetic fields is obtained. The safety factor profile, $q(r) = rB_\phi/RB_\theta$ is a measure of this pitch and is thus directly determined the polarization

Figure 2.12: A diagram of the DNB and MSE views. Image from [34].

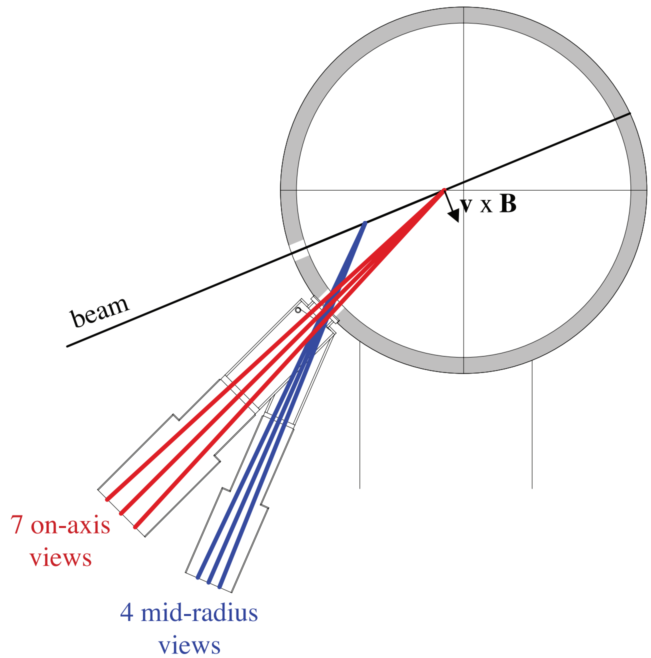

of $\vec{\mathbf{E}}_{\text{eff}}$. Without the polarization information, $|\mathbf{B}|$ can still be extracted from the peak shifts.

On MST, the MSE diagnostic views the previously described DNB at two locations [34]. The cameras are located at the same toroidal location as the beam, but view from $\theta = -45°$. One camera views the on-axis magnetic field, and the other views the beam at mid-radius, Fig. 2.12. Temporal resolution is 100s of μs, and spatial resolution is ≈ 5 cm for both views.

Determination of the q profile is crucial for locating mode resonances. MSE is too slow to detect magnetic fluctuations, but has been used on tokamaks to determine how q_0 varies with mode frequency.

Equilibrium reconstruction directly depends on magnetic field information, so MSE is a crucial diagnostic. Point measurement of the pitch of a field line in the helical configuration provides a powerful constraint on the phase and flux surface shape. Because the helical axis has a shift, both measurements from MSE will likely be off-axis measurements, where field line pitch can be determined via the same method. With a pitch resolution off-axis of $\pm 10°$ [37], the diagnostic can provide bounds on q. The current on-axis view is not set up to handled polarized light. MSE is not currently included in V3FIT equilibrium reconstructions, but is included in MSTFIT.

2.4.3 Rutherford Scattering

While viewing light produced from electron transitions after charge exchange allows a measurement of the impurity ion temperature, tracking the scattering of a monoergetic neutral particle beam provides information on the bulk ion temperature. Divergence due to Rutherford scattering of a tightly focused beam of neutral particles will carry a dependence on the temperature of the plasma. In the case of an ideal beam, the energy distribution of scattered particles is

$$f\left(E\right) = C\left[\frac{Z_p Z_b e^2}{4\pi\epsilon_0}\right]^2 \frac{1}{E_0^3}\sqrt{\frac{\pi E}{\mu T_i}}\frac{1}{\sin^4\theta}\exp\left\{\frac{-\left(E - E_0\left(1-\mu\sin^2\theta\right)\right)^2}{4\mu E_0 T_i}\right\},$$

where Z_p and Z_b are the plasma ion and beam particle masses, and E_0 is the initial beam energy [38]. C is a scaling factor that includes various experimental considerations. It is clear from the formula that T_i correlates directly with the width of the energy distribution. By detecting the spread in energies at a given angle, a direct inference of the temperature of the bulk plasma can be made. The chosen angle must not be in line with the beam as the signal from scattered particles is desired.

On MST, the Rutherford scattering system is located at $\phi = 180°$, where the beam fires vertically upward from $\theta = 270°$. Two analyzers are located at $\theta = 79.8°, 100.2°$, both $10.2°$ displaced from a directly vertical position, Fig. 2.13. The analyzers view the beam at a position ≈ 15 cm below the machine mid plane, and the view extends

Figure 2.13: The Rutherford scattering set-up on MST. The beam passes radially through the plasma. The neutral analyzers sample a volume below the midplane. from [39].

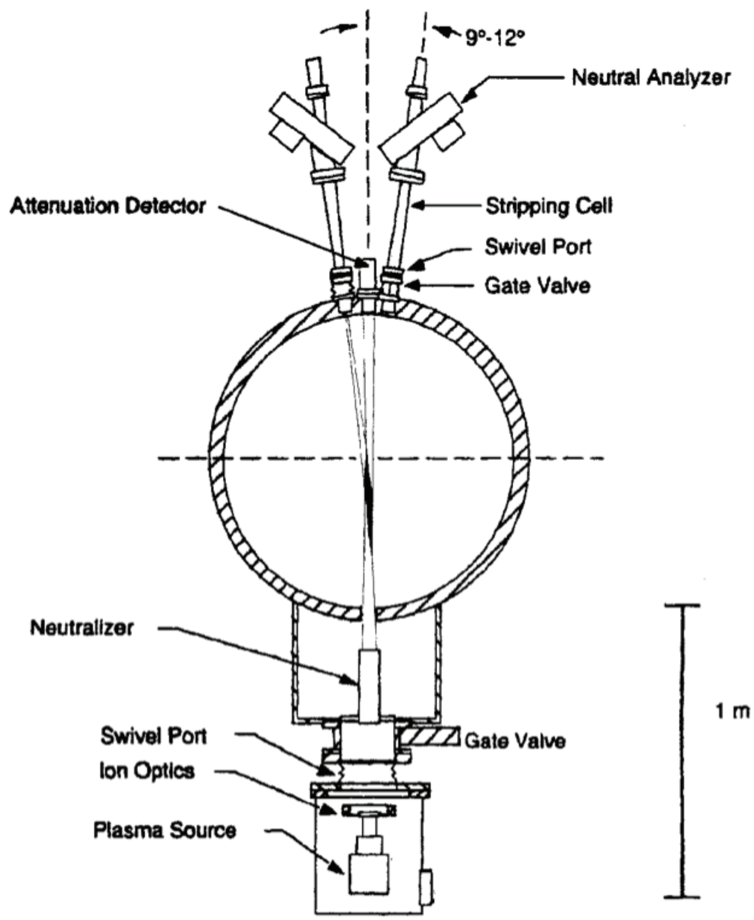

15 cm in either direction, just touching the axis. Temporal resolution is up to 10 points per shot due to signal levels, about 200 Hz, although the data are digitized at 1 MHz before smoothing.

Ion temperature is a difficult quantity to measure in plasmas, but contributes strongly to the plasma pressure, influencing the ∇p term in MHD equilibria. Although the resolution of the Rutherford scattering diagnostic is too poor to distinguish flux surface, volume-averaged T_i provides a constraint on the ion pressure. The total pressure is $p = k_B\left(n_eT_e + \Sigma n_iT_i\right)$, with the sum over ion species in the plasma. If charge neutrality is assumed and the pressure due to non-bulk ions is assumed to be small, T_i is the final pressure constraint after electron diagnostics. Rutherford scattering signals are not included directly in MSTFIT or V3FIT. Measurements are indirectly incorporated by assuming the ion pressure is linearly related to the electron pressure using previously measured ratios.

2.4.4 Heavy Ion Beam Probe

An ion passing through a plasma can undergo electron impact ionization by collision with plasma electrons. In a region of finite potential, the stripped electron will remove $\Delta E = -e\phi_l$ from the ion, where ϕ_l is the local electrostatic potential. Loss of this electron will alter the charge of the ion by $+e$, changing the curvature of its trajectory through the plasma. If the ion is heavy enough, the magnetic field will not be sufficient to confine it. Depending on the point of ionization, the plasma-ionized heavy ion will exit the plasma at a correspondingly different pitch and location, Fig. 2.14. By injecting a beam of heavy ions into the plasma and collecting at a port that "views" a particular location of ionization, the change in energy can be measured and thus the ϕ_l at that location can be determined via the formula,

$$\phi_l = \frac{W_d - W_i}{q_s - q_p}$$

where $(W_d - W_i)$ is the change in energy from source to detector of the beam ions, and $(q_s - q_p)$ is the change in charge at ionization. This measurement is finely localized in time if the flight time of the ions is known to greater accuracy than the temporal resolution of the system.

While the individual ion energy decreases proportionally with the electrostatic potential, the beam current at the detector is a function of the plasma density at the location of ionization, $I_s \propto n_{e,l}$. The more electrons in the sample volume to impact

Figure 2.14: Heavy Ion Beam Probe mock-up. Image provided by Peter Fimognari.

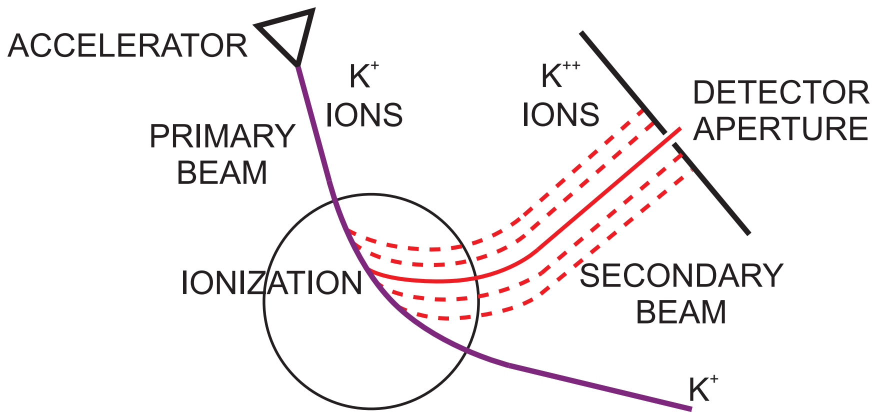

on the ions, the more ionizations will occur in the sample volume, thus directing more secondarily-ionized products to the detector.

On MST, the Heavy Ion Beam Probe injects a $\sim$ 100 μA beam of $<$ 200 keV sodium or potassium ions which take a three dimensional path through the plasma [40]. Their time-of-flight is $\sim$ 5 μs. The injector is located at $\phi = 128°, \theta = 105°$, with the detector plates for 3 paths located at $\phi = 138°, \theta = 19°$. Three points within the plasma can be sampled simultaneously, and the beam can be steered to change the radius at which sampling is performed. The samples are performed at 1 MHz, with a spatial resolution of $\sim$ 1 cm and the ability to resolve potential fluctuations of $\tilde{\phi} \approx 2 - 5$ V. The system been calibrated for fluctuating relative electron density measurements $\tilde{n}_e/n_e$, but requires the FIR Interferometer to determine absolute fluctuation levels.

The HIBP system has the capability to measure the electrostatic potential fluctuation amplitude, $\tilde{\phi}$, for high frequency waves up to 500 kHz. A point measurement of this quantity can be correlated with magnetics to determine relative phase. Point measurements of $\tilde{n}_e$ can be correlated with interferometry to resolve internal poloidal

Figure 2.15: Heavy Ion Beam Probe on MST. From [40].

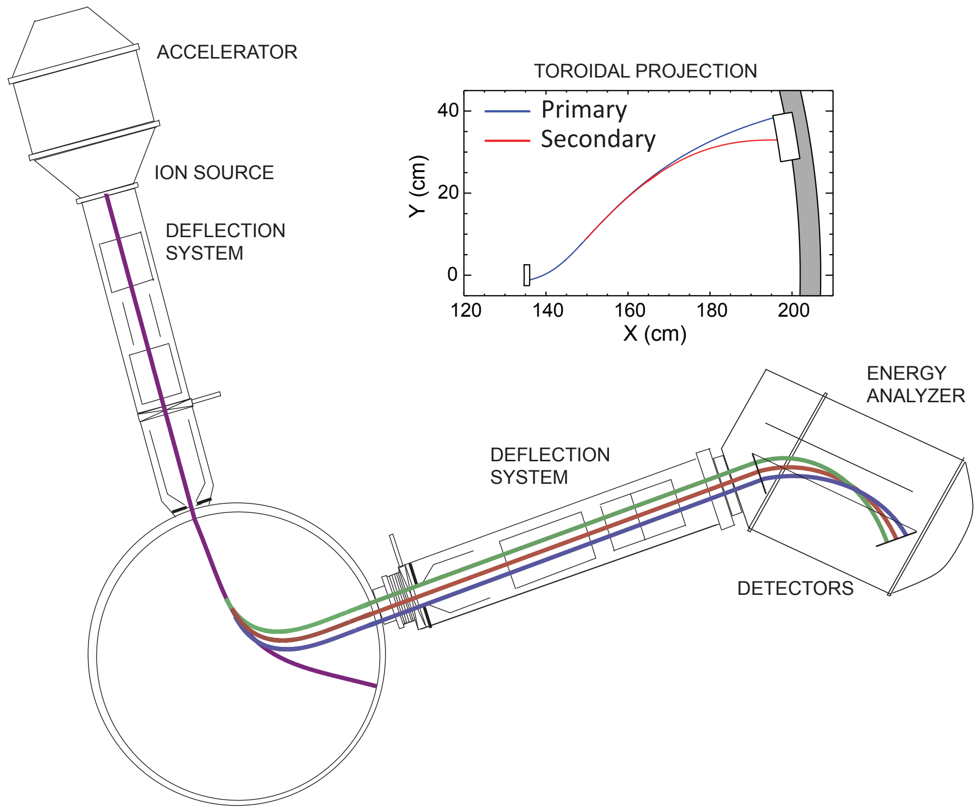

harmonics. The TJ-II heliac has performed these measurements successfully [41].

The flight path of the beam is a stringent check of the equilibrium. Only a small subset of possible fields bend the HIBP ions correctly into the detector. If the HIBP sees a signal, the flight path can be calculated during equilibrium reconstruction as a check. If the calculated flight path does not enter the detector, the equilibrium is not correct. This has been implemented in MSTFIT, but not in V3FIT.

2.5 Summary

A number of diagnostics are currently in operation on MST that can provide data for equilibrium reconstruction and mode analysis. Table 2.2 summarizes those relevant to equilibrium reconstruction, a subset of which are currently employed. Table 2.3 summarizes those relevant to Alfvénic frequency mode analysis.

Table 2.2: MST Equilibrium Reconstruction Diagnostics

Diagnostic	Measured	ϕ	Geometry
Flux Loop	$\langle B_\phi \rangle$	60°	Circle at $r = 0.52$
Rogowski Coil	I_p, $B_{\theta w}$	60°	Circle at $r = 0.52$
Magnetic Arrays	$\mathbf{B}(a)$	Tab. 2.1	Triplets
Probes	$\mathbf{B}(r < a)$	Various	Point
SXR Cameras (Old)	T_e, ϵ	300°	$\theta_{\text{view}} = -45°, 45°, 75°, 165°$
SXR Cameras (New)	T_e, ϵ	90°	$\theta_{\text{view}} = -22.5°, 45.5°, 87.5°, 157.5°$
FIR Interferometer	$\bar{n}_e$	255°	$R - R_0 = -32, -17, -2, 13, 28, 43$
FIR Interferometer	$\bar{n}_e$	250°	$R - R_0 = -24, -9, 6, 21, 36$
FIR Polarimeter	$\overline{n_e B_z}$	250°/255°	Same as Interferometer
CO2 Interferometer	$\bar{n}_e$	40°	r chord from $\theta_{\text{in}} = -75°$
Thomson Scattering	T_e	$\phi = 222°$	21 pts, $Z = 0.01$ to -0.45, $R = 1.5$
DNB		270°	Radial from $\theta = -22.5°$
ChERS $\parallel$	T_i (imp.)	312°	$\theta = 180°$ viewing DNB at axis
ChERS $\perp$	T_i (imp.)	270°	11 points viewing $\perp$ to DNB
MSE Camera	$\mathbf{B}, \lvert B \rvert$	270°	DNB points viewed from $\theta = -45°$
Rutherford	T_i	180°	$\theta_{\text{beam}} = 270°$, $\theta_{\text{view}} = 79.8°, 100.2°$
HIBP	ϕ	$128°_{\text{in}}, 138°_{\text{view}}$	$\theta_{\text{in}} = 105°, \theta_{\text{view}} = 19°$

Table 2.3: MST Alfvén wave Diagnostics

Diagnostic	Measured	f_{Nyquist}	Localization
Magnetic Arrays	$\tilde{B}_\phi, \tilde{B}_\theta, \tilde{B}_r$	1 MHz	100+ Points
Dense Array	$\tilde{B}_\phi, \tilde{B}_\theta$	3 MHz	4 Points
FIR Interferometer	$\tilde{n}_e$	1 MHz	11 Chords
FIR Polarimeter	$\tilde{n}_e B_z + n_e \tilde{B}_z$	1 MHz	11 Chords
CO2 Interferometer	$\tilde{n}_e$	300 kHz	Chord
ANPA	$\Gamma_{E>2\text{ keV neutral}}$	50 kHz	Chord View
Thomson Scattering	$\tilde{T}_e$	12.5 kHz	21 Points
HIBP	$\tilde{\phi}, \tilde{n}_e/n_e$	500 kHz	Scannable Point

Chapter 3

Equilibrium Reconstruction

A plasma equilibrium is a necessary starting point in order to compute the Alfvén continuum in a plasma. In the search for wave eigenmodes, the continuum provides a map of wave resonances that aides in mode characterization.

Plasma equilibria provide a basis to compare diagnostic measurements based on flux functions and serve as the starting point for a number of computational analyses. Equilibrium reconstruction on MST has been historically done using MSTFIT, a Grad-Shafranov reconstruction code. However, a number of mature analysis routines rely on output files from the Variational Moments Equilibrium Code (VMEC), a fully three-dimensional equilibrium solver[42]. VMEC has been adapted to reconstruct RFP equilibria on MST. The modifications to VMEC allow for it to be utilized with V3FIT to reconstruct non-axisymmetric plasmas. The resultant 3D equilibria can likewise be processed using these analysis routines.

3.1 History of Equilibrium Reconstruction on MST

Before equilibrium reconstruction from diagnostic signals was done, several cylindrical models were successively employed in order to model RFP equilibria from experiment. The models all possess the common feature of fitting the $\lambda =$ constant consequence of Eq. 1.21. The models are modified to account for experimental observations of zero current at the plasma boundary, implying $\lambda \to 0$ at the edge. A thorough account of all of these models is made in the Anderson thesis[24].

MSTFIT was developed by Jay Anderson as the next logical step beyond the 1D models, and was documented in his thesis in 2001. The reconstruction takes a guess from the Modified Polynomial Function Model as its starting point, then performs a χ^2 minimization to match observed diagnostic signals. The reconstruction routine was based on the EFIT tokamak equilibrium reconstruction code.

MSTFIT uses an iterative routine to solve the Grad-Shafranov equation with poloidal flux as the ordinate,

$$J_\phi = \frac{2\pi F F'}{\mu_0 R} + 2\pi R P' \tag{3.1}$$

where J_ϕ is the toroidal current density, R is the distance to the machine center, $F = RB_\phi$ and P is the pressure. This solution takes place on an up-down symmetric triangular mesh grid, to which the diagnostic signals are mapped. The computed equilibrium then undergoes a χ^2 Amoeba [24] minimization with respect to the available plasma diagnostics. MSTFIT performs this comparison by generating synthetic signals for each of the included diagnostics.

3.2 Variational Moments Equilibrium Code (VMEC)

The Grad-Shafranov equation used in MSTFIT is an axisymmetric application of the more general radial force balance equation,

$$\vec{\mathbf{J}} \times \vec{\mathbf{B}} = \nabla p$$

which describes the current, magnetic field and pressure of a plasma in equilibrium. VMEC satisfies this equation by minimizing the total magnetic and thermal energy of a plasma [42],

$$W_p = \int_{\Omega_p} \left(\frac{1}{2\mu_0} B^2 + p \right) dV.$$

This minimization is done by modifying the spectral components that describe a finite number of flux surfaces. The coordinates for a flux surface, R_ψ, Z_ψ and λ_ψ are decomposed into their spectral components,

$$R_\psi = \sum_{m,n} R_{mn}(s) \cos(m\theta - n\xi)$$

$$Z_\psi = \sum_{m,n} Z_{mn}(s) \sin(m\theta - n\xi)$$

$$\lambda_\psi = \sum_{m,n} \lambda_{mn}(s) \sin(m\theta - n\xi)$$

where m and n are the poloidal and toroidal mode numbers of the spectral mode, ξ is an index that maps directly to toroidal angle, and λ_ψ is a normalization function used to truncate the Fourier series at a discrete number of harmonics. The radial-like coordinate s increases from the magnetic axis to the edge. For axisymmetric cases, only the $R_{0,0}$, $R_{m,0}$ and $Z_{m,0}$ terms are important, as toroidal angular dependence is removed. For circular flux surfaces, $R_{1,0} = Z_{1,0}$ and no higher-m terms are included. R and Z each only have one sinusoidal term because the equilibrium is assumed to be in stellarator coordinates, with the helical axis outboard at $\phi = 0°$.

The solution algorithm for VMEC is the equivalent step to the Grad-Shafranov solver in MSTFIT. While VMEC includes a more general set of physics and requires more computation time, it is only an equilibrium solver. Linkage to diagnostics is performed separately by codes with χ^2 minimization routines, such as STELLOPT and V3FIT [43, 44]. These codes initialize VMEC and perform similar loops to those found in MSTFIT, generating equilibria and minimizing the difference between synthetic and measured signals.

The required inputs for VMEC are: a rotational transform profile $\iota(s) = 2\pi R B_\theta / r B_\phi$, a pressure profile $p(s)$, a specification of the total toroidal flux Φ_{B_ϕ} or the total toroidal plasma current I_p, and some geometric specifications for the system. The mesh size and number of harmonics to be included may be specified alongside other parameters for the fit and minimization. For three-dimensional reconstructions, the number of field periods may be specified beforehand, as well as harmonics of the last closed flux surface (LCFS) if known.

VMEC has been used on a number of devices over the years, including stellarators [44, 45], tokamaks [46], and more recently the RFP [47]. It has proven to be a fast code for equilibrium reconstruction.

3.2.1 Modifications for the RFP

Although the choice between poloidal and toroidal flux is arbitrary for tokamaks and stellarators, toroidal flux ψ_t was initially chosen as the coordinate linked with s in VMEC reconstructions. When RFX-mod reported their findings on the Single Helical Axis (SHAx) state [48], work began to modify VMEC to function in poloidal flux.

A Jacobian, $\sqrt{g}$, is used to convert between flux coordinates and real space coordinates. It is applied before minimization to convert cylindrical inputs, and can be applied again after minimization to transform answers back to real space. Flux is linked to the coordinate s and not explicitly included in the calculation, so only the transformation must be modified. For toroidal flux,

$$\sqrt{g}_t = \frac{B_\phi^{\mathrm{co}} + \iota B_\theta^{\mathrm{co}}}{B^2}$$

where B_ϕ^{co} is the covariant toroidal field, B_θ^{co} is the covariant poloidal field, and $\iota = 2\pi/q$ is the rotational transform. For poloidal flux,

$$\sqrt{g}_p = \frac{qB_\phi^{\mathrm{co}} + B_\theta^{\mathrm{co}}}{B^2}.$$

Post-reconstruction routines that require the Jacobian and flux to convert to cylindrical or cartesian coordinates, but do all calculations in real space, need only switch their inputs to accept the new poloidal outputs of VMEC. In an RFP, $q = 0$ at the reversal surface, implying $\iota \to \infty$. Therefore, the rotational transform input must be modified. In RFP mode, VMEC accepts the q-profile as its input instead of the ι-profile.

In order to maintain the high degree of confidence in fits for axisymmetric plasmas, a χ^2 minimization algorithm was **not** applied to VMEC equilibria. Instead, the full MSTFIT routine was used to reconstruct these equilibria, and then the output parameters were fed as inputs into the VMEC fit. Recall that VMEC is not explicitly compared to signals as the MSTFIT loop is, so appropriate comparison is made between equilibrium quantities of the two routines when run on the same q-profile, flux, and plasma current. Pressure, magnetic field and flux surface profiles are compared and are in good agreement, Fig. 3.1.

3.2.2 AE3D and STELLGAP

In order to calculate the Alfvén continuum, a compressionless, reduced MHD equation is solved in Boozer coordinates. The Alfvén continuum solution routine Stellgap

Figure 3.1: Comparison of VMEC and MSTFIT axisymmetric equilibria.

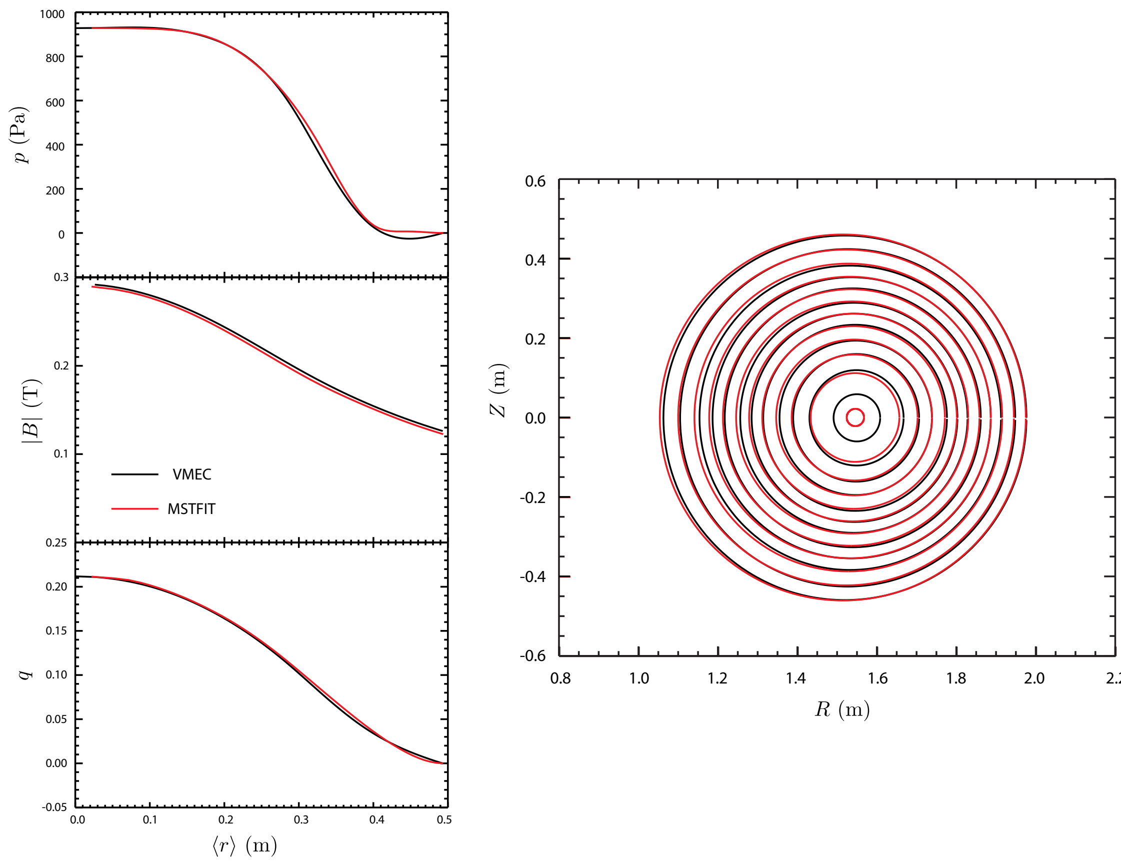

and the eigenmode calculation routine AE3D are codes developed for this purpose by Don Spong at Oak Ridge National Laboratory [49, 50]. Both codes rely on XMetric, a routine that prepares matrix elements from the Boozer coordinates output by Booz-Xform, which is contained in the VMEC code suite. It was deemed much more time-consuming to replicate these procedures for MSTFIT than to adapt VMEC for the RFP, so they remain tied to the VMEC code. It should be noted that familiarity with Booz-Xform and other codes associated with VMEC presents significant opportunity for collaboration with other machines.

STELLGAP

Using the formulation presented by Salat and Tataronis [51], the shear Alfvén continuum can be generated. This treatment starts with reduced MHD in the pressureless limit and generates two eigenvalue equations that correspond to field-line localized solutions and radial surface-localized solutions. The latter equation is traditionally associated with solutions for the Alfvén continuum,

$$\mu_0 \rho_m \omega^2 \frac{|\nabla\psi|^2}{B^2} E_\psi + \mathbf{B}\cdot\nabla\left[\frac{|\nabla\psi|^2}{B^2}\left(\mathbf{B}\cdot\nabla\right) E_\psi\right] = 0, \tag{3.2}$$

where ρ_m is the mass density, ω is a radial frequency, and E_ψ is the covariant ψ component of the electric field. Using the Fourier expansion,

$$E_\psi = \sum_{j=1}^{L} E_\psi^j \cos\left(n_j\zeta - m_j\theta\right),$$

and transforming the system to Boozer coordinates, the equation can be recast as

$$\omega^2 \overleftrightarrow{A}\mathbf{x} = \overleftrightarrow{B}\mathbf{x}$$

where $\mathbf{x} = \left[E_\psi^1, E_\psi^2, E_\psi^3 \cdots E_\psi^L\right]$. The equation is now a matrix eigenvalue solution problem, with the ω^2 values as eigenvalues. The code Stellgap diagonalizes this matrix and finds eigenvalue solutions at a range of ψ locations for a range of n and coupled-m modes. These solutions are the shear Alfvén continuum modes, whose flux surface location, frequency and mode numbers are outputs. These solutions are no longer meaningful when $\omega \to \omega_c = 5 - 10$ MHz, at which point cyclotron effects are dominant.

As inputs, Stellgap takes a processed VMEC equilibrium and additional files specifying the ion mass, density profile and a range of Fourier modes to examine. As described previously, this processed equilibrium is first transformed to Boozer coordinates with Booz-Xform, then broken into matrix elements describing field

Figure 3.2: STELLGAP output before and after the Jacobian was adjusted. The reversal surface is the source of discontinuity at $\psi_{\text{norm}} = 0.85$. Image provided by Don Spong.

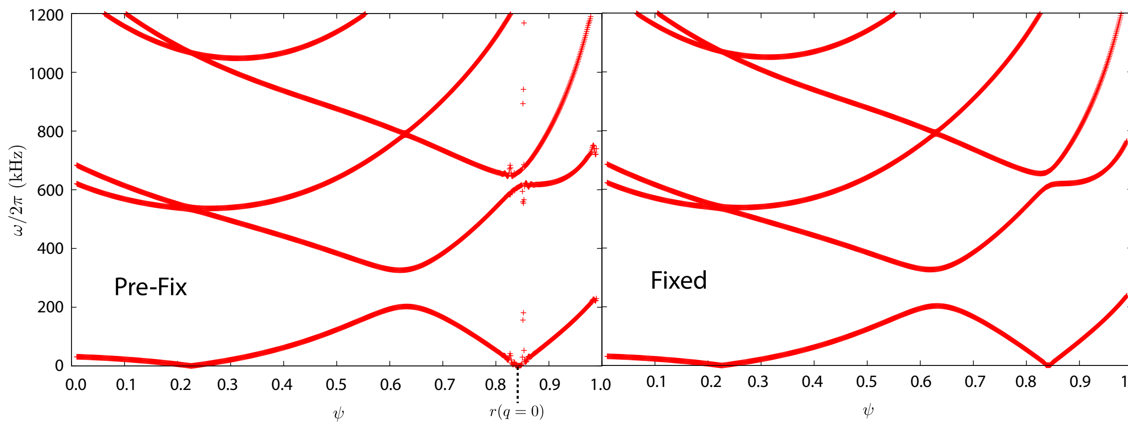

line orientations as a function of flux by XMETRIC. As outputs, STELLGAP returns a list of frequencies, each corresponding to a flux surface, n number, and dominant m number.

This code has been applied to stellarators, tokamaks and, more recently, RFPs, [49, 18]. Note that with the appropriate adaptation of VMEC, STELLGAP handles the reversal surface well, Fig. 3.2. Its solutions provide a map of the continuum, which helps to locate Alfvén eigenmodes in radial and frequency space. The code required no adaptation to run on 3D equilibria, as its calculations are done in flux coordinates.

AE3D

In order to capture the physics of Alfvén eigenmodes in the pressureless, reduced-MHD limit, a different approach must be taken to account for their radial extent. The formulation used to build STELLGAP identifies eigenvalues on radial surfaces, which makes it insufficient for locating global modes. The reduced-MHD formulation presented by Kruger, Hegna and Callen [52] excludes short wavelength modes and distinguishes between equilibrium and perturbation scale effects. The modified vorticity equation and Ohm's law equation are employed in the pressureless, compressionless limit to obtain

$$\omega^2\nabla\cdot\left(\frac{1}{v_A^2}\nabla\phi\right)+(\mathbf{B}\cdot\nabla)\left[\frac{1}{B}\nabla^2\left(\frac{\mathbf{B}}{B}\cdot\nabla\phi\right)\right]+\nabla\zeta\times\nabla\left(\frac{\mathbf{B}}{B}\cdot\nabla\phi\right)\cdot\nabla\frac{J_{\|0}}{B}=0 \tag{3.3}$$

where ϕ is the electrostatic potential and $J_{\|0}$ is the equilibrium parallel current. Recognizing that $v_A^2 = B^2/\mu_0\rho_m$, this equation is of a similar form to Eq. 3.2 with the additional third term of higher order. Multiplying by a trial function $\tilde{\phi}$ and integrating by parts, the equation becomes

$$\begin{aligned}-\omega^2\int d^3x\frac{1}{v_A^2}\nabla\tilde{\phi}\cdot\nabla\phi+\int d^3x\left[\nabla\left(\frac{\mathbf{B}\cdot\nabla\tilde{\phi}}{B}\right)\cdot\nabla\left(\frac{\mathbf{B}\cdot\nabla\phi}{B}\right)\right]&\\+\int d^3x\left(\frac{\mathbf{B}\cdot\nabla\phi}{B}\right)\nabla\zeta\cdot\nabla\tilde{\phi}\times\nabla\left(\frac{J_{\|0}}{B}\right)=0.&\end{aligned} \tag{3.4}$$

A similar approach to the solution of Eq. 3.2 is taken, with Fourier expansions in ϕ and $\tilde{\phi}$. In this case, finite radial elements $f_p(\rho), f_q(\rho)$ are included in the basis functions to permit solutions with radial extent. The basis functions are

$$\phi=\sum_{i=1}^{I}\sum_{p=1}^{P}\phi_{ip}f_p(\rho)\cos(m_i\theta-n_i\zeta);$$

$$\tilde{\phi}=f_q(\rho)\cos(m_i\theta-n_i\zeta),$$

where i is the Fourier mode index, p is the flux surface index, and ρ is the flux surface label. Once more, the problem is cast as a matrix equation,

$$\omega^2\overleftrightarrow{G}\mathbf{y}=\overleftrightarrow{F}\mathbf{y}$$

where $\mathbf{y}$ is a vector containing the ϕ_{ip} terms, with two loops over i and p within the one-dimensional vector. The resultant matrix is large, and more easily solved when a frequency band is selected beforehand. For this reason, it is useful to run Stellgap beforehand to identify gaps within which eigenmodes might reside. Both solutions for eigenmodes and continuum resonances can be found using this method, although it is a significantly slower tool than STELLGAP for that purpose. Because a finite radial element is used, the global eigenfunction is determined by solution for the ω^2 values. Multiple Fourier harmonics may couple along a wide radial extent, providing the expected form of the eigenfunctions for TAEs and other Alfvén eigenmodes.

AE3D uses the same input file from XMETRIC that STELLGAP uses. The code returns eigenfunctions of the electrostatic potential ϕ and their associated eigenfrequencies. Although both continuum modes and Alfvén eigenmodes are found, they are easily distinguishable by their eigenfunctions (It should be noted that although continuum modes are eigenmodes of the matrix equation, the moniker of Alfvén eigenmode is reserved for special cases with radial extent due to coupling.). Continuum modes have sharp singularities in their forms, Fig. 3.3, which bely either short wavelength couplings or phase mixing, two phenomena whose scale lengths are too short to be captured by the reduced MHD formulation. The resonant surfaces at $\psi(\omega_{\rm res})$ are marked, along with the adjacent non-resonant surfaces with $\omega \neq \omega_{\rm res}$. The adjacent non-resonant surfaces cause phase-mixing, and for this reason the continuum functions are ignored. The AEs have a broader radial extent and either no singularities or singularities far from the bulk of their eigenfunction, Fig. 3.4. They are significantly smoother than their continuum counterparts. The resonant and non-resonant surfaces are indicated once more, but it is clear from the picture that the radial extent of the mode creates a wide area of resonance where growth can occur. An eigenmode that crosses the continuum was chosen to show that although it is next to non-resonant surfaces, it has a broader eigenfunction, rendering it more resistant to local dispersion. The code has no built-in selection criterion for identifying AEs, but they can be readily identified by browsing the output eigenfunctions.

Figure 3.3: Example Alfvén continuum mode structure as output by AE3D. The solid lines represent poloidal spectral components of the solution. Surfaces where $\omega = \omega_{\text{res}}$ is the dominant resonance are plotted in dotted red, while surfaces where $\omega \neq \omega_{\text{res}}$ are dominant are plotted in dotted blue to illustrate phase mixing at nearby non-resonant surfaces.

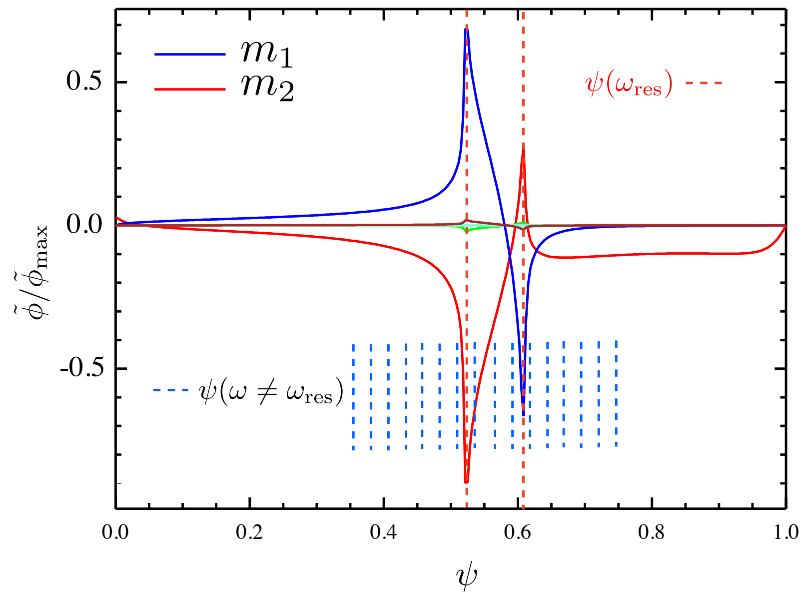

The eigenfunction solution code AE3D has also previously been applied to stellarators and tokamaks [50]. Without adaptation to function with the poloidal flux version of VMEC, the reversal surface presents a significant problem for RFPs. The frequency distortion present in STELLGAP manifests as a "hole" in the resonant eigenfunction. Because AE3D connects radial steps to enforce continuity, this hole kinks or zeroes the eigenfunction at the reversal surface. [At the time of writing, this issue has not yet been resolved. Several eigenfunctions will be presented in Sec. IV, whose recalculation is straightforward once modifications in the code have been made.]

3.3 3D Equilibrium Reconstruction

The adaptation of VMEC to work with RFPs was motivated primarily by the presence of a helical axis in RFX plasmas [48, 53]. The same phenomenon occurs for MST

Figure 3.4: Example TAE structure as output by AE3D. The solid lines represent poloidal spectral components of the solution. The domain where $\omega = \omega_{\text{res}}$ is the dominant resonance is indicated in dotted red while the surfaces where $\omega \neq \omega_{\text{res}}$ are dominant are shown in dotted blue. The mode has a nonsingular eigenfunction across a significant portion of the plasma.

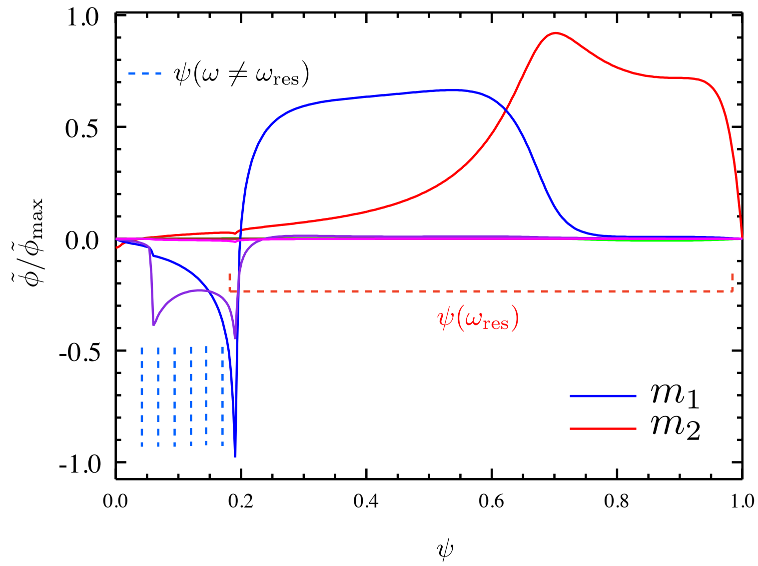

plasmas, which transition to a helical equilibrium in high I_p non-reversed discharges. The shift is characterized by a large increase in the amplitude of the coremost mode, from $\tilde{B}_{\text{w}}/B_{\text{w}} = 1\% \rightarrow 8\%$. Simultaneously, the secondary modes decrease in amplitude, decreasing stochasticity and leading to a new equilibrium with a single helical axis (SHAx). The condition for single felicity expressed in terms of the spectral index,

$$N_s = \left[\sum_{n=5}^{15} \left(\frac{\left(\tilde{b}_n\right)^2}{\sum_{n=5}^{15} \left(\tilde{b}_n\right)^2} \right)^2 \right]^{-1} \tag{3.5}$$

where the growth of any single mode and decrease of other modes will cause $N_s \rightarrow 1$. On MST, the $n = 5$ mode grows and the spectral index decreases to $N_s \approx 1.1$ as the other mode amplitudes decrease.

The modifications to VMEC for RFPs allowed V3FIT, an equilibrium reconstruction code built to run with the equilibrium solver VMEC, to work with the RFP. The

Figure 3.5: SXR emissivity compared to NCT-SHEq equilibrium. (a), the NCT-SHEq flux surface solutions calculated from external magnetics. (b)(d) The SXR emissivity mapped to NCT-SHEq flux surfaces. (c) The reconstructed SXR emissivity map from only SXR measurements. (e) The compared reconstruction from (b) with the measured data. From [54].

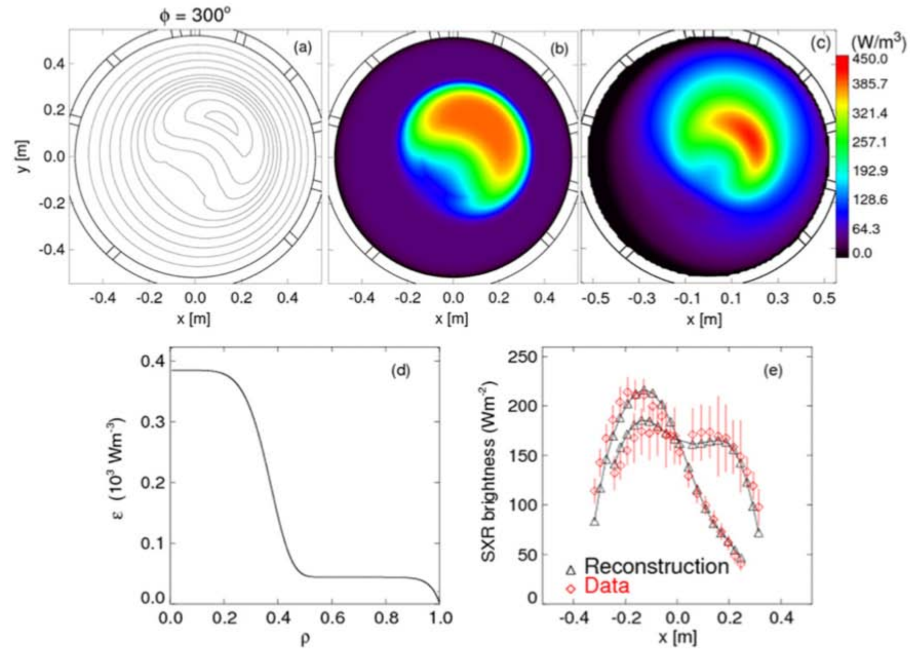

expanded access to analysis routines built on VMEC was a happy secondary effect of this adaptation. While the main focus of this thesis is on Alfvénic activity and thus on the AE3D and Stellgap, a significant push has also been made to reconstruct helical plasmas on MST using V3FIT. Because the output of a V3FIT reconstruction is a VMEC equilibrium, these analysis routines can be applied immediately after reconstruction. However, the first reconstruction of MST plasma equilibria using internal diagnostics along with magnetics is itself an important result.

3.3.1 Newcomb Toroidal Code

Reconstruction of helical flux surfaces has been performed previously using the Newcomb Toroidal Code (NCT) for comparison with the Soft X-Ray system [54], Fig.

Figure 3.6: $\bar{n}_e$ from FIR Interferometry compared to NCT-SHEq equilibrium. (a), the NCT-SHEq flux surface solutions calculated from external magnetics. (b) n_e surfaces from mapping measurements to flux surface solutions. From [55].

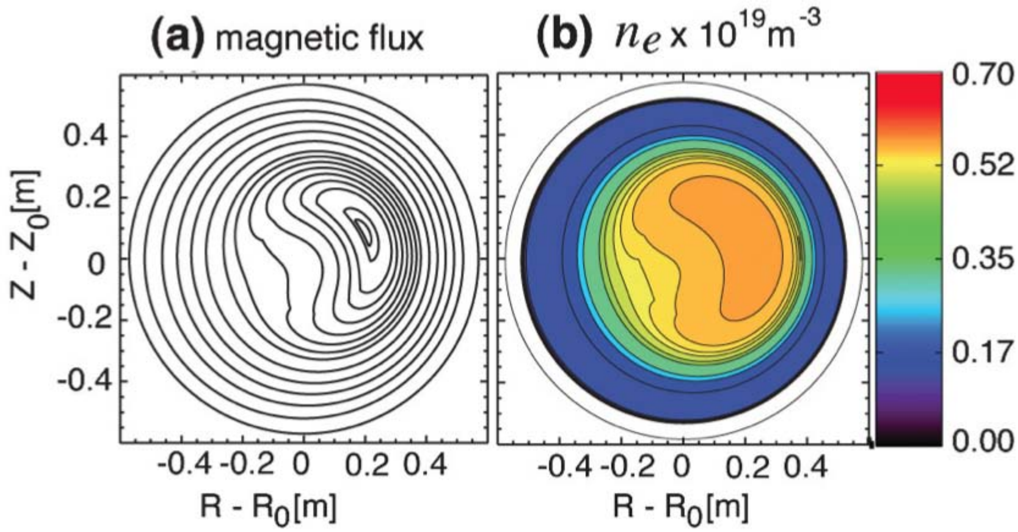

3.5, and the Interferometer-Polarimeter [55], Fig. 3.6. NCT performs a spectral decomposition to form flux coordinates, as VMEC does. However, the code takes a pressureless, perturbative approach to calculating the flux surfaces. First the zeroth order approximation, non-concentric circular flux surfaces with a Shafranov shift, is calculated. This solution closely matches the equilibrium in an axisymmetric plasma. Then the first order correction, the dominant helical mode eigenfunction, is calculated. These two solutions are linearly combined to match the edge magnetic measurements [56].

Although the solution approximates the helical flux surfaces well, it is not a fully three dimensional calculation. Secondary harmonic content in the calculation of flux surfaces plays a role in defining their shapes, and is not included in the NCT calculation. Pressure is also not included in the calculation, which for the axisymmetric case is a good approximation. This approximation may not hold true at all points for 3D equilibria, although the region of strong pressure gradient seen on RFX is observed to have little effect on NCT reconstructions[57]. Because pressure is not included, and neither are internal diagnostics, density is not constrained in the calculation by interferometry. Polarimetry relies on the $n_e(r)$ inversion from interferometry to decouple its $\overline{n_e B_z}$ measurement. Without a self-consistent constraint on density, achieving a match between diagnostic results and modeled signals can be deceptive. For these reasons, a fully three dimensional equilibrium reconstruction code like V3FIT is preferred as the ultimate direction of equilibrium reconstruction on the RFP.

3.3.2 V3FIT

The three-dimensional equilibrium reconstruction routine V3FIT is a modular code that performs χ^2 minimization between computed and measured signals. Although V3FIT is designed to interface with any equilibrium solver, VMEC maintains dominance in the realm of 3D equilibrium solvers, and is to-date the only one implemented. V3FIT has been used to reconstruct 3D stellarator and tokamak equilibria in the past [44]. The adaptation of VMEC to function with the RFP consequently permitted V3FIT to be run with the RFP, and reconstructions have been performed for the RFX-mod device [58]. Recently, V3FIT has been benchmarked against NCT for axisymmetric RFP equilibria on RFX-mod[59].

Minimization algorithm

The code seeks to minimize the total weighted difference between observed signals and computed signals. The description presented here follows the method presented in Hanson's 2009 paper [44]. First, a VMEC equilibrium is generated from initial inputs according to the method described in Section 3.2. The set of parameters $\mathbf{p}$ included in the VMEC and V3FIT input files are inputs that are allowed to vary throughout the reconstruction. The set of diagnostic values $\mathbf{d}$ are measurements whose values are fixed throughout the reconstruction. The computed signals, or model signals, $S_i^m(\mathbf{p})$ are generated from the equilibrium. The observed signals, $S_i^o(\mathbf{d},\mathbf{p})$ include the diagnostic values in the simplest case, but can also include values calculated from a combination of diagnostics, which can be used for averaging or taking the largest value of a set. Associated with the observed signals is a measurement error σ_i in the same units as S_i. A weighting for each signal κ_i may also be specified. A similar function to χ^2 is computed,

$$g^2(\mathbf{p}) \equiv \sum_i \kappa_i \left(\frac{S_i^o(\mathbf{d},\mathbf{p}) - S_i^m(\mathbf{p})}{\sigma_i} \right)^2 , \tag{3.6}$$

This is the function that V3FIT seeks to minimize, and is distinguished from χ^2 in the presence of a weighting value κ_i and the use of signals S_i^o, which may be a function of the parameters as well as the diagnostics. $g^2 \sim \sum_i \kappa_i$ is approximately the condition for a good fit, corresponding to the state where the mean (weighted) value of $|S_i^o - S_i^m|$ is equal to the measurement error. An error vector normalized to σ_i has components defined as

$$e_i \equiv \frac{\sqrt{\kappa_i}}{\sigma_i} \left(S_i^o(\mathbf{d},\mathbf{p}) - S_i^m(\mathbf{p}) \right). \tag{3.7}$$

The error vector is used to construct a Jacobian in conjunction with a dimensionless parameter vector $a_j = p_j/\pi_j$, where π_j is a normalizing factor. This Jacobian,

$$A_{ij} = -\frac{\partial e_i}{\partial a_j} \tag{3.8}$$

describes how a small change to model parameters will affect the computed signal S_i^m. Singular value decomposition is performed on A_{ij}. Quasi-Newton steps are used to avoid computing the Hessian matrix. The step towards minimizing g^2, $\underline{\delta a}$ is found through the equation

$$\mathbf{A}^T \cdot \mathbf{A} \cdot \underline{\delta a} = \mathbf{A}^T \cdot \mathbf{e}. \tag{3.9}$$

Taking the step $\mathbf{A} \cdot \underline{\delta a}$ leads to a decrease in the error vector. The expected new error vector

$$\tilde{\mathbf{e}} = \mathbf{e} - \mathbf{A} \cdot \underline{\delta a} \tag{3.10}$$

contributes to an expected new value,

$$\tilde{g}^2 = \tilde{\mathbf{e}} \cdot \tilde{\mathbf{e}}. \tag{3.11}$$

At this point the VMEC solver is run again, and the new g^2 value is calculated in the same fashion. This process is repeated until user-defined criteria such as maximum number of iterations, minimum Δg^2, or minimum g^2 are met. The final equilibrium solved by VMEC is returned as the result of the reconstruction.

Parameters

V3FIT alters the equilibrium through modifying the input parameters to the VMEC reconstruction. VMEC accepts pressure as an input to determine the ∇p term in the equilibrium, but does not separate out T and n from $p = nk_BT$. Additional profiles for flux functions such as density and brightness are included in the V3FIT inputs, but must be implemented with care as they are determined independently of the VMEC reconstruction. These profiles are altered in the V3FIT minimization step after a VMEC reconstruction, subject to the constraint imposed by pressure and the flux surface shapes. They do not have direct input into the VMEC solution.

Each parameter is associated either with a static number or a multivariable profile. Each point in a profile, in addition to any single value inputs, may be specified as a parameter to be varied. Along with identification, a step size in the units of the associated parameter must be specified. Table 3.1 contains a list of the parameters that may be varied during V3FIT reconstruction, and the following paragraphs explain any parameter meanings that may be unclear. Finally, a description of the available parameterization functions for use in both VMEC and V3FIT follows.

Table 3.1: V3FIT and VMEC parameters

Parameter	Variable	Name	Flux Label	Code	Type
Pressure	p	‘AM_AUX_F’	‘AM_AUX_S’	VMEC	Profile
Pressure Norm.		‘PRES_SCALE’		VMEC	Value
Safety Factor	q	‘AI_AUX_F’	‘AI_AUX_S’	VMEC	Profile
Toroidal Flux	Φ_{B_t}	‘PHIEDGE’		VMEC	Value
Electron Density	n_e	‘PP_NE_AF’	‘PP_NE_AS’	V3FIT	Profile
Electron Temperature	T_e	‘PP_TE_AF’	‘PP_TE_AS’	V3FIT	Profile
Soft X-Ray Emissivity	ϵ	‘PP_SXREM_AF’	‘PP_SXREM_AS’	V3FIT	Profile
Axis R Fourier Comp.	R_0	‘RAXIS’		VMEC	Profile
Axis Z Fourier Comp.	Z_0	‘ZAXIS’		VMEC	Profile
Bndry R Fourier Comp.	$R_a(m,n)$	‘RBC$(m,\ n)$’		VMEC	2D Profile
Bndry Z Fourier Comp.	$Z_a(m,n)$	‘ZBS$(m,\ n)$’		VMEC	2D Profile

The first several inputs to consider when reconstructing a plasma are terms directly relevant to radial force balance, $\mathbf{J} \times \mathbf{B} = \nabla p$. The variable ‘AM_AUX_F’ parameterizes the pressure profile and accepts a vector of variables as input. The associate flux label for each point in a spline fit is ‘AM_AUX_S’. These may also be varied as parameters in the model. The associated variable ‘PRES_SCALE’ is a normalization factor intended to be used to convert between units of pressure. It directly multiplies each term of the pressure profile. The variable ‘AI_AUX_F’, when VMEC is running in poloidal flux, parameterizes the q profile. Its associated flux label is ‘AI_AUX_S’. Finally, ‘PHIEDGE’ is the total toroidal flux through a toroidal cross section.

V3FIT contains a number of inputs that parameterize flux functions, but do not directly affect the VMEC equilibria. The coefficients in ‘PP_NE_AF’ describe the electron density of the plasma if a spline fit is chosen, with appropriate flux labels ‘PP_NE_AS’. Similarly, ‘PP_TE_AF’ and ‘PP_TE_AS’ correspond to the electron temperature, and ‘PP_SXREM_AF’ and ‘PP_SXREM_AS’ correspond to soft X-ray emissivity. All three profiles may have their primary inputs as ‘_B’ instead of ‘_AF’ as part of a two-power fit instead of a spline, resulting in no need for the '_AS' flux labels.

The three profiles can be coupled or decoupled in V3FIT, depending on the options chosen. By using $p = nk_BT$, the model only requires pressure and density to be parameterized to fit all three variables. Through the specifier 'MODEL_TE_TYPE', the user can specify whether a T_e profile is input and varied, or whether only a density profile is input and temperature is calculated from $p = nk_BT$. Soft X-ray emissivity can be calculated from the simple model $\epsilon = p^{1/2}\left(n_e/n_{e0}\right)^{3/2}$, once again relying only on the density and pressure. However, implementation of this model in practice is quite difficult due to filtering techniques present on most soft X-ray camera systems. An independent emissivity profile assumed to be a flux function is still useful as an identifier of flux surface shape and phase. The two options are selected between with the specifier 'MODEL_SXREM_TYPE'. Finally, the ion pressure p_i contributes along with the electron pressure, so a scalar relation between the two is assumed in the model, and the ratio of electron pressure to the total pressure can be specified with 'E_PRESSURE_FRACTION'.

The flux surface geometry can also be taken as a parameter. Specification of the last closed flux surface (LCFS) in helical plasmas informs VMEC of where it should stop calculating its solution. The 'RBC(m, n)' and 'ZBS(m, n)' input parameters specify the Fourier components of the LCFS, where m and n are the poloidal and toroidal mode numbers in VMEC coordinates, respectively. When running V3FIT, the exact shape of the LCFS may not be known at the outset, so allowing these parameters to vary permits deformation at each subsequent VMEC calculation. The variables 'RAXIS' and 'ZAXIS' are initial guesses for the Fourier components of the magnetic axis. Because a line is being described and not a surface, the two parameters are only 1D. VMEC takes the 'axis' parameters only as guesses, and calculates a different magnetic axis in the course of its solution. However, a poor magnetic axis guess can start the equilibrium sufficiently far away from convergence that no solution can be found.

A number of functions are available for parameterization of profiles in VMEC and V3FIT. These functions are selected between for each variable with 'PP_XX_PTYPE' in V3FIT and 'PXXXX_TYPE' in VMEC. The traditional power series centered at 0,

$$f(s) = \sum_{n=0}^{N} p_n s^n, \tag{3.12}$$

is included as 'POWER_SERIES'. A more explicit fit to the form of many plasma parameters, the two-power fit,

$$f(s) = p_0 \left[p_1 \left(1 - s^{p_2}\right)^{p_3} \right] \theta(s)\theta(1-s) \tag{3.13}$$

has terms with a more direct interpretation, and is specified with 'TWO_POWER'. If instead the user wishes to perform spline fits, with $\mathbf{p}(s)$ corresponding to values of the parameter at discrete flux surfaces, two such fits are available. The 'CUBIC_SPLINE' type fit is the standard piecewise cubic interpolation between data points with a continuous 2nd derivative. The 'AKIMA_SPLINE' type fit has been added more recently, and resolves issues of oscillations around bending points of a curve. However, the Akima spline requires 5 points to be specified in order to generate a fit, so it is not practical for all profiles.

Diagnostics and Signals

The ability of V3FIT to reconstruct equilibria hinges on the diagnostics included in its reconstruction. At present, the diagnostics included in V3FIT are flux loops, Rogowski coils, Interferometry, Polarimetry, Soft X-ray cameras and Thomson scattering, Fig. 3.7. All of these diagnostics have been implemented on MST. Each diagnostic has a file specifying the geometric location of its measurements. In addition, each signal S_i^m generated by a diagnostic, corresponding to one measurement,

Figure 3.7: A single flux surface of the helical plasma core with field lines superimposed, over plotted on a diagram of MST diagnostic locations. The mode locks with random phase, but the diagnostics themselves are fixed.

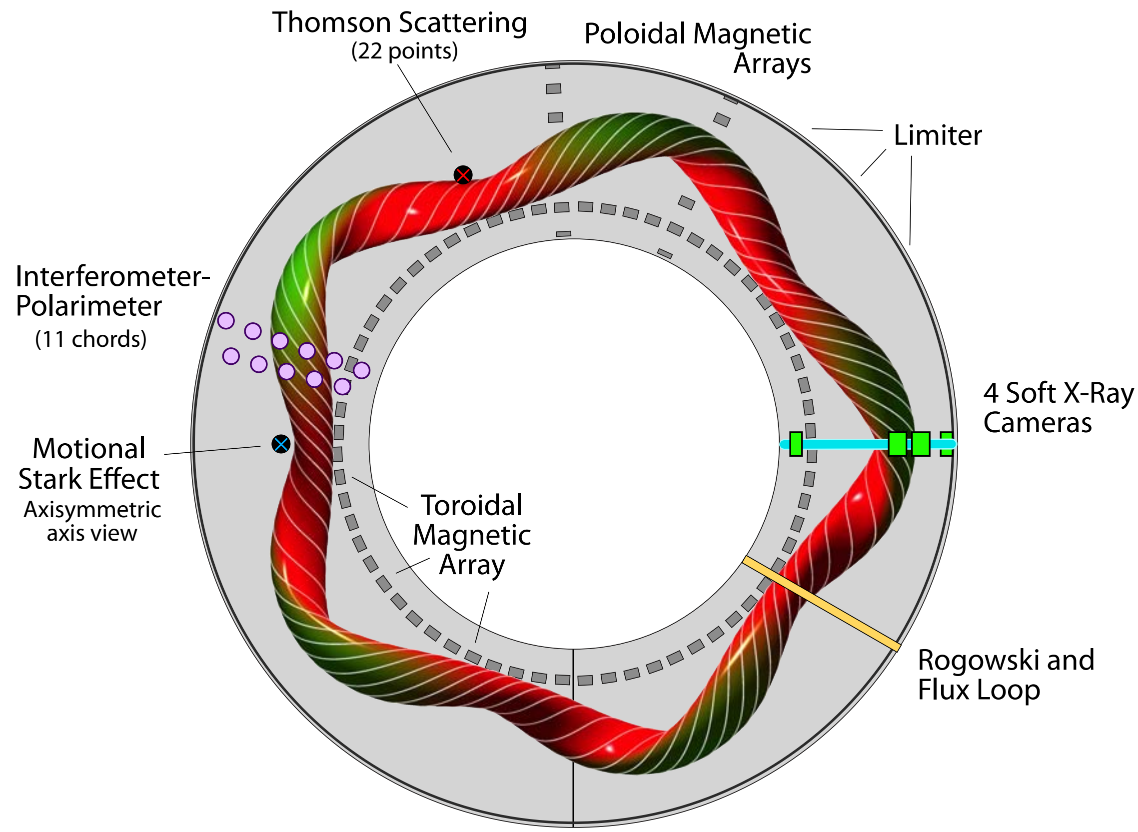

can have a specified σ_i and κ_i. If the user wishes to calculate values for a particular diagnostic but not use it as a constraint, κ_i may be set to 0 for one or all points.

The location of each diagnostic is important, but VMEC contains a peculiarity that must be accounted for in specifying the geometry of the fit. VMEC assumes that the helical axis is outboard at $\phi = 0°$, keeping only the $(R\cos)$ and $(Z\sin)$ terms in its spectral decomposition. In MST, the helical axis locks with random phase with respect to the $\phi = 0°$ location, so a scheme is implemented to account for this, utilizing the toroidal array as a phase designator. The magnetics signals,

Figure 3.8: The mode is rotated so that it is outboard at $\phi = 0°$. The magnetics are not rotated, but all diagnostics are moved along with the mode.

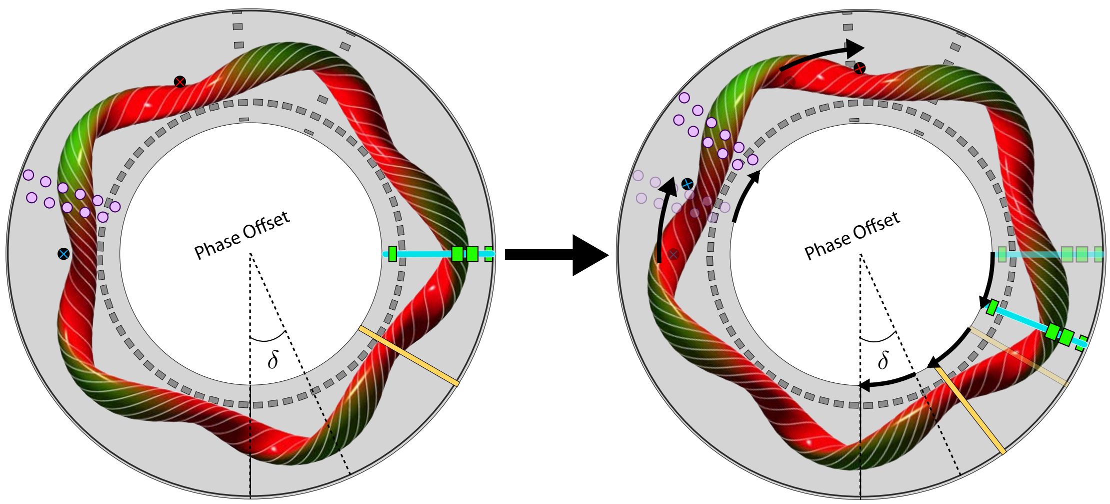

once filtered for the $n = 1$ harmonic introduced by error field at the toroidal gap, are approximated well by $n = 5$ and its higher-order harmonics. To avoid having to shift all ~ 100 coils for each fit, the B_θ and B_ϕ signals are Fourier decomposed and shifted to place the mode outboard at $\phi = 0°$, then recalculated for each coil. In practice, the location of the coils at $\theta = 241°$ requires $\phi(B_{\theta,\max}, \theta = 241°) = 47°$, which corresponds to $\phi(B_{\theta,\max}, \theta = 0°) = 0°$, assuming $n = 5$ periodicity. This technique cannot be performed in the θ direction for diagnostics that are localized in ϕ because toroidicity negates θ symmetry. Processing the data in a spectral fashion would introduce significant uncertainty, so a different approach is taken. All non-magnetic diagnostics have their ϕ locations dynamically determined for each shot, with the rotation angle determined by the processing of the toroidal array data. Effectively, the magnetics rotate the mode around the machine, and the diagnostics rotate toroidally with the mode, Fig. 3.8.

In fixed-boundary mode, V3FIT does not specify currents external to the LCFS.

Figure 3.9: (a)(b) Flux surfaces generated by currents in the plasma. (c)(d) The same flux surfaces after calculation of Green's function response in 72 toroidal current filaments representing the conducting shell. Image by Jay Anderson.

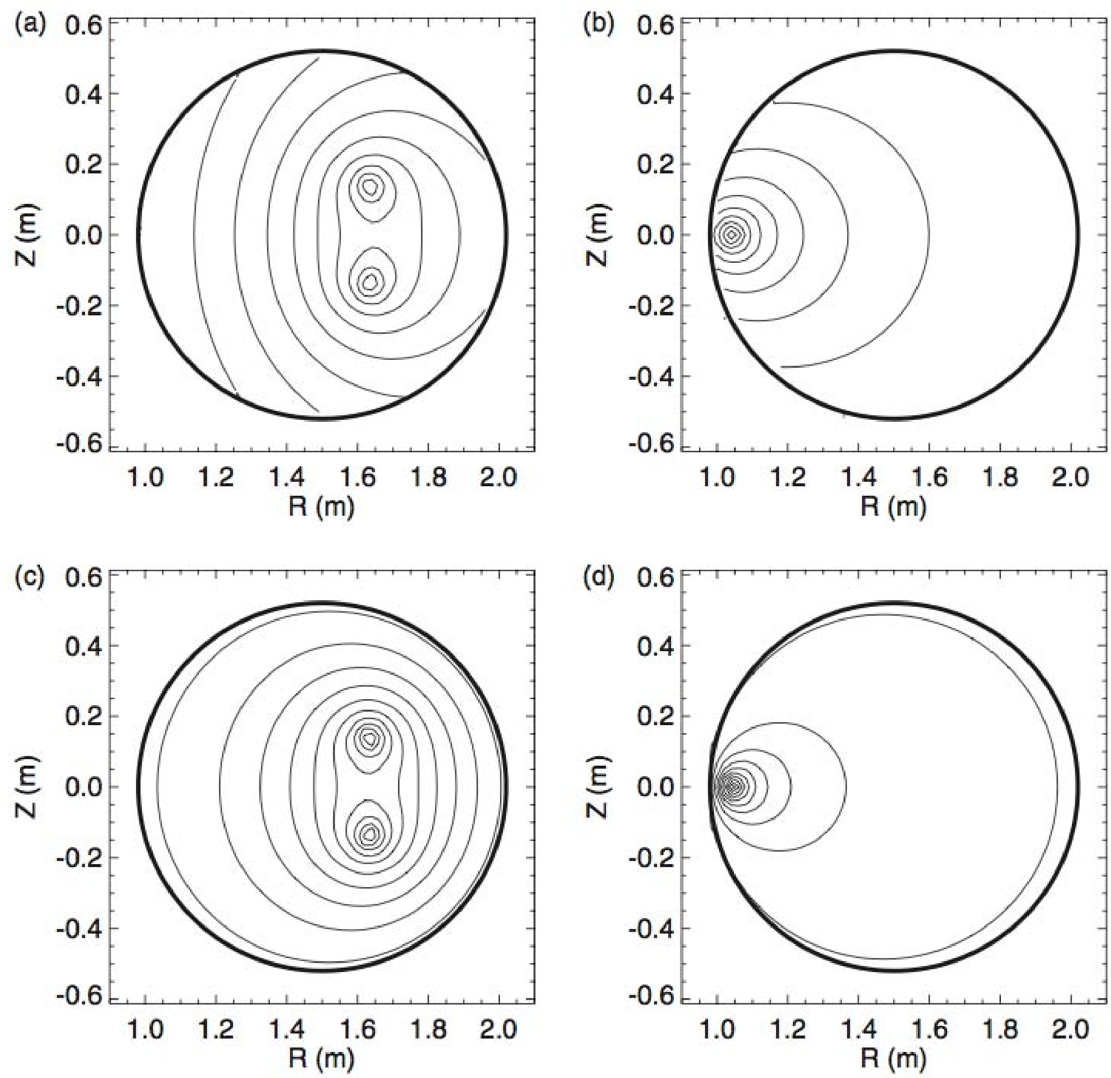

Figure 3.10: ΔB_θ at the toroidal array coil locations vs. I_p. The value for ΔB_θ is calculated from Green's tables applied to MSTFIT equilibria at each of four plasma currents. The fit line represents the first order correction employed in V3FIT.

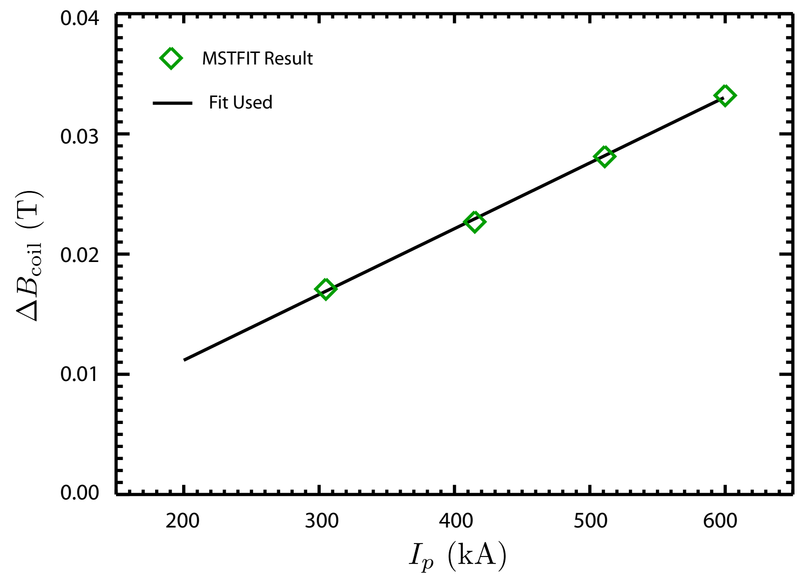

Instead, the LCFS is specified, and the $\mathbf{B}$ and $\mathbf{j}$ are solved for self-consistently inside of this surface. However, the model-calculated $\mathbf{B}$ outside the LCFS includes only the plasma current contribution. This mismatch in observed and modeled signals was initially confusing, so care has been taken to handle it. On MST, a non-uniform $j_{\phi w}$ current distribution in the toroidal shell generates vertical magnetic field B_z to close flux surfaces at the wall, Fig. 3.9. This current arises in the conducting shell from induction due to the magnetic flux of the plasma. The toroidal and poloidal arrays are located outside the LCFS by design. V3FIT does not account for $\Delta B_\theta(a) = \mathbf{B}_z(a) \cdot \hat{\theta}$, so $\Delta B_\theta(a)$ must be calculated and subtracted from the coil measurements before fitting. Tables using Green's functions to determine the $j_{\phi w}$ from $j_{\phi \mathrm{plasma}}(r, \theta)$ have been constructed previously for MSTFIT [24]. These tables were used to determine the first order-correction to the B_θ supplied to V3FIT by calculating the $j_{\phi w}$ and thus B_z at the coil locations in an axisymmetric plasma equilibrium. This process was performed at 4 I_p values with axisymmetric MSTFIT equilibria, then fit linearly to obtain $\Delta B_{\theta,\text{coil}}(I_p)$, Fig. 3.10. This first-order correction is $\Delta B_\theta(a) \sim 10\%\, B_\theta(a)$.

A similar correction is made to the $n = 5, m = 1$ contributions to the coil magnetic field. Empirically, $\Delta B_{n=5}(a) = 60\%\, B_{n=5}(a)$ for both $\tilde{B}_\theta$ and $\tilde{B}_\phi$. Work is underway to incorporate calculation of the helical shell currents into the fit itself.

A crucial signal in the reconstruction is the plasma limiter. While not a 'diagnostic', the location of the limiter provides information about the allowable space the plasma can occupy. Its specification is purely geometric, but it is included as a V3FIT signal whose expected value is 0. When the plasma enters the limiter by deformation of the outer flux surfaces, e_{lim} (Eq. 3.7) rises rapidly, forcing the fit to maintain the LCFS outside the limiter. This signal may also be weighted with κ_i.

3.4 Summary

Axisymmetric plasmas have been reconstructed in the past using the MSTFIT equilibrium reconstruction routine. With the adaptation of the VMEC equilibrium solver to handle RFP equilibria, new access to mature analysis routines has been gained, along with the capability to reconstruct three dimensional plasmas. The NCT perturbative equilibrium reconstruction code has been used to reconstruct plasmas using the assumption of a single helical mode superimposed on an axisymmetric background. The V3FIT 3D equilibrium reconstruction code has been implemented on MST, and full advantage has been taken of its included diagnostics and variable parameters.

Chapter 4

Alfvén Eigenmodes and Continua

The Alfvén continuum provides a map of the frequencies at which energy can be transferred to the plasma without a coherent wave excitation. In the presence of a large population of resonant energetic particles, the Alfvén continuum becomes a map of the frequencies that may be driven unstable for given mode numbers. The Alfvén eigenmodes (AEs) that are located in gaps in the continuous spectrum are weakly damped, allowing them to be driven easily both by waves and energetic particles. For the first time, the determination of the Alfvén continuum and of the eigenmode structures of several Alfvén eigenmodes has been performed for the RFP.

First, the methodology for determining the eigenmodes and continua is outlined. Then this method is applied to three types of axisymmetric equilibria: non-reversed, reversed and deeply reversed plasmas. Finally, the equilibria for helical plasmas are determined and the same method is applied to determine continua and eigenmodes in these cases.

4.1 Methodology

In order to generate the Alfvén continuum, equilibria must be reconstructed. For each case, many shots with similar plasma current I_p, electron density n_e, and edge safety factor q_a were selected. During these shots, the Rogowski loop, flux loop, B_θ coils at the toroidal gap, Interferometry, Polarimetry, Thomson scattering and MSE all collect data to be used in equilibrium reconstruction. MSTFIT offers the capability to use average quantities from many shots to form an ensemble, so a single fit is generated from this set of shots. The goodness-of-fit is assessed from χ^2 and knowledge of the analytical plasma equilibrium quantities.

The MSTFIT-determined pressure profile, q profile, toroidal flux and LCFS geometry are taken from the MSTFIT equilibrium and passed as input parameters to the VMEC equilibrium solver. The solver is run in RFP mode, generating its own equilibrium in VMEC flux coordinates. This is checked against the MSTFIT equilibrium for incongruities that may have developed due to the use of different solvers. In the three dimensional case, V3FIT is run instead of MSTFIT, with the toroidal array B_ϕ coils included and the MSE diagnostic excluded. As the resultant file is a VMEC equilibrium, there is no need to import it into VMEC. In either case, at the end of this step a VMEC equilibrium is produced.

The VMEC equilibrium is processed from flux coordinates into Boozer coordinates by Booz-Xform. The XMetric code then prepares the metric elements for use with the Alfvén codes. Because this equilibrium only contains information on the pressure, the density profile must be imported from either the MSTFIT outputs or the V3FIT profiles. The Alfvén continuum is solved for using Stellgap, with each toroidal mode number n and many possible poloidal mode numbers m solved in one continuum calculation. This step is performed across multiple n's. After gaps or spaces in the continuous spectrum are identified from the STELLGAP output, AE3D is run across each gap frequency range. By browsing the output of the AE3D code, global modes are identified.

4.2 Axisymmetric Continua and Eigenmodes

The Alfvén continua for axisymmetric plasmas are calculated. While more similar to each other than they are to the three dimensional continua, these continua span the majority of RFP operating regimes on MST. Particular attention is paid to non-reversed plasmas, as it is under these plasma conditions that the EPMs are observed.

Figure 4.1: 300 kA $q_a = 0$ Alfvén continuum. The $m = 0$ branch on the right goes to zero frequency at the reversal surface. $m = 0$ couples to $m = 1$ at $q = 1/2n$ for each n shown, forming a gap above 250 kHz.

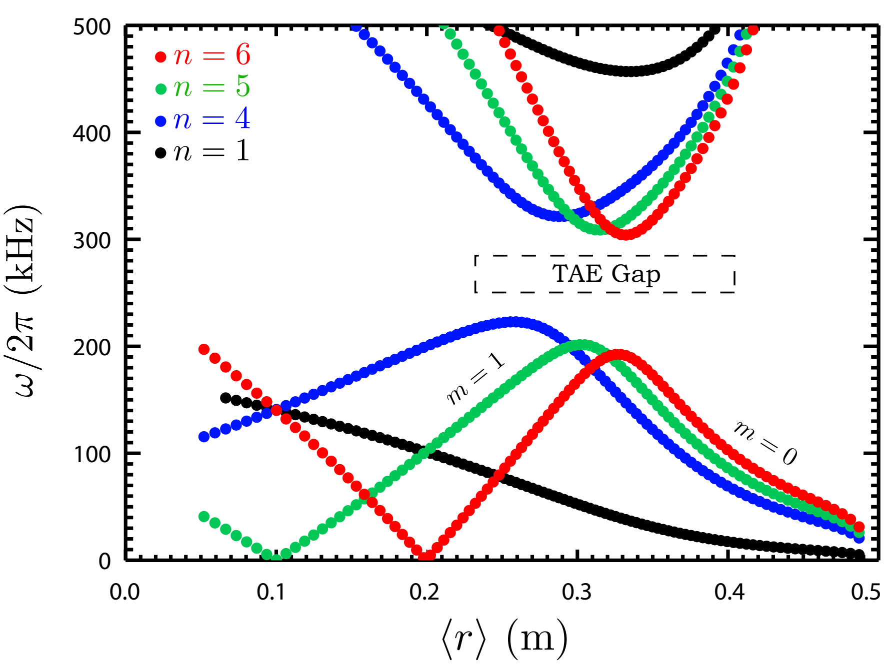

4.2.1 Non-Reversed Plasmas

When the edge safety factor q_a is brought to 0 by short-circuiting the poloidal current in the plasma shell, the decreased activity from $m = 0$ modes in the plasma provides enhanced opportunity to study MHD activity. The sawtooth cycle is modified, with smaller $m = 0$ bursts taking the place of large parallel current relaxation events. Unlike the standard plasma case [32], the q profile evolves minimally throughout this modified cycle, providing a fixed equilibrium. Cases are compared at three densities and three plasma currents around a base case of $I_p = 300$ kA, $\bar{n}_e = 0.7 \times 10^{19}$ m^{-3}, which was chosen because it has been the subject of significant study for EPMs.

Figure 4.2: $q_a = 0$ Alfvén continuum, $n = 5$ at multiple I_p. Solutions are similar, but with frequencies scaled by $v_A \propto |B| \propto I_p$.

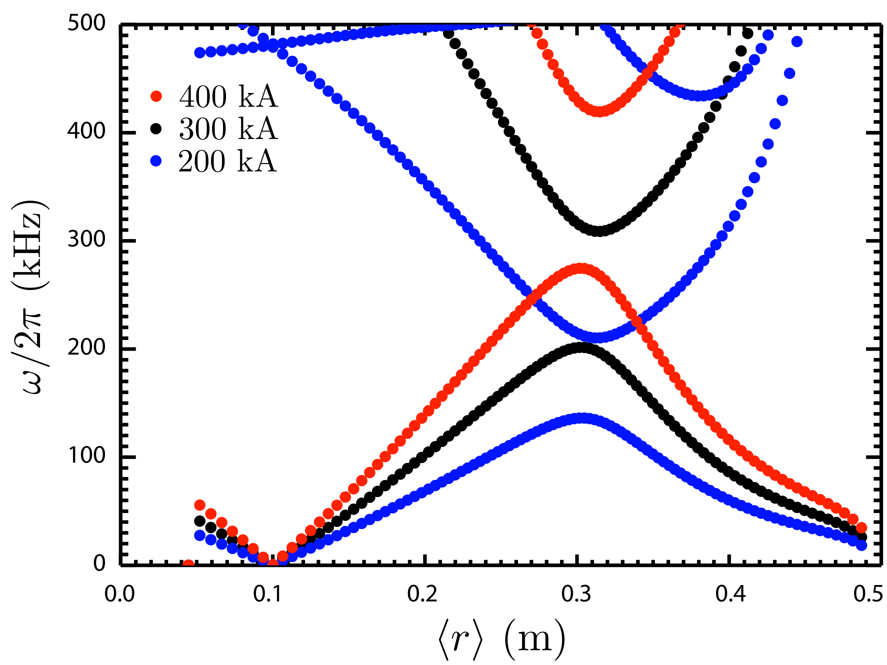

The Alfvén continuum for 300 kA non-reversed plasmas has a number of important features, Fig. 4.1. The outermost branch for all modes is dominantly $m = 0$ due to the location of the reversal surface $q = 0$ at the plasma edge. The zero-frequency point for a given mode lies at $q = m/n$, so all $m = 0$ modes have zero frequency at the reversal surface. The $m = 1$ branch is the second closest to the edge, and couples to the $m = 0$ to create the first gap in the continuous spectrum. All toroidal mode numbers n that have have m-coupling to create a gap have $m = 0, 1$ coupling. With $q < 0.23$, the lowest possible mode number for a gap coupling is $n = 3, m = 0, 1$, Eq. 1.18. Mode numbers for gaps can then be described as medium n, low m. The gap itself is in the frequency range from $f = 200 - 350$ kHz, independent of mode numbers.

Figure 4.3: 300 kA $q_a = 0$ Alfvén continuum, $n = 5$ at multiple $\bar{n}_e$. Solutions are similar, but with frequencies scaled by $v_A \propto 1/sqrt(n_e)$.

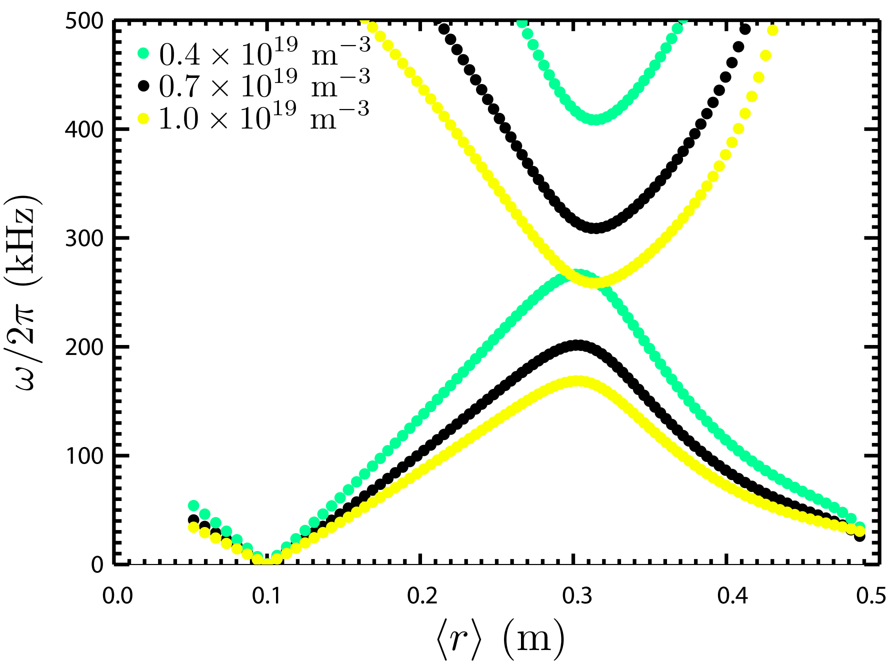

The $I_p = 200$ kA and $I_p = 400$ kA cases have similar features to the 300 kA case, Fig. 4.2. The $\bar{n}_e = 0.4 \times 10^{19}$ m^{-3} and $\bar{n}_e = 1.0 \times 10^{19}$ m^{-3} case also have similar features, Fig. 4.3. The $m = 0, 1$ couplings and m branch locations are unchanged, and a frequency gap is evident. The only discernible difference comes from the Alfvén scaling $v_A = |B|/\sqrt{\mu_0 \rho_m}$, where $\rho_m = m_i n_i \propto n_e$ and $|B| \propto I_p$. The continuum is

Figure 4.4: 300 kA $q_a = 0$ Alfvén continuum, $n = 5$ at multiple q_0. The altered q profile shifts $k_\parallel$, changing resonances and zero crossings.

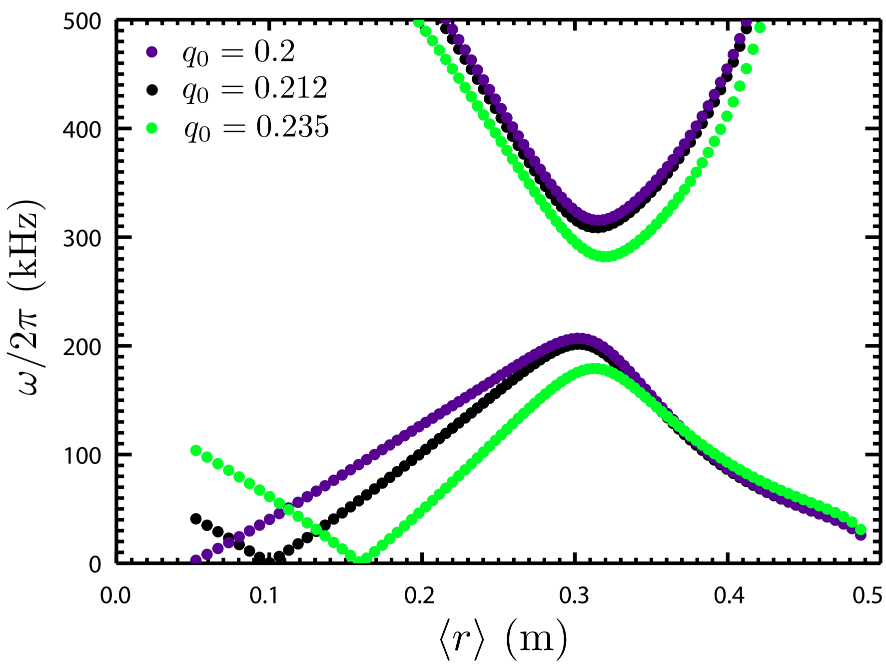

scaled along the frequency axis proportionally to plasma current and inversely with the square root of density, $v_A \propto I_p/\sqrt{n_e}$. The properties along the radial axis change minimally.

A small scan of q_0 was performed, as determination of this parameter has been elusive in the past, Fig. 4.4. The base case with $q_0 = 0.212$ is shown alongside $q_0 = 0.2$ and $q_0 = 0.235$ cases. The radial position of the gap and zero frequency crossings are affected as the q profile alters $k_\parallel$.

The most obvious class of eigenmodes evident from the AE3D solutions are the TAEs, Fig. 4.5. Each solution from $n = 4$ to $n = 8$ is localized to the gap, and has poloidal harmonic content from $m = 0, 1$ coupling. Unlike tokamak continua [5], there are few coupled poloidal harmonics at medium n, with only 1-2 m couplings present. Much like the locations where the gap is created, the peak mode amplitudes move farther outward as n increases. When n becomes large enough ($n = 9$ here), $m = 1, 2$

Figure 4.5: $n = 4$ through $n = 8$ TAE structures in the non-reversed 300 kA base case. The $n = 4 - 7$ TAEs have $m = 0, 1$ coupling, while the $n = 8$ TAE has $m = 0, 1, 2$ coupling. All TAEs extend across the radius of the plasma.

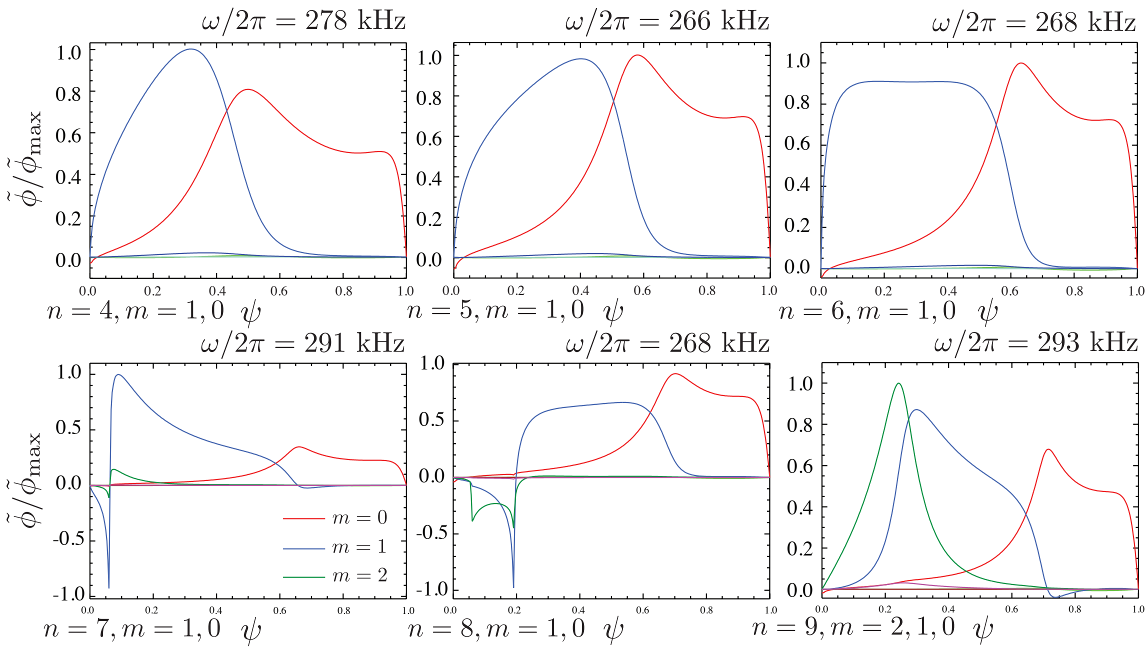

crossings appear and corresponding TAEs are present. The mode frequencies lie in a similar range to the $m = 0, 1$ modes, but the peak mode amplitudes are closer to the core. As is shown in this case, coupling across all three m modes can occur.

4.2.2 Standard Plasmas

The 400 kA standard plasma continuum is similar to the non-reversed 400 kA continuum seen in 4.2, with several notable differences, Fig. 4.6. Although I_p and $\bar{n}_e$ are the same, the modification to the q profile is evident in the shifted mode resonances. Particularly, the $q_a < 0$ condition means the reversal surface $q(r) = 0$ is inside the plasma. This means that the $m = 0$ modes have branches both inside and outside the reversal surface. For high-n modes, there is $m = 0, -1$ coupling outside the reversal surface. Because $q_0 > 0.2$, the zero-frequency point for the $n = 5, m = 1$ mode

Figure 4.6: 400 kA $q_a = -0.06$ Alfvén continuum, with $q_0 = 0.205$. The altered q profile shifts $k_\parallel$ from the non-reversed case, changing resonances and zero crossings. $q_a < 0$ adds an $m = 0$ branch outside the reversal surface.

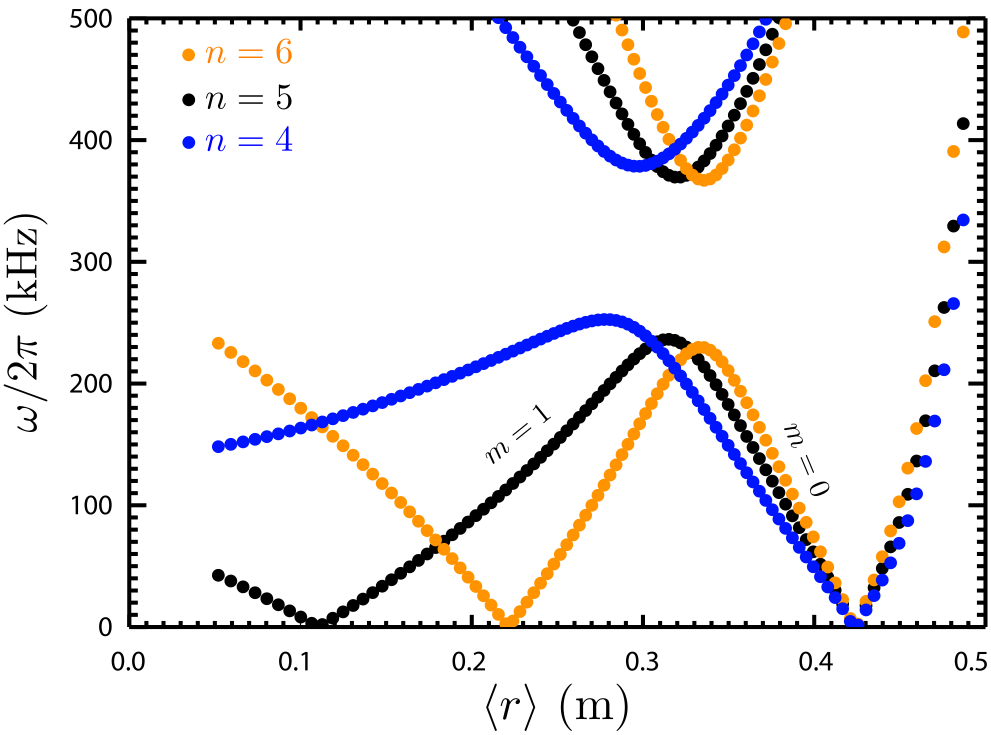

remains. However, the $n = 5$ zero point has shifted 1 cm closer to the magnetic axis due to the slight drop in q, as expected from Fig. 4.4. The continuum gap resides at a similar frequency to the non-reversed case, between 250-400 kHz. Continuum resonances exist outside the reversal surface, where q passes through zero.

For standard plasmas, q_0 varies considerably during the sawtooth cycle, from $q_0 > \frac{1}{5} \rightarrow q_0 = \frac{1}{6}$. However, q_a does not vary considerably. An additional continuum was generated with $q_0 = 0.18$ to examine the shift of the Alfvén continuum that naturally occurs between sawteeth. As shown Fig. 4.7 as compared to Fig. 4.6, a radial shift of the zero-frequency crossings and the gap crossings occurs. The $n = 6, m = 1$ continuum takes on a similar character to the $n = 5$ in the non-reversed case, with a zero-frequency point near the axis. This frequency shift has a substantial

Figure 4.7: 400 kA $q_a = -0.06$ Alfvén continuum, with $q_0 = 0.18$. The altered q profile shifts $k_{\|}$ from the $q_0 = 0.18$ case, changing resonances and zero crossings.

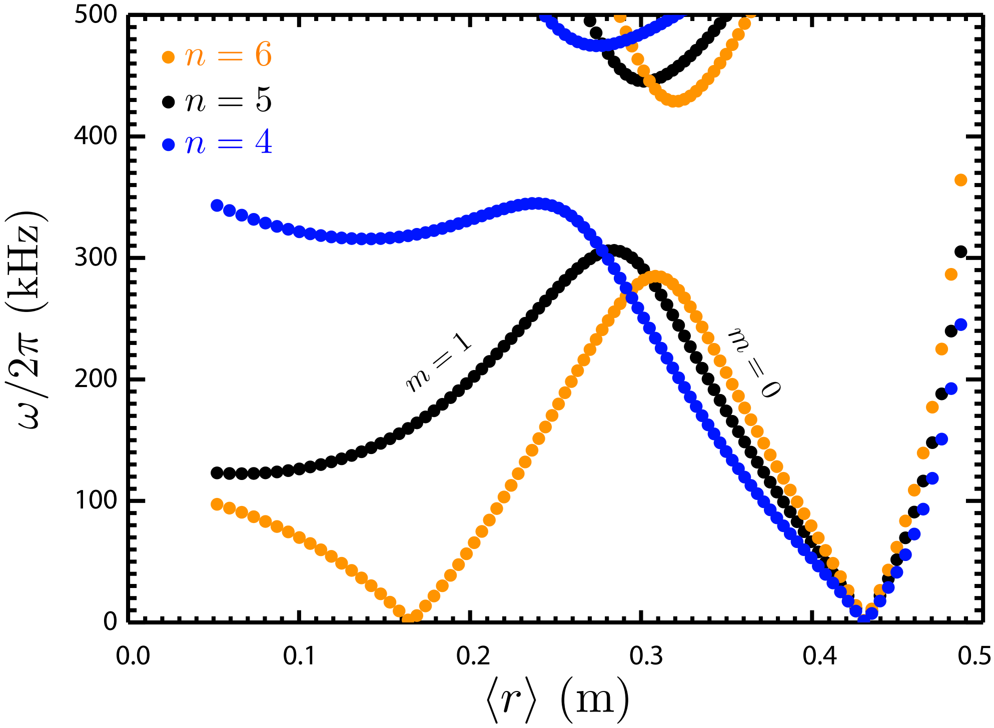

Figure 4.8: $n = 4$ through $n = 6$ TAE structures in the 400 kA $q_a = -0.06$ case. The TAEs are similar to the non-reversed case, although the discontinuity at the reversal surface zeroes their amplitude at the edge.

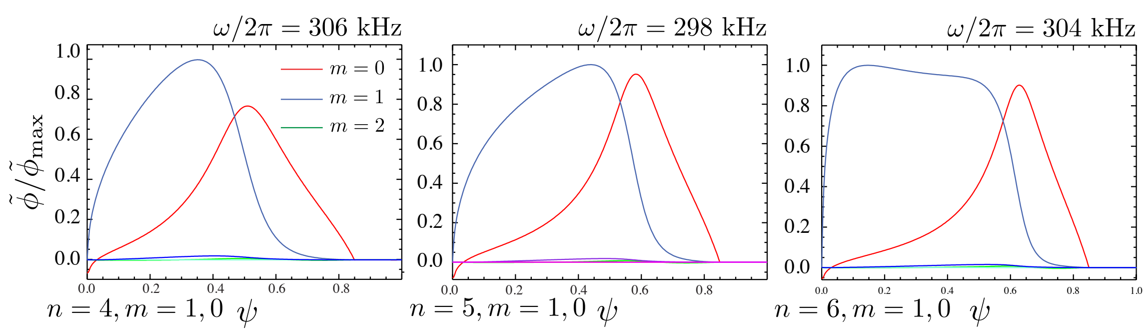

effect on the radial profile of resonance below the TAE gap.

The AEs in these plasma equilibria are similarly sparse in m-content, Fig. 4.8, and only at $n = 8$ and above does the $m = 1, 2$ coupling appear. The kink at the reversal surface is evident at $\psi = 0.85$, where $\tilde{\phi}$ looks like it will change sign, but instead is

Figure 4.9: 300 kA $q_a = -0.15$ Alfvén continuum for deeply reversed plasmas. Further decreased q_0 shifts $k_\parallel$, and $q_a = -0.15$ creates a coupling outside the reversal surface, with a gap above 150 kHz.

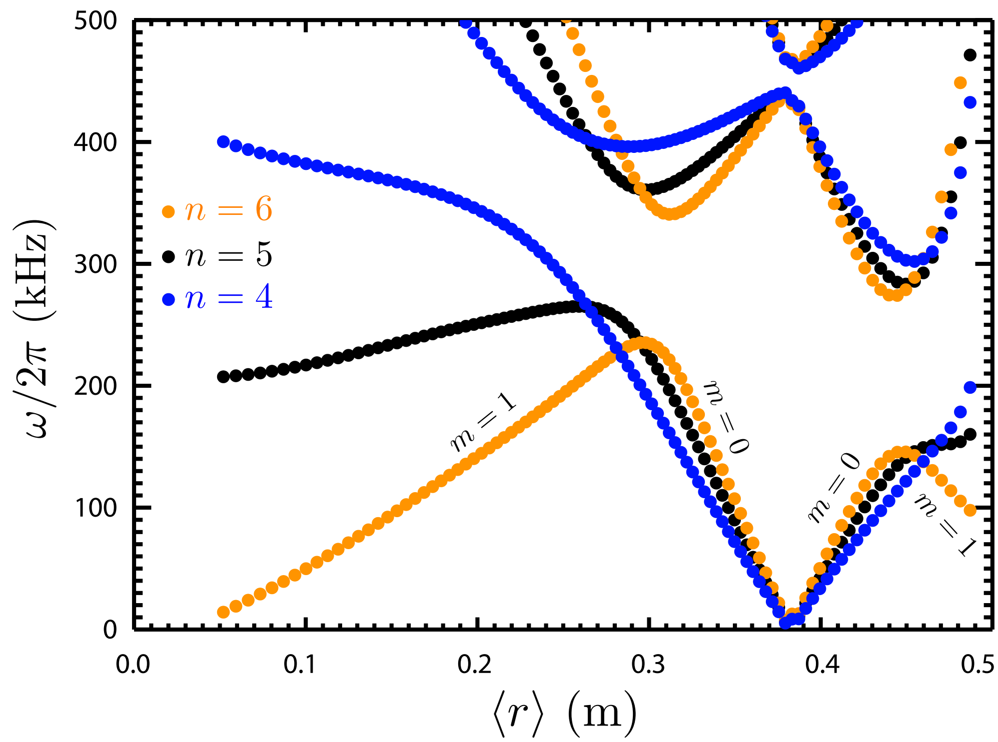

zeroed. In these plasmas, whose reversal surface is closer to the boundary than in deeply-reversed plasmas, the distortion of the eigenmode appears to be minimal.

4.2.3 Deeply Reversed Plasmas

Deeply reversed ($q_a < -0.1$) plasmas are achieved in MST by externally driving $B_{\phi w}$ more negative through a poloidal current in the conducting shell. This process is known as pulsed poloidal current drive (PPCD), and the resulting plasma equilibria are sometimes referred to as "improved confinement" plasmas. They will be referred to as deeply reversed equilibria for the remainder of this work, while the term PPCD will be used in reference to the period within which current is being driven. The most notable changes to the equilibrium for deeply reversed plasmas are a peaking of the

Figure 4.10: q profile during PCCD. The plasma is deeply reversed, with edge safety factor $q_a = -0.15$.

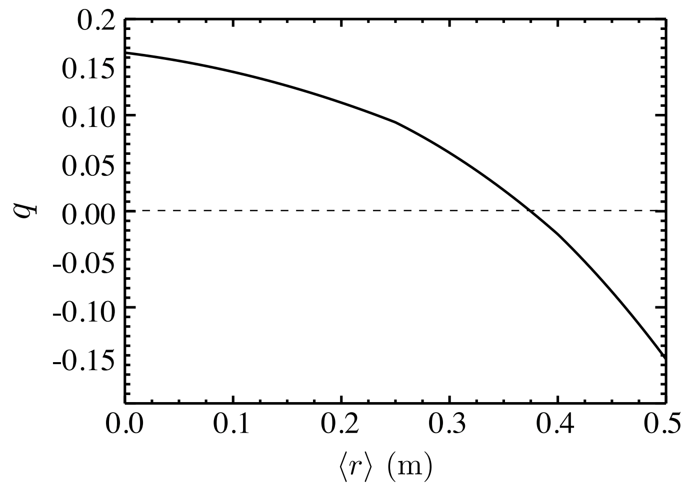

density profile on-axis and a large dip in q_a and q_0, Fig. 4.10. The sawtooth cycle is temporarily halted[60], so although q_a continuously decreases throughout the PPCD period, it is unlikely that q_0 is decreasing as in standard plasmas. As in standard plasma, the $m = 0$ zero-frequency point is inside the plasma, but the reversal surface is farther into the plasma and the q profile is much steeper outside of it, Fig. 4.10. The deeper q_a value allows branches of $m = -1$ to appear at lower n numbers outside of the reversal surface. The gap is in a similar location at 250-400 kHz, although it is at 150-250 kHz outside of the reversal surface.

Alfvén eigenmodes in these plasmas couple on either side of the reversal surface, Fig. 4.11. As evident in Fig. 4.9, a gap exists near $\langle r \rangle = 0.45$, at $\omega/2\pi \approx 200$ kHz. Indeed edge-localized coupled AEs with $m = 0, -1$ and core-localized coupled AEs with $m = 1, 0$ are both found, but due to the current inability of the code to handle the reversal surface, there is no coupling of the two. It is unknown the degree to which the two will couple when the reversal surface is handled adequately by AE3D.

Figure 4.11: $n = 5$ through $n = 6$ TAE structures in the 300 kA deeply reversed case. AE3D does not allow TAE to couple across the reversal surface. Edge-localized TAEs are seen where a gap exists outside the reversal surface.

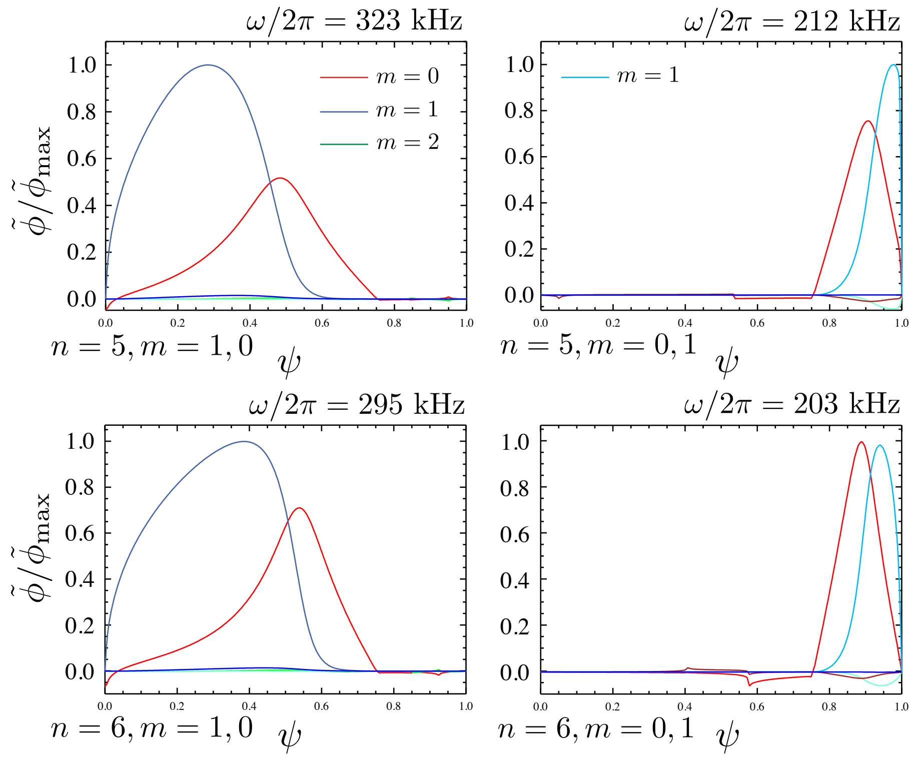

4.2.4 Summary

The Alfvén continua and eigenmodes in axisymmetric RFP plasmas are similar, with differences attributable to v_A and the q profile. The dominant coupling in all plasmas is medium n, $m = 0, 1$, at $q = 1/2n$. The resulting $m = 0, 1$ TAE at $f \approx 250 - 300$ kHz has wide global extent. AE3D is not equipped to handle the reversal surface at present, so modes in $q_a < 0$ plasmas cannot couple across it. A TAE resonant near the edge with $m = 0, 1$ and $f \approx 200$ kHz appears in deeply reversed plasmas, where $q_a \sim -q_0$. In all equilibria, the closest zero point for continuum frequencies lies at $q = 1/n$, where $k_\parallel$ changes sign. The coremost zero frequency points are $n = 5, m = 1$ for $q_0 > 0.2$ and $n = 6, m = 1$ for $q_0 < 0.2$.

4.3 Three Dimensional Continuum and Eigenmodes

Although no high frequency magnetic activity has been detected in SHAx plasmas, the search for such activity is made easier by predictions for eigenmodes and the shape of the Alfvén continuum. For this reason, and owing as well to the fact that VMEC equilibria were used to generate all previously shown continua, three dimensional equilibria have been generated and processed to produce Alfvén continua for the special case of a helical RFP plasma. Because the process of full equilibrium reconstruction in three dimensions is novel for MST, results of successful reconstructions are presented before moving on to Alfvén calculations. A single case is used for the continuum and eigenmode calculations, as the SHAx occurs spontaneously and persists over a narrow range of high I_p, low n_e conditions.

4.3.1 V3FIT Equilibrium Reconstruction Results

The equilibrium reconstructions were performed on the same set of data used for the Bergerson [55] and Auriemma [54] papers from 2011. This set of data was chosen for comparison to the previously published works, and because the full diagnostic set useable in V3FIT was employed during data taking. The legacy thin-filter soft X-ray system with 2 cameras at $\phi = 300°$ is used in this reconstruction as the new system was not installed until late in that year. Interferometry, polarimetry and Thomson scattering were all employed. In addition, the flux loop, the Rogowski coil, and 64 B_ϕ-facing coils and 32 B_θ-facing coils from the toroidal array were included.

The shots examined have $I_p = 500$ kA, $\bar{n}_e \approx 0.5 \times 10^{19}$ m^{-3} and $q_a = 0$. Equilibrium reconstruction is performed on single time slices after SHAx has been established. The observed and modeled number of field periods is $N_{fp} = 5$. Multiple mode

Figure 4.12: Example parameterized profile with a 5-point spline. Varied directions are depicted with red arrows.

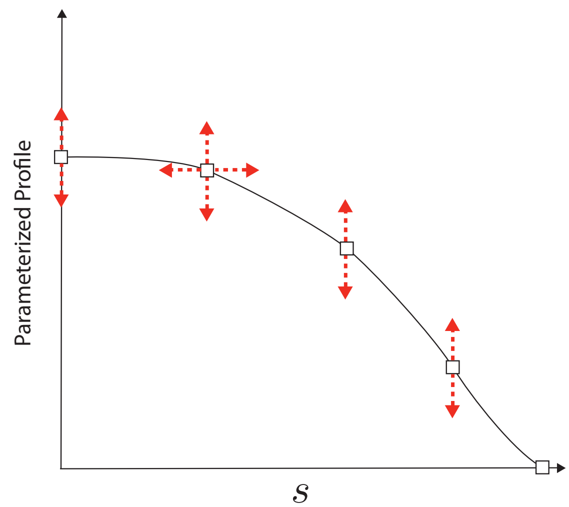

phases with respect to machine coordinates were investigated.

Input Parameters

After all parameters were poorly fit by two-power type parameterizations, all of them were switched to cubic splines. Each spline consists of an on-axis point that can vary in magnitude, a second point that may vary in position and magnitude, two points to determine the shape of the profile towards the edge, and a last to pin the function at the edge, Fig. 4.12. For the q profile, the on-axis and edge point are not allowed to varied, while the three middle points may vary. In other words, q_0 is specified in the VMEC input and remains fixed for the full reconstruction. For all other profiles, only the edge point is not varied. In the VMEC inputs, $p(s)$ and $q(s)$ are specified, while $n_e(s)$ and $\epsilon(s)$ are specified in V3FIT. The electron temperature $T_e(s)$ is not specified, as the option to calculate it on from density and pressure is used.

The q_0 value ($q_0 = 0.155$) is chosen from NCT cases, as it is not currently well-constrained by measurements. V3FIT has ambiguity in the width and shift of the helical surfaces, as the two values may be interchanged to produce nearly identical magnetic signals at the edge. The width and shift are directly determined by the core q values, so the innermost and second innermost points can be modified to produce degenerate results. In this respect NCT may be superior until q_0 measurements can be included in V3FIT, as NCT uses a simple method of linear combination. V3FIT has significantly more freedom to deform flux surfaces due to its full spectral decomposition method, resulting in solutions ranging from $q_0 = 0.1$ to a near-axisymmetric q-profile ($q_0 = 0.2$). The $q(s)$ profiles associated with this range of values have dips and peaks that reproduce the correct magnetic field amplitudes at the edge. With q_0 fixed, varying the remaining points is sufficient to fit the data, and the resultant q profiles are similar across a wide range of shots.

Five values are allowed to vary for the LCFS, Fig. 4.13. The $R_a(0,0)$ value determines the center of the boundary surface. The $R_a(0,1)$ and $Z_a(0,1)$ values determine its radius, tracing a circle in R, Z coordinates. The $R_a(1,0)$ and $Z_a(1,0)$ values determine the helical shift of the LCFS, translating in the same direction as the helical axis. Depending on whether the coordinate system employed is right-handed or left-handed, and on the sign of $I_p \cdot B_\phi$ in this coordinate system, Z_a must be given the correct sign, as V3FIT has difficulty reversing this value as it iterates. For the standard field orientations on MST, $Z < 0$. It should be noted that due to the conducting shell, the helical shifts are small, $Z_a(1,0) \approx 0.5$ mm.

The limiter was specified as a circular boundary at the same distance as the outboard limiter from the wall, $r_L = 0.517$ m. The actual MST limiter consists of two 3 cm bands of graphite tiles covering the full toroidal extent, at poloidal angles $\theta = 0°, 180°$. The full circular limiter in this case was chosen to avoid letting V3FIT "step" the LCFS out of the machine in any direction.

Figure 4.13: Picture of specified VMEC variables describing the last closed flux surface.

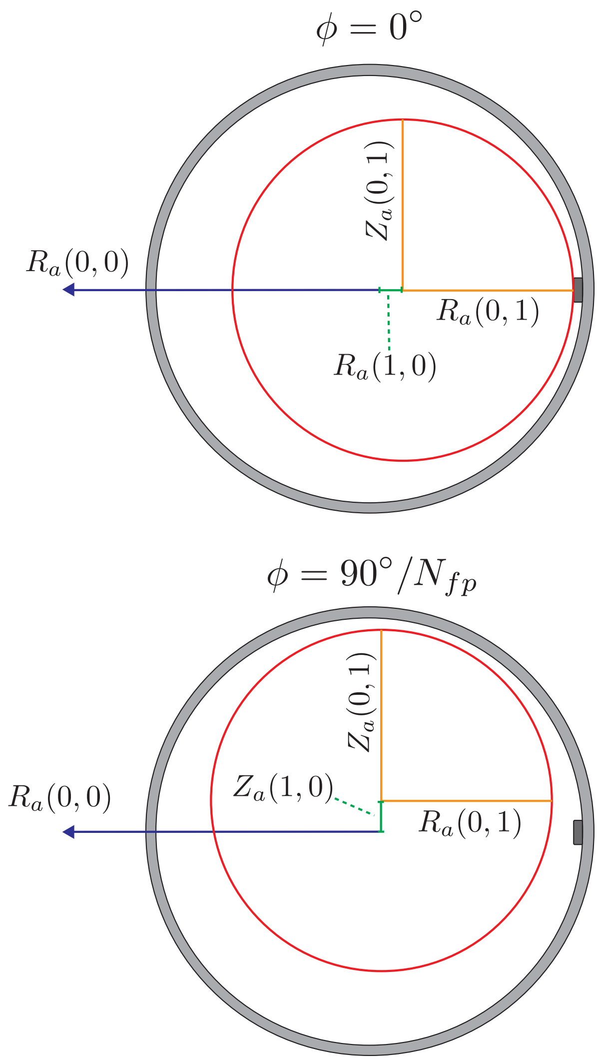

Results

The V3FIT equilibria converged successfully with $g^2 \approx 340$, where $\sum_i \kappa_i = 200$. This corresponds to $\langle S_i^m - S_i^o \rangle \approx 1.3\sigma_i$. The primary factor influencing good convergence were the internal diagnostics, particularly interferometry, polarimetry and soft X-ray. Examination of their error vectors indicates that they were oppositely-oriented, signifying opposed influences on parameters during reconstruction. Polarimetry data pushes the helical distortion to be smaller, while interferometry and soft X-ray push helical surfaces to be larger. Inclusion of all relevant diagnostics in the reconstruction is evidently important, as it allows this competition to contribute to the end degree of confidence. Reliance on individual comparisons of these diagnostics to equilibria reconstructed only from magnetics can be deceptive. The disagreement between diagnostics evidences either poor assumptions of measured quantities as flux functions, or of additional complicating physics.

The reconstructed equilibria have helical shifts of $\Delta R_{1,0} = 17.5$ cm in addition to Shafranov shifts of $\Delta R_{0,0} = 3.2$ cm. The helical surfaces have slight elliptical character, with $|R_a(1,0)| < |Z_a(1,0)|$. This is likely due to the competition between the Shafranov shift and the conducting shell, which causes the perturbation to be more limited in the radial direction, effectively "squashing" it. In the toroidal direction $+\phi$, the helical mode rotates counter-clockwise, in the $+\theta$ direction. On the magnetic axis, $B_\phi = 0.5$ T, and $p = 1100$ mbar. The on-axis safety factor q_0 was fixed, and the reconstruction determined peak safety factor was $q_{\text{peak}} = 0.157$. Two fits of an inboard-locked and outboard-locked mode are compared in terms of p and q, Fig. 4.14, showing good agreement.

Although the safety factor has decreased to $q_0 < 0.2$, eliminating the $n = 5$ resonance, the equilibrium has $N_{fp} = 5$. It is important to note that while the flux surfaces are helically translated with $n = 5$ symmetry, the safety factor is lowered be-

Figure 4.14: Comparison of pressure and safety factor for inboard and outboard locked SHAx cases.

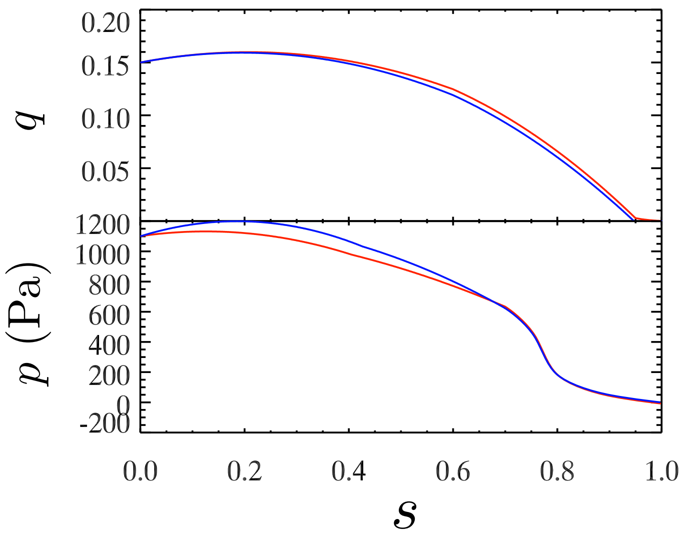

cause helical distortion has introduced writhe that reduces q. As in the axisymmetric case, magnetic field lines complete greater than one poloidal circuit around the $n = 5$ magnetic axis in one toroidal round, implying $q < 0.2$.

The plots from the Auriemma and Bergerson papers that show helical surfaces calculated by NCT are reproduced with V3FIT, Fig. 4.15. The resultant flux function plots for $\epsilon(s)$ and $n_e(s)$ are reproduced from the final fit profiles from V3FIT, 4.16. Note that the V3FIT fitted profiles are hollow, whereas the profiles mapped to NCT are peaked. Finally, the plots for synthetic and observed diagnostic outputs from the Bergerson paper are compared to the results from V3FIT, Fig. 4.17. The V3FIT helical distortion is evidently smaller in amplitude, but persists across a greater number of flux surfaces than the NCT solution. Both codes fit the profiles adequately, although it should be noted that a single shot with all diagnostics is being fit by V3FIT, so data has not been selected for the best fit for a given diagnostic.

A converged equilibrium ideally has $g^2 = \sum_i \kappa_i = 200$, a 40% decrease in g^2 and a corresponding 25% decrease in $\langle S_i^m - S_i^o \rangle$ from the currently reconstructed equilibria.

Figure 4.15: Flux surfaces generated by V3FIT reconstruction. A Shafranov shift of $\Delta R_{0,0} = 3.2$ cm is seen, along with a helical shift of $\Delta R_{1,0} = 17.5$ cm.

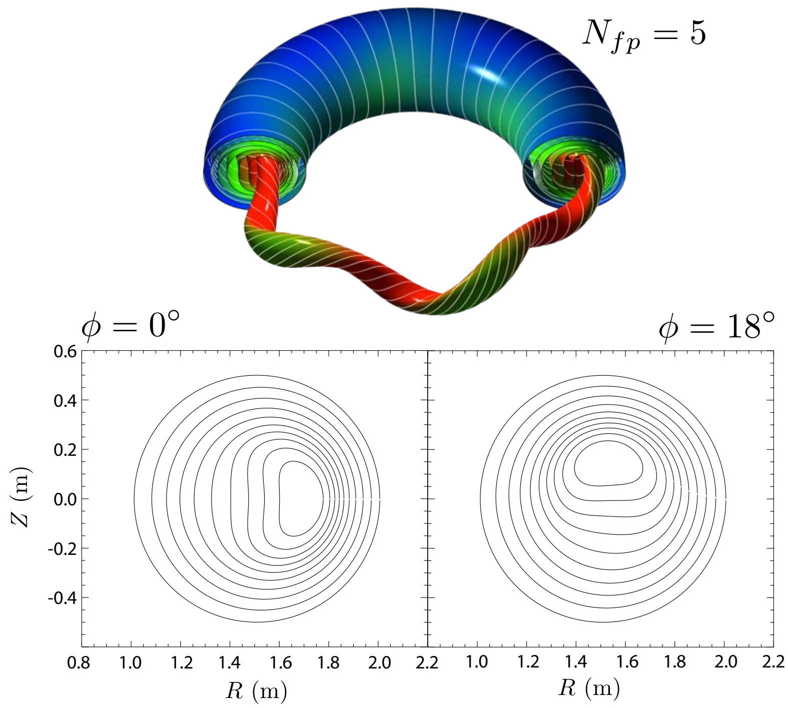

Figure 4.16: Output $n_e(s)$ and $\epsilon(s)$ mapping to flux surfaces from V3FIT. Both profiles are hollow and broad.

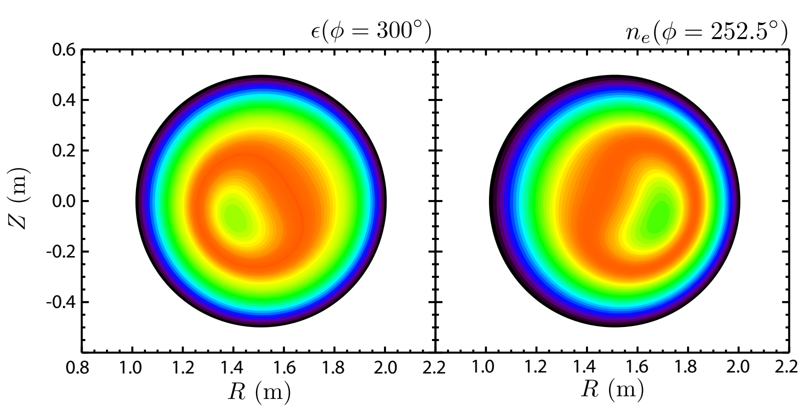

Figure 4.17: Synthetic (V3FIT) vs. measured values for FIR Interferometer-Polarimeter measurements.

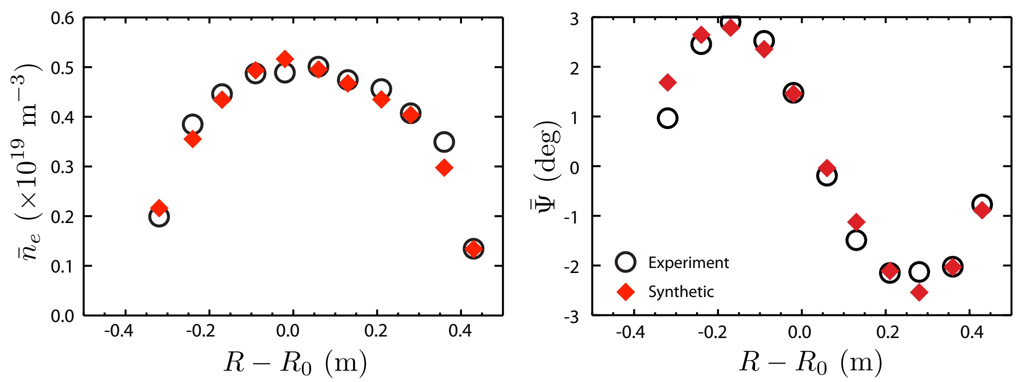

Nonetheless, the profile produced is both an equilibrium satisfying $\mathbf{J} \times \mathbf{B} = \nabla p$ force balance, and a fit to the data within $\langle S_i^m - S_i^o \rangle = 1.3\,\sigma_i$. The usefulness of a 3D VMEC equilibrium in calculating the Alfvén continuum and eigenmodes is retained.

4.3.2 3D Alfvén Continuum and AEs

The reconstructed equilibrium from Figs. 4.15 and 4.16 is used with Stellgap and AE3D to generate an Aflvén continuum and the AEs. The Boozer coordinates used in these codes readily accept three dimensional variations in the plasma, so they may be straightforwardly applied to the VMEC equilibria according to the method described at the beginning of this chapter. The density profile $n_e(s)$ has conveniently been iteratively solved for by V3FIT in the reconstruction, allowing it to be directly used in the calculations.

The continuum calculated by Stellgap is significantly different than the continua generated from axisymmetric equilibria, Fig. 4.18. The continuum branches now have extended flat or $\partial\omega/\partial r$ =const. regions. Due to the change in the q profile and resulting change in $k_{\|}$, the $n = 5, m = 1$ and $n = 6, m = 1$ continuum branches lose their zero-frequency points. The continuum gap has moved to $300 - 400$ kHz,

Figure 4.18: 500 kA $q_a = 0$ Alfvén continuum in a helical state. The $n = 4$ and $n = 5$ zero crossings disappear due to the change in $k_\parallel$ from a lowered q profile. The $n = 6, m = 1$ branch has an extended flat area.

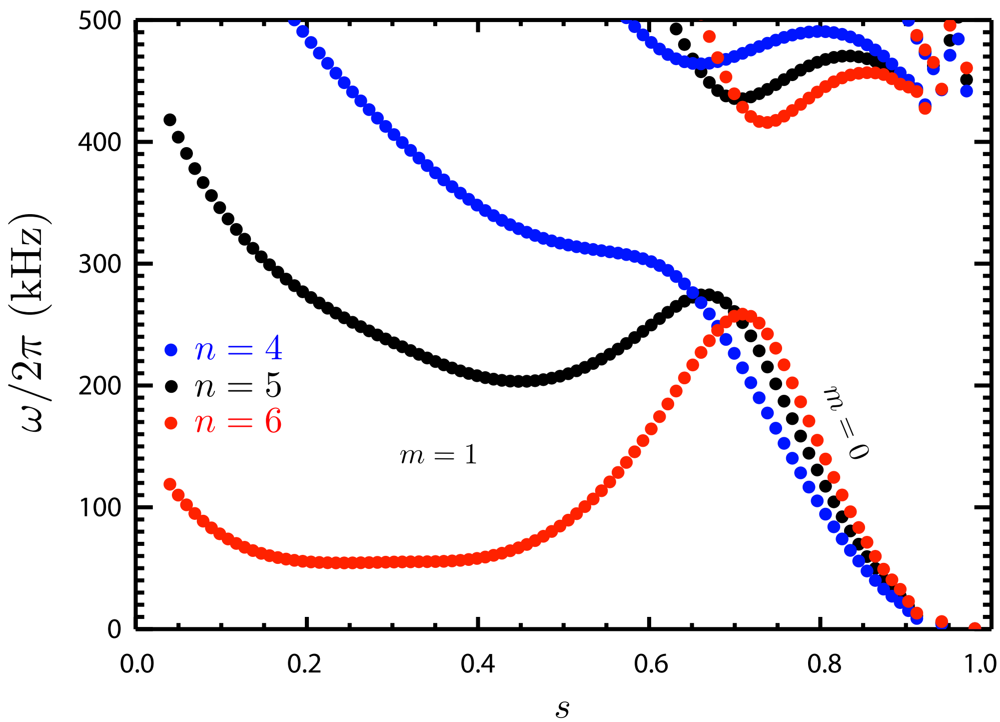

consistent with an upshift due to v_A from high $|B| \propto I_p$. The $n = 6$ inner continuum branch flattens over much of the core due to the change in $k_\parallel$.The gap also has a greater slope in frequency space.

The AEs in the three dimensional plasma are similar to the axisymmetric solutions, albeit higher in frequency, Fig. 4.19. No $n = 4$ TAE was found. The downward spike in the $n = 5$ TAE eigenfunction is a result of a core continuum crossing at $\omega/2\pi = 383$ kHz, whose resonant location can be seen in Fig. 4.18. The $n = 6$ TAE has an extended $m = 1$ component where its $m = 1$ branch is flattened in the continuum.

Figure 4.19: $n = 5$ and $n = 6$ TAEs in a 500 kA $q_a = 0$ helical plasma. They appear similar to the 300 kA non-reversed case, although the $n = 5$ has a continuum crossing and both TAEs are at higher frequency.

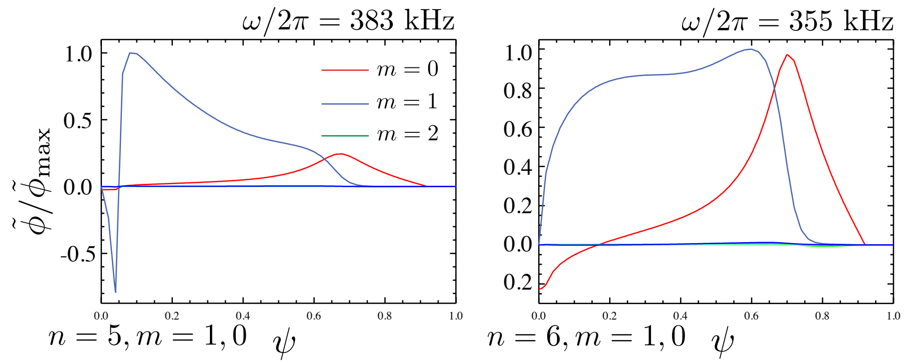

4.4 Summary

Using MSTFIT equilibria imported into VMEC, Alfvén continua were generated using AE3D and Stellgap for non-reversed, standard and deeply reversed plasmas. The lowest n eigenmodes and continua have dominantly $m = 0, 1$ coupling, and solutions in several plasmas are similar except for the coremost resonance and mode branches outside the reversal surface. The toroidicity-induced Alfvén eigenmodes had global extent and TAE frequencies ranged from $200 - 400$ kHz. The TAEs from the reversed case resembled those in the non-reversed case, with $m = 0, 1$ coupling for $n = 4$ through $n = 6$. At moderate n in deeply reversed plasmas, mode coupling occurred outside the reversal surface. Three dimensional equilibria were generated for the SHAx cases presented in previous papers using V3FIT. The equilibrium reconstructions converged and fit the data well. The continuum solutions show an increase in central $\omega \propto k_\parallel$, with the same $m = 0, 1$ coupling seen in axisymmetric plasmas. Eigenmodes in the helical equilibrium are similar to the axisymmetric cases, albeit at higher frequency.

Chapter 5

Characteristics of observed Alfvénic modes

The rapid growth of energetic particle modes and Alfvén eigenmodes can induce rapid transport of fast ion populations confined with plasmas. EPMs arise from the resonance between the characteristic frequency of a large group of fast ions and a point in the Alfvén continuum. As shown in Chapter 1, such a group exists due to neutral beam injection. For the first time on the RFP, a beam-driven instability has been observed and characterized. The analysis was performed using the toroidal and poloidal arrays of magnetics detailed in Chapter 2, along with interferometry and polarimetry. The Alfvén continua generated in Chapter 4 provide context and insight into the resonance location of the EPM.

This Chapter details the method by which bursts with coherent frequency and mode number were extracted from magnetics signals. Then the mode characteristics are detailed. The effect of the magnetic bursts on the fast ion population is discussed, and finally an overview of the work done on characterization of the internal mode structure is presented.

5.1 Numerical Methodology

The observed magnetic signatures of AEs and EPMs on other devices have been both transient and nonstationary in frequency space[14]. For this reason, the development of a scheme by which to identify the frequency and time of short bursts signals was sought. The analysis of MST magnetic signals to find these modes utilizes the toroidal array, processed through three successive stages: a spatial Fourier decomposition, a wavelet transform, and an event tagging scheme similar to previously used sawtooth ensembles [61]. The principle behind each method is described along with the practical usage parameters.

An arbitrary vector, or signal, $\mathbf{f}_i$ may be described by any complete set of normalized vectors,

$$\mathbf{f}_i = \sum_i a_i \mathbf{v}_i.$$

Vector notation is used because physical signals are discrete functions, and all calculations will be performed on these signals. In the most straightforward case, the unit vectors corresponding to each element of $\mathbf{f}_i$, $\mathbf{x}_i$, are used. Each unit vector corresponds to a time or spatial point, and its weight a_i is the value of $\mathbf{f}_i$ at that point, or

$$\mathbf{f}_i = [f_1, f_2, f_3 \cdots f_n]^{\mathbf{T}} = \sum_i a_i \mathbf{x}_i$$

$$\mathbf{x}_1 = [1, 0, 0 \cdots 0]^{\mathbf{T}}$$

$$\mathbf{x}_2 = [0, 1, 0 \cdots 0]^{\mathbf{T}}$$

$$\mathbf{x}_n = [0, 0, 0 \cdots 1]^{\mathbf{T}}$$

$$a_i = f_i$$

The basis vectors need not be orthogonal, $\mathbf{v}_i \cdot \mathbf{v}_k = 0$. If there are more vectors than the number of points in the signal, the set of vectors cannot be linearly independent.

In order to transform from a description by this set of vectors to one where

$$\mathbf{g}_i = \sum_i^N b_i \mathbf{u}_i,$$

the matrices $\mathbf{U}, \mathbf{V}$ are needed, where $\mathbf{V}$ is a matrix whose ith column is $\mathbf{v}_i$ and $\mathbf{U}$ is a matrix whose ith column is $\mathbf{u}_i$. For the case where $\mathbf{f}_i$ is comprised of spatial or time points, $\mathbf{V} = \mathbf{I}$. The transformation matrix is $\mathbf{T} = \mathbf{U^{-1}V} = \mathbf{U^{-1}}$,

$$\mathbf{g}_i = \mathbf{U^{-1}f}_i.$$

For the most straightforward case of "transforming" into the same space using the $\mathbf{x}_i$'s, the matrix for transformation is merely the identity matrix $\mathbf{I}$ and

$$\mathbf{f}_i \cdot \mathbf{I} = \mathbf{f}_i.$$

It is important to remember that a basis transformation is only a dot product, and a dot product is only a test of how similar two functions are. An "overcomplete" set of vectors spans the space, but is not linearly independent and has more vectors than signal points. After transformation to an ovecomplete basis from an orthogonal complete basis, the total amount of information in the transform will be "padded" with degenerate data. Performing the inverse transform on only a subset of the transformed data can return the original signal.

5.1.1 Fourier Transform of Array Data

The Fourier transform is a basis transformation to the orthogonal, complete set of basis functions comprised of the sine and cosine functions:

$$u_{is}(x) = \sin(2\pi i x)$$

$$u_{ic}(x) = \cos(2\pi i x)$$

In the case of digital signals, the functions and coordinates are discrete, and the discrete-time Fourier transform (DTFT) is used. In the case of a signal with N points where n is the index, the vector representation of sine and cosine functions is

$$\mathbf{u}_{is}[n] = \sin\left(\frac{2\pi i n}{N}\right)$$

$$\mathbf{u}_{ic}[n] = \cos\left(\frac{2\pi i n}{N}\right)$$

$$1 \leq i \leq N/2,$$

where a single $i = 0$ term for a constant offset is retained as well. If the system is unevenly binned, it is necessary to replace n with $x[n]$, the point of measurement, and N with L, the total span of the measurement. The designator for the new basis is the frequency, $f(i) = i/L$.

At $i = N/2$, $\mathbf{u}_i[N/2] = [\cos(\pi n), n = 0, 1, 2...] = [1, -1, 1, -1 \cdots]^{\mathbf{T}}$, which is the maximum resolution of the system. At $i > N/2$, the sinusoidal functions vary faster than π radians per index, so that $\mathbf{u}_{(N/2+1)c} \cdot \mathbf{u}_{(N/2-1)c} \neq 0$ and $\mathbf{u}_{(N/2+1)s} \cdot \mathbf{u}_{(N/2-1)s} \neq 0$. The Nyquist frequency, the frequency corresponding to the minimum periodicity interval of the sinusoidal basis functions, is then equal to 1/2 the number of points in the signal. This provides the exactly N basis functions necessary to form a complete, orthogonal set.

The DTFT is the transform of a signal using the Fourier basis functions in vector form,

$$\mathbf{g}_i = \mathbf{U}_s^{-1}\mathbf{f}_i$$

$$\mathbf{g}_{N/2+j} = \mathbf{U}_c^{-1}\mathbf{f}_i,$$

although the indices may be arranged differently with respect to the sine and cosine components.

For spatial mode decomposition using the toroidal array on MST, the argument to the sinusoidal functions is $(2\pi i\, x[n]/360)$, where $L = 360$ is chosen to describe one toroidal transit of 2π radians. The j indices are then properly toroidal mode numbers, where $n_i = i$. The values for $\mathbf{f}_i$ are the measured $\dot{B}$ at the magnetic coils in either the θ or ϕ direction at a single time point, and the $x[n]$ values correspond to the toroidal locations of the coils as described in Eq. 2.2. The poloidal array mode decomposition is handled similarly, with the exception that the poloidal mode numbers are found, and the locations of the $x[n]$ are taken from Eq. 2.4. The $\mathbf{f}_i$ values returned are then $\dot{\mathbf{B}}_n$ and $\dot{\mathbf{B}}_m$ for each case. The transform is performed for each point in time, so $\dot{\mathbf{B}}_n(t[n])$ and $\dot{\mathbf{B}}_m(t[n])$ are constructed, where each mode number corresponds to a time series $t[n]$ of $\dot{B}$ values.

5.1.2 Wavelet Transform of Time Series

The wavelet transform provides a compromise between the frequency localization of the Fourier decomposition and the temporal localization of the original signal basis. The following discussion is informed by the 1998 guide to wavelets by Torrence [62] and the 2009 tutorial on wavelets by Yan [63]. Recall that a basis transform is a dot product, which is a test of how alike two vectors are. By tapering the sinusoidal perturbations with a windowing function, they can be temporally localized. The form of a simple wavelet is

$$f_j(t) = \frac{1}{\sqrt{s}} W\left(\frac{t-\tau}{s}\right) \sin\left(\frac{d\,(t-\tau)}{s}\right), \tag{5.1}$$

where s is the scale parameter that modifies frequency, wave packet size and amplitude, d is a fixed parameter to determine the number of wave periods in the window, τ describes time shifts to move the wavelet, and W is a windowing function such as a Gaussian. j is used as the index because wavelet transforms are often performed with overcomplete bases. Because the multiplicative inclusion of windowing is itself a function with a finite Fourier-transformed amplitude, frequency localization is weaker than in the Fourier transform. One sinusoidal period in time is necessary to resolve frequency, therefore temporal localization is also weaker than in the untransformed signal.

The strength of this approach is that, by varying τ, the window can be moved along the signal, providing frequency data as a function of time. The resultant $f_j(t)$ then has temporal information like the original signal, and frequency information like the Fourier-transformed signal. Intuitively, the matrix transformation is then more sparse than the Fourier transform, containing zeros outside the relevant window.

The value of the scale parameter s is in its locking of frequency, window size and amplitude. The shape of the wavelet is unaltered as s is varied - the function is only stretched. Compared to the windowed Fourier transform (WFT), there are a number of advantages. The WFT takes the form

$$f_{j\mathrm{WFT}}(t) = W\left(t - \tau, L_W\right) \sin\left(\frac{j\left(t-\tau\right)}{L_W}\right), \tag{5.2}$$

where L_W is a fixed window length. L_W is fixed and j varies, fitting multiple frequencies inside a single window that slides along the signal. The weakness of this approach is that the temporal resolution $\Delta\tau$ is fixed by L_W and the frequency resolution Δf is fixed by the number of wave periods that fit inside L_W. In the case of the wavelet transform, the ratios $\Delta\tau/\tau$ and $\Delta f/f$ are fixed. The locking provided by s preserves these ratios. This locking is desired compared to the WFT because of the nature of transient signals. For signals that rapidly change in frequency or appear in bursts, the WFT provides unnecessary and deceptive frequency resolution at higher frequencies, sacrificing temporal resolution in the process. By convoluting a less transient basis function with a high-amplitude transient signal, a low amplitude result with high frequency resolution is found. However, a transient signal has inherently low frequency coherence. The real signal is changing rapidly either in amplitude or frequency, and is thus best fit with wavelets whose forms mimic the signal features. By choosing d in the wavelet transform, the ratio of frequency resolution to temporal resolution is chosen, and this balance is preserved for all frequencies.

The discrete Wavelet transform (DWT), similar to the DTFT, is performed on a signal vector. The continuous form of the Morlet wavelet set, which was used in the analysis for EPMs, is

$$w_{js}(t) = \frac{1}{\pi^{1/4}\sqrt{s_j}} \exp\left[-\frac{1}{2}\left(\frac{t-\tau_j}{s_j}\right)^2\right] \sin\left(d\left(\frac{t-\tau_j}{s_j}\right)\right) \tag{5.3}$$

$$w_{jc}(t) = \frac{1}{\pi^{1/4}\sqrt{s_j}} \exp\left[-\frac{1}{2}\left(\frac{t-\tau_j}{s_j}\right)^2\right] \cos\left(d\left(\frac{t-\tau_j}{s_j}\right)\right). \tag{5.4}$$

The form of the wavelet as well as its scaling with s_j and d is shown in Fig. 5.1. As with Fourier transforms, both sine and cosine terms are used to capture phase. The s_j values range from arbitrarily small up to the length of the signal, and should be of a set $s = s_0 \cdot 2^l$, where l is an integer. Overcomplete representations often use octaves instead, where l is a multiple of 1/8. To approximate the continuous wavelet transform, the τ_j values chosen for the DWT are one Nyquist period apart, although this causes the basis to be strongly overcomplete. In order to transform back to the original basis, only the subset of the new basis functions where l is an integer and τ_j values are $s/2$ separated should be used. It is the shift τ_j and the scale s_j that form the final time-frequency map of the transformation. The value for d is commonly chosen to be $d > 5$, as lower values may result in a non-zero offset of the wavelet functions. Higher values result in greater frequency resolution, while lower values result in higher temporal resolution. Although it is tempting to call d/s_j the frequency, in reality a Fourier transform must be performed on the basis functions to determine their center frequencies.

Figure 5.1: The Morlet wavelet sine and cosine components for several values of s and d. Increasing s stretches the wavelet and decreases its amplitude. Increasing d adds more internal oscillations to the wavelet.

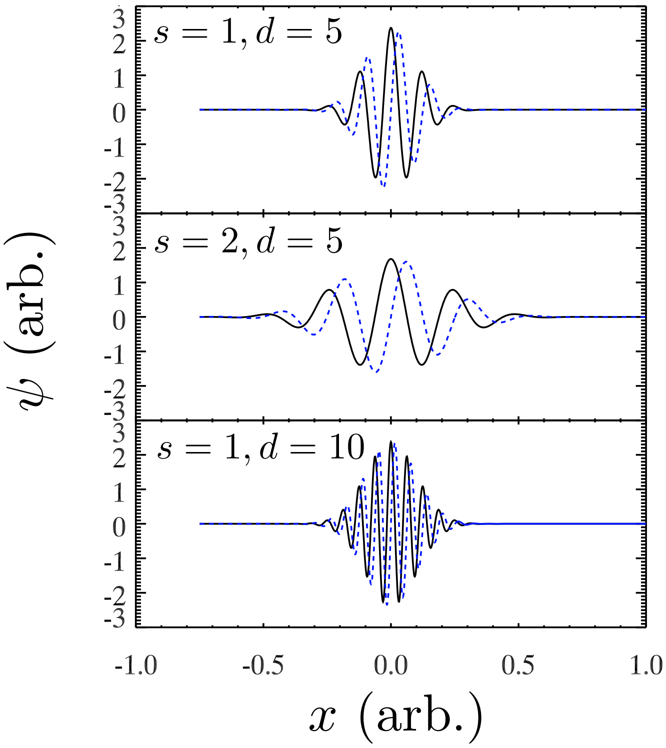

In the vector form used for mode analysis, the sine and cosine terms are combined into a complex exponential, resulting in a complex output that captures the phase. The wavelet transform vectors are

$$\mathbf{w}_j[n] = \frac{1}{\pi^{1/4}\sqrt{s_j}} \exp\left[-\frac{1}{2}\left(\frac{t[n]-\tau_j}{s_j}\right)^2\right] \exp\left[-id\left(\frac{t[n]-\tau_j}{s_j}\right)\right] \tag{5.5}$$

where the assumed $\mathbf{f}_i[n]$ vector is any signal with respect to time. $\mathbf{W}$ is a matrix with a number of rows equal to the length of $\mathbf{f}_i$ and whose jth column is $\mathbf{w}_j[n]$.

In the mode analysis, the wavelets are used to transform each of the $\dot{\mathbf{B}}_i[n]$ signals, where the i denotes the original time basis and a single m or n signal is transformed at a time. The basis transformation

$$\dot{\mathbf{B}}_j = \mathbf{W}^{-1}\dot{\mathbf{B}}_i \tag{5.6}$$

is a map of a one-dimensional vector $\dot{\mathbf{B}}_i[n]$ to another one-dimensional vector $\dot{\mathbf{B}}_j[j]$. However, the result can be represented two-dimensionally as $\dot{\mathbf{B}}_j[\tau, s]$ because both τ_j and s_j are uniquely determined by the index j. By assigning the center frequency $\langle f \rangle_s$ from Fourier decomposition of the original wavelet, the map is instead cast as $\dot{\mathbf{B}}_j[\tau, \langle f \rangle_s]$. It is important to note that the map $\dot{\mathbf{B}}_j[\tau, s]$, known as a time-scaleogram, is the exact mapping of the data to wavelet basis functions, while, $\dot{\mathbf{B}}_j[\tau, \langle f \rangle_s]$, the time-spectrogram, is an approximation based on central frequencies. The time-scaleogram is the more accurate representation of the data, but frequency is often preferred for calculations and ease of understanding, and so time-spectrograms are presented here.

In the time basis, integration is required to remove the d/dt effect on the magnetic signals. However, if the signals are assumed to be sinusoidal, this component can be extracted in frequency space.

$$B_\omega = B_0 \sin(\omega\, t[n])$$

$$\dot{B}_\omega = \omega B_0 \cos(\omega\, t[n])\,.$$

The contribution of the frequency $\langle f \rangle_s$ is divided out of the wavelet signals, resulting in the final output $\mathbf{B}_j[\tau, \langle f \rangle_s]$, whose phase is reversed in time and shifted by 90° (due a derivative of cosine and sine functions). The correct phase of $\mathbf{B}_j[\tau, \langle f \rangle_s]$ is recovered by manually adjusting the phase, which is the equivalent of a Hilbert transform.

The Morlet wavelet is employed for these wavelet transforms, with $d = 10$ to obtain high frequency resolution. The resultant time-spectrogram can be produced for any n and m with data from the toroidal and poloidal arrays. The most common transient features observed are "bursts" whose frequency is coherent but whose amplitude is rapidly changing in time. The time-spectrograms range from 20 Hz up to the Nyquist frequency, and can be used to look for any changing magnetic fields as a function of time.

5.1.3 Event Tagging and Analysis

In order to find and ensemble a large set of events, two routines are employed. The first routine generates spectrograms, identifies large amplitudes at relevant frequencies, filters for false positives using other signals, and finally records the shot number, time spread, frequency spread and amplitude of each burst. The second routine takes this burst list as an input and performs a number of functions, from correlation analysis for each burst to estimating the core Alfvén speed for each burst based on internal diagnostics.

The burst identification code takes as an input a list of shots, a relevant frequency range or minimum frequency f_{min}, a relevant time window, and a minimum fluctuating amplitude $\tilde{B}_{\text{min}}$. The list of shots allows ensembling to be done on similar plasmas and only on shots with the neutral beam running. The choice of f_{min} is important because the code does not screen out the tearing modes, whose rotation frequency is $f < 40$ kHz. In general, $f_{\text{min}} = 60$ kHz is chosen to exclude these low frequency modes. The time window allows plasma ramp-up and ramp-down phases to be excluded, and allows the neutral beam duration to be focused on. Finally, $\tilde{B}_{\text{min}}$ is crucial for screening out noise and setting the threshold for "good" bursts.

Inside the specified time and frequency window applied to the $\mathbf{B}_j[\tau, \langle f \rangle_s]$ signal, the algorithm finds the maximum B amplitude. If this amplitude occurs in the bottom-most frequency band, it is discarded and $\mathbf{B}[\tau, f_{\text{min}}]$ is zeroed to remove the tails of lower frequency modes. If this amplitude is below the threshold, it is likewise discarded. The spectrum of at this time point $\mathbf{B}_\tau[\langle f \rangle_s]$ is chosen, then a simple Gaussian with a linear offset is fit to amplitude versus frequency. The peak of this fit is recorded as f_{peak}, and the full-width half-maximum (FWHM) values of the frequency, f_{low} and f_{high}, are calculated from the square root of variance, σ, from the Gaussian fit. The code then returns to the original $\mathbf{B}_j[\tau, \langle f \rangle_s]$ map and finds the temporal FWHM by tracing the amplitude contours in time. The start and end times, t_{start} and t_{end}, are recorded at these FWHM points. The end result is a box in $\mathbf{B}_j[\tau, \langle f \rangle_s]$ space. All B values inside an area twice the size of this box and centered at the same point are zeroed to exclude them from the next scan. This zeroing results in a "hole" in the time-spectrogram. The code iterates this procedure and returns a list of bursts across many shots and times.

Further processing of this list is performed after bursts are selected. The $B_{m=0}$ signal is checked for high amplitude spikes, and coincident bursts are discarded to remove magnetic signatures from sawteeth. The $\bar{n}_e$ signal from the FIR or CO2 system is also checked to make sure that data is available for v_A calculation.

The burst analysis portion of the code takes the burst list as an input and performs various analyses using several other signals. It is in this routine that the signals in Table 2.3 are examined for each burst, either as a time-averaged value or a full time trace. Multiple time-averaged values are tabulated for each burst, allowing frequency or amplitude scaling to be extracted by comparison with the listed burst parameters. This method is used to compare core Alfvén speed and beam energy to burst frequency. Full time traces are averaged together over each burst to determine average behavior, or their correlation with each other at each burst is averaged together. This method is used to determine, for instance, ANPA signal drops across bursts.

5.2 Burst Characteristics, Scaling, and Prevalence

Original detection of the EPM bursts occurred by visual analysis of the $\mathbf{B}_j[\tau, \langle f \rangle_s]$ maps throughout the duration of NBI, during 300 kA plasma shots with edge safety factor fixed at $q_a = 0$ and with $\bar{n}_e = 0.7 \times 10^{19}$ m^{-3}. The rate of bursting in non-reversed plasmas is the highest and the greatest amount of secondary analysis has been performed on them, so the characteristics of bursts in this equilibrium will be described as the base case. Helical plasmas, reversed plasmas and deeply reversed plasmas will then be compared to this base case.

5.2.1 Non-Reversed Plasmas

Bursts with toroidally coherent periodic magnetic structure are observed during NBI in Fig. 5.2. This case shows a single plasma shot from 10 to 40 ms. The plasma parameters as a function of time, I_p, $\bar{n}_e(0)$, and P_{beam} are plotted with the $\mathbf{B}_{\theta,n=4}[\tau, \langle f \rangle_s]$ and $\mathbf{B}_{\theta,n=5}[\tau, \langle f \rangle_s]$ time-spectrograms. The Alfvén continuum for these type of plasmas is shown in Fig. 4.1. When the beam turns on, there is a delay of $\approx 3ms$ before bursts appear. Coherent $n = 5$ magnetic perturbations appear in bursts at frequency $f_{\text{peak}} \approx 90$ kHz. The bursts rapidly grow to amplitudes of $\tilde{B}_\theta < 2$ G and decay to noise level within ≈ 150 μs. After correcting for the Doppler shift due to plasma rotation, the average burst frequency is 65 kHz. Immediately following the $n = 5$ bursts are similar $n = 4$ bursts with a frequency of $f_{\text{peak}} = 160$ kHz, whose growth begins approximately when $\tilde{B}_{\theta,n=5}$ reaches its peak. Correcting for Doppler shift, this $n = 4$ frequency is 140 kHz. The $n = 4$ bursts reach their own peak amplitude of $\tilde{B}_{\theta,n=4} < 2$ G between 40 and 60 μs later. Although the $n = 4$ bursts can have amplitudes up to 2 G, across many bursts $\langle \tilde{B}_{\theta,n=4} \rangle = 0.6$ G, compared to $\langle \tilde{B}_{\theta,n=5} \rangle = 1.7$ G. Due to

Figure 5.2: Wavelet spectrograms of $n = 4$ and $n = 5$ bursts in a shot from the base case. Bursts appear during beam injection at constant frequency, and turn off with the beam.

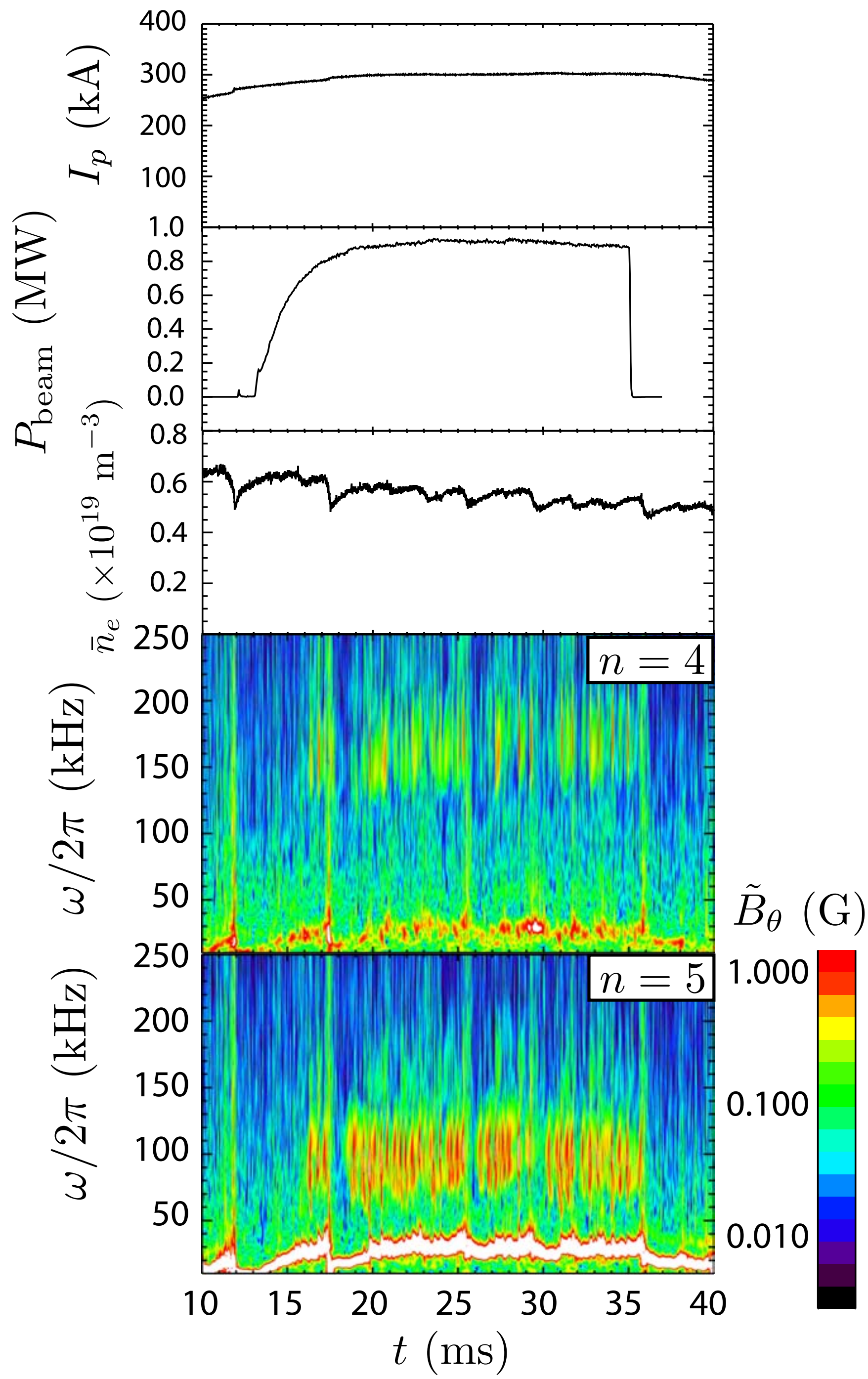

their lower amplitude and wider variability in amplitude, the $n = 4$ bursts are not always evident after $n = 5$ bursts, although they may be falling below the noise level of the magnetic signal.

The particular case of $n = 5$ bursts followed by evident $n = 4$ bursts in non-reversed plasmas was studied extensively, and is discussed in this section. Neutral beam injection prompts magnetic activity in a plasma that already contains magnetic effects from tearing modes and sawteeth. The physics behind the studied bursts is both interesting and the most readily quantifiable.

Figure 5.3: A single burst on a single coil, resolved into $n = 4$, $n = 5$ and $n = 1$ components

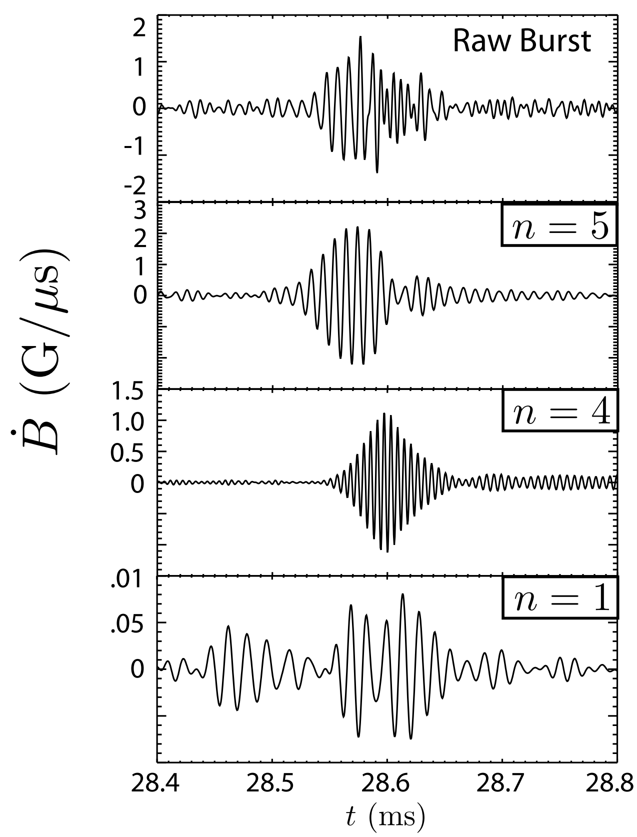

The 1D raw trace of the poloidal magnetic field signal $\tilde{B}_\theta$ from a single coil, filtered to exclude the tearing mode frequencies, shows a burst that grows rapidly

Figure 5.4: Time evolution $\dot{B}_p$ of a burst across all coils. An $n = 5$ perturbation appears, then transitions to an $n = 4$ perturbation, mitigated by a counter-propagating $n = -1$ burst.

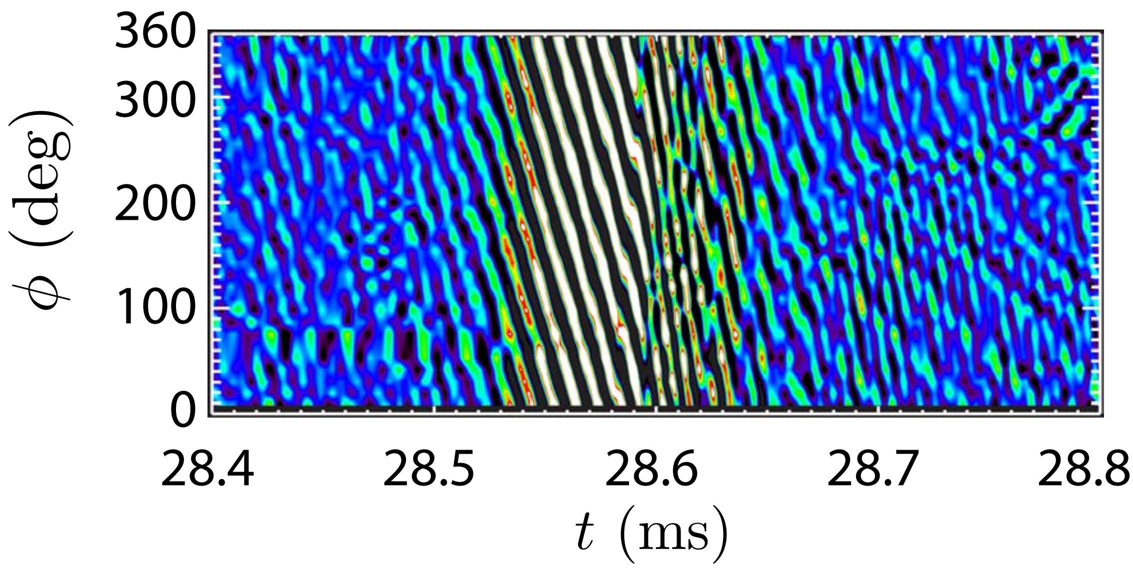

in time and changes frequency, Fig. 5.3. When filtered into $n = 5$, $n = 4$ and $n = 1$ components, the frequencies correspond directly to toroidal harmonics. The structure of the signal is similar to early fishbone modes seen in tokamaks [64], but this similarity is merely indicative of a mode that grows rapidly in time and damps rapidly. A more complete picture of the filtered $\tilde{B}_\theta$ signals contains all 32 coils in the toroidal array, where the 3 wave components are evident, Fig. 5.4. The $n = 5$ perturbation grows, then transitions via an $n = 1$ intermediary to a higher frequency $n = 4$ state. It is clear from this picture that the intermediate mode is $n = -1$, as it propagates counter the toroidal angle. As discussed in Sec. 1.3, $n < 0$ is used to refer to the counter-propagating modes whose continuum slope is $\partial\omega/\partial r < 0$.

The poloidal array at $\phi = 177°$ was used to determine the polarization and poloidal mode number m of the bursts. 8 of the 16 sets of B_ϕ and B_θ facing coils were monitored to resolve $m = 0 - 3$ in correlation with the $n = 5$ bursts. The modes do not obey the expected polarization condition set by the conducting boundary, and the mode is composed of two dominant poloidal harmonics with nearly equal amplitude.The dominant poloidal mode is $\tilde{B}_{\phi,m=0}$, with an amplitude $\tilde{B}_{\phi,m=0} = 2.3$ G. The limiter excludes the $\tilde{B}_{\theta,m=0}$ mode, whose amplitude is $\approx .25$ G and may be attributed to aliasing. While the $\tilde{B}_{\phi,m=1}$ signal carries a significant amount of noise, correlation shows that its amplitude is $\tilde{B}_{\phi,m=1} = 1.7$ G. Finally, the B_θ signal, $\tilde{B}_{\theta,m=1} = 1.8$ G is within calibration errors and secondary mode contributions from $\tilde{B}_{\theta,n=5} = 1.7$ G, Fig. 5.5. The limiter also fixes $j_r = 0$ in the current-free region at the edge of the plasma. When combined with Ampere's law, $\nabla \times \mathbf{B} = 0$, the ratio $\tilde{B}_\phi / \tilde{B}_\theta = (na) / (mR_0)$ is fixed as well. Predicted amplitudes for correlated signals of $m = 1, n = 5$ bursts are $\tilde{B}_\phi / \tilde{B}_\theta = 1.6$, but measured amplitudes are $\tilde{B}_\phi / \tilde{B}_\theta \approx 1$. The discrepancy could be due to small coupled $\tilde{B}_{\phi,n>5}$ modes that are out of phase with the dominant $n = 5$ perturbation. As $\dot{B}_\phi$ was not measured from the toroidal array due to practical constraints on number of measured signals, this has not yet been confirmed.

Scaling studies were performed in non-reversed plasmas to determine frequency dependence on a number of parameters. To systematically alter $v_A = |B| / \sqrt{\mu_0 \rho_m}$, where $\rho_m = m_i n_i$, three plasma parameters were changed. The plasma current $I_p \propto |B|$ was scanned from $I_p < 200$ kA to $I_p = 400$ kA. The electron density, which by the charge neutrality condition $en_e = q_i n_i$, was scanned from $\bar{n}_e \approx 0.4 \times 10^{19}$ m^{-3} to $\bar{n}_e \approx 1.5 \times 10^{19}$ m^{-3}. The mass density and charge of the plasma ions was changed by switching fueling gas from deuterium, $m_D/q_D = 2m_p/q_p$, to hydrogen $m_H/q_H = m_p/q_p$, to helium, $m_{He}/q_{He} = 2m_p/2q_p = m_p/q_p$, where m_p and q_p are the mass and charge of a proton, respectively. The core Alfvén speed is scannable from $v_{A0} = 1 - 4 \times 10^6$ m/s, but decreased prevalence of bursts at high density and poor plasma conditions in low density hydrogen limited the effective range to $v_{A0} = 1.1 - 2.4 \times 10^6$

Figure 5.5: Burst amplitudes resolved by toroidal and poloidal mode number, versus $n = 5$ amplitude from the toroidal array. All other amplitudes are linear with $n = 5$ amplitude.

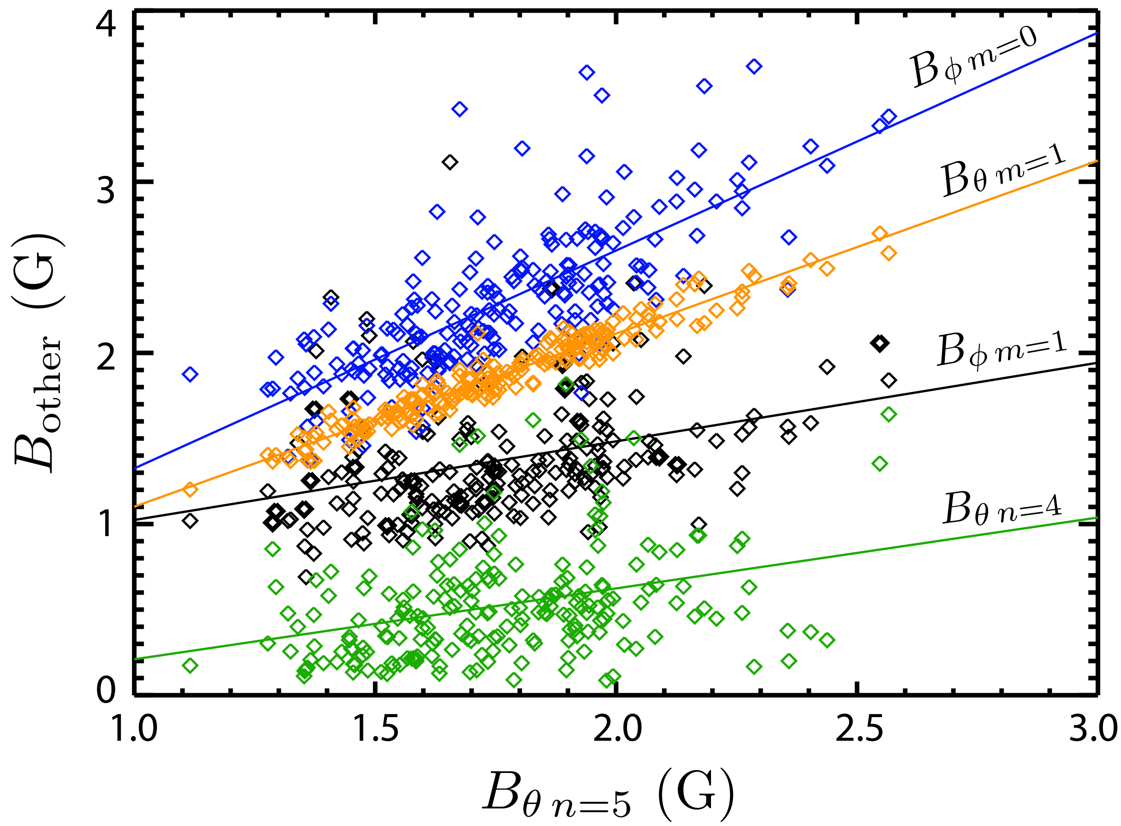

m/s.

The neutral beam injector is capable of injecting fast hydrogen or fast deuterium at a range of energies. Scaling studies covering the full extent of the NBI capabilities were performed in these plasmas, varying $I_{\mathrm{beam}} = 15 - 40$ A and $E_{\mathrm{beam}} = 17 - 25$ keV, corresponding to $v_{\mathrm{beam}} = 1.8 - 2.2 \times 10^6$ m/s. Beam scaling studies were performed on the base case of non-reversed plasmas.

Different frequency scalings for the two types of bursts were observed. The $n = 5$ bursts scaled weakly with core density and not with core magnetic field, Fig. 5.6. The density scaling $f_{n=5} \propto n_e^{-0.3}$ could be attributable to fast ion deposition, as

Figure 5.6: Scaling of the $n = 5$ frequency with magnetic field and density. There is no magnetic field scaling, and density scaling is weak.

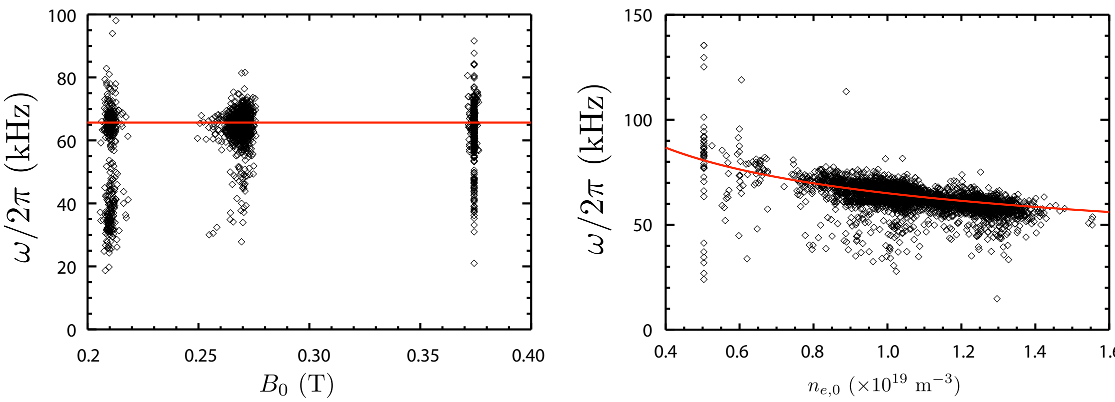

Figure 5.7: Scaling of the $n = 5$ bursts with $v_{\rm beam}$. The $n = 4$ bursts do not scale with beam velocity, but the $n = 5$ bursts do.

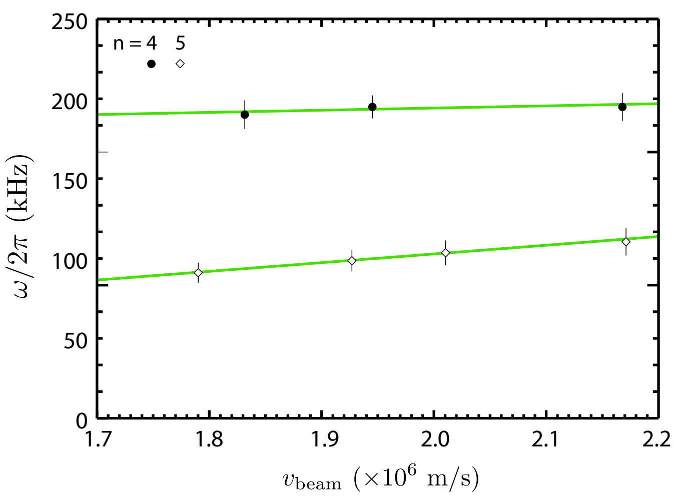

the NBI focus and direction are fixed but the beam ionization rate is proportional to density. This weak scaling persisted with respect to mass density, $f_{n=5} \propto \rho_m^{-0.3}$, which was investigated by switching the plasma ion species. The deuterium beam ions into hydrogen plasmas excited similar-frequency bursts to the hydrogen beam ions, albeit with greater frequency spread. No strong scaling with v_A was found for the primary bursts. The burst frequencies scaled strongly with the velocity of injected ions, $f_{n=5} \propto v_{\text{beam}}$, Fig. 5.7. Although the beam-born ions could not be varied widely in velocity, the intercept of a line of best fit to 4 beam energies passed through $f_{n=5} = 0, v_{\text{beam}} = 0$, suggesting a linear scaling.

Figure 5.8: Scaling of the $n = 5$ and $n = 4$ bursts with v_A. $n = 4$ scales strongly with v_A, while $n = 5$ does not. The fit line to the $n = 4$ frequencies is overplotted in green.

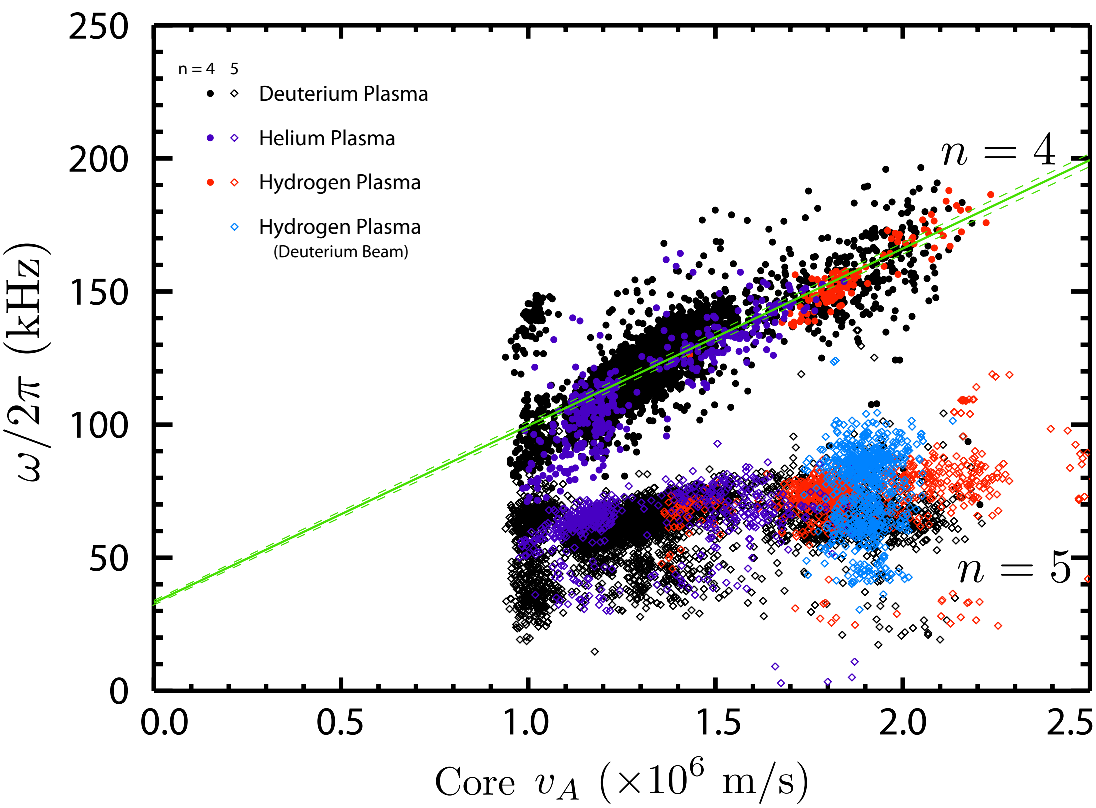

The $n = 4$ burst frequency scaled with core density and magnetic field individually. The bursts also changed frequency with m_i. The scaling with these 3 parameters is a strong confirmation of Alfvénic scaling, $f_{n=4} \propto v_A$. The computed wavenumber and offset values for $\omega_{n=4} = k_{\parallel} v_A + C$ is $k_{\parallel} = 0.43$ m^{-1} and $C = 31$ kHz. A line representing these values is included in Fig. 5.8. The $n = 4$ bursts were examined for beam scaling, and no correlation was found, Fig. 5.7.

Figure 5.9: Continuum calculation with crossing of the $n = 5$, $n = 4$ and $n = 1$ modes marked. Burst frequencies correspond to continuum crossings at several radii.

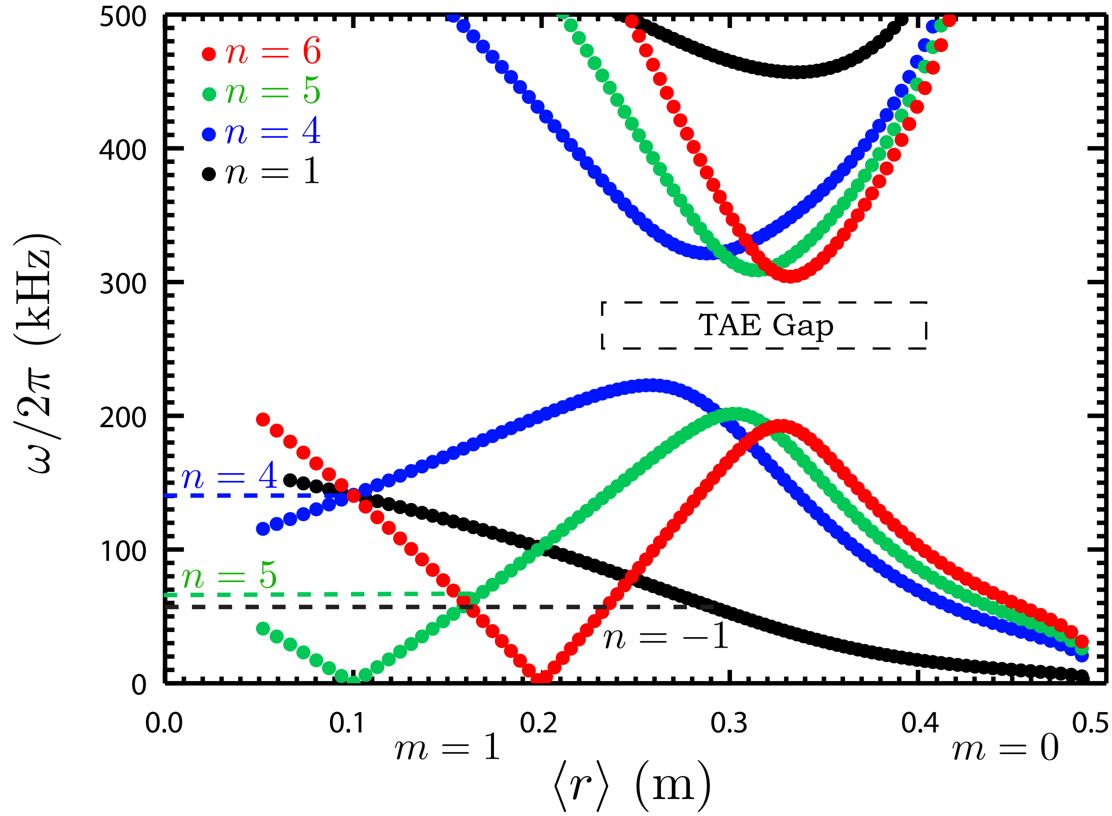

The observed $n = 4$ and $n = 5$ frequencies do not coincide with the TAE frequencies calculated using AE3D, but fall within the Alfvén continuum below the TAE gaps, Fig. 5.9. Inverse Landau damping is unlikely as the excitation mechanism because bursts still appear for $v_{\mathrm{beam}} > v_A$. The observed modes are likely two EPMs that couple the steepest gradient of the fast ion distribution to the nearest Alfvén continuum point that satisfies $k_{\|} v_A = k_{\| fi} v_{\mathrm{beam}}$. The circulating frequency $\omega_{\mathrm{circ}} = k_{\| fi} v_{\mathrm{beam}}$, where $k_{\| fi}$ is determined using q_{fi} from Section 1.3, is the most likely mechanism of coupling. ω_{circ} is close to the continuum frequencies calculated by Stellgap and the trapped fraction of particles is small as stated in Section 1.4.2. Assuming that primary continuum excitation occurs at the $n = 4/5, m = 1$ resonance, the observed frequencies permit calculation of the resonant surfaces, $r_{n=5} = 17$ cm and $r_{n=4} = 10$ cm. The $n = -1$ resonance is also evident at $r = 0.28$ m.

Figure 5.10: Picture of the mechanism for excitation by multiple flattening of the distribution function. The $n = 5$ burst flattens the distribution function, which steepens it near the $n = 4$ and $n = -1$ resonances.

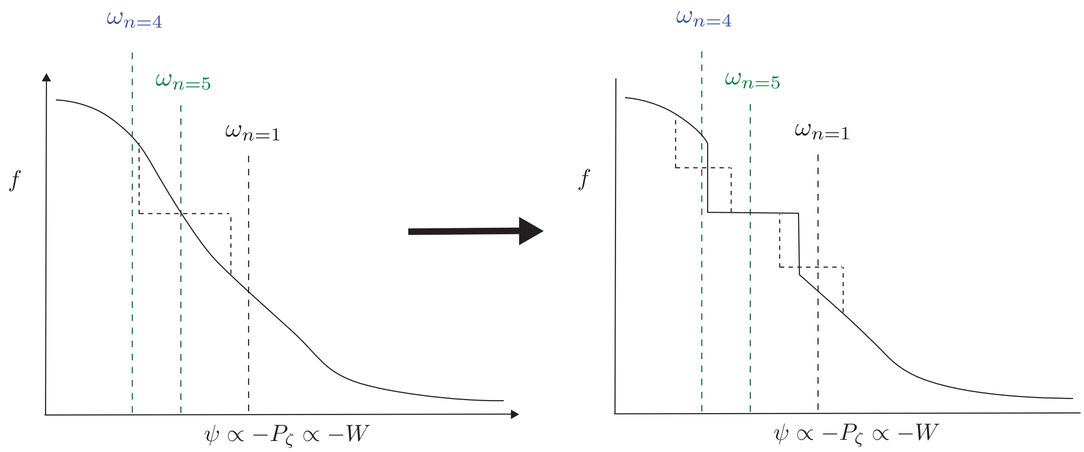

A picture that self-consistently explains the observed behavior is included in Fig. 5.10. The fast ion pressure gradient builds up over time, with a peak gradient at the $n = 5$ resonant surface. The frequency of the burst is set by ω_{fi} at the point of steepest gradient in the distribution function. The $n = 5$ mode burst convectively transports fast ions outward in radius, generating a new steep gradient in the core and at mid-radius. One gradient is localized at the $n = 4$ continuum resonance, and the another is localized at the $n = -1$ continuum resonance. Both these resonances then undergo convective transport, flattening the distribution function locally. The net effect is an outward convection of ions and an overall flattening of the distribution function. This type of process has been seen in tokamaks [65]. The NBI then rebuilds the distribution function by generating new fast ions, repeating the cycle.

The picture described above contains a caveat in order to explain the observed scalings. In the EPM picture, the beam-like distribution of particles will always determine the frequency of the $n = 4$ burst through its characteristic resonance, while the background plasma will only set the resonance location. The observed scaling contradicts this, as there is no beam velocity scaling but an evident scaling with v_A. It is possible to explain this mismatch with a "special radius" picture. The point where $\gamma_\uparrow - \gamma_\downarrow$ is at a maximum will be influenced by the changing slope of the Alfvén continuum. This slope sets $\gamma_\downarrow \propto d\omega/dr$. The slope of the distribution function sets the drive, $\partial f/\partial W \propto \gamma_\uparrow$, and this slope is likewise changing in the core of the plasma. The competition between damping and drive could strongly depend on $r(\omega_{\text{res}})$. In the $n = 5$ case, the slope around $(df/dP_\zeta^2)_{\text{max}}$ is constant and steep, localizing the resonance to the point "picked" by the beam ions. It is possible that the flattening of the distribution function from the $n = 5$ bursts continues inward until the subsequent local steepening at the $n = 4$ resonance causes the $n = 4$ drive over damping to reach a maximum. This could pick the resonance of the Alfvén continuum at a similar radius every burst. Because the Alfvn continuum at a given radius $\omega \propto v_A$, Alfvénic scaling will be observed. Alternately, initial work by Don Spong suggests that the $n = 4$ mode may be a Beta-induced Alfvén Acoustic Eigenmode (BAAE), a mode that has been observed on tokamaks [66, 67].

5.2.2 Standard Reversed Plasmas

In plasmas where $q_a < 0$, the mode bursts are less frequent and are higher in mode number. Two factors influence the change in character. First, standard plasmas have $q_0 < 0.2$, which lowers along with q_a, albeit weakly. Second, when the plasma is reversed, q_0 changes throughout the sawtooth cycle, decreasing from $q_0 \approx 0.2 \to 0.167$ between sawteeth [32], Fig. 5.11. As discussed in Chapter 4, the continuum branch locations depend heavily on q. As mentioned in Section 1.3, the $\omega_{\text{circ}} = k_{\| fi}\, v_{\text{beam}}$ values are also dependent on q_{fi}. There is no comparison information for polarization from the poloidal array at $\phi = 177°$ for standard plasmas, so B_ϕ is not known.

Figure 5.11: Evolution of the q profile throughout the sawtooth cycle. From [32]

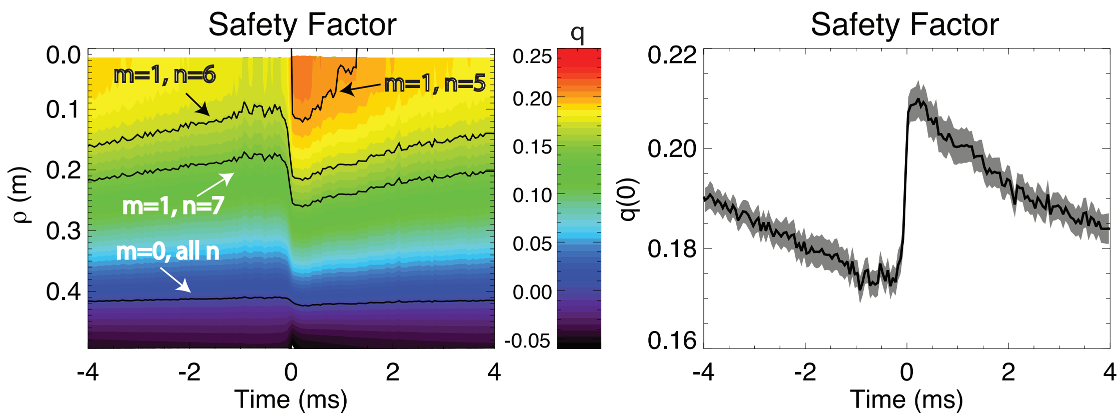

A typical case for a 400 kA plasma with $q_a \approx -0.04, \bar{n}_e = 0.7 \times 10^{19}$ m^{-3} is shown from 21 to 29 ms, Fig. 5.12. In this type of plasma, sawtooth bursts are stronger than the relaxation events in the base case, and they occur more frequently. 1-2 ms after each sawtooth, bursting modes with $n = 5$ appear at < 100 kHz. The central frequency for these bursts decreases down to 70 kHz before the next sawtooth, while downward chirps appear below the burst frequencies, Fig. 5.12 at $t = 24, 25, 25.5$ ms. The time between bursts is short, ≈ 100 μs. After 4 ms from the last sawtooth crash, $n = 6$ bursts appear with $f_{n=6} \approx 110 - 130$ kHz, whose peaks are interleaved with $n = 5$ peaks at spacings of 40-50 μs. Very late in time, (28.5 ms), $n = 5$ bursts at the $n = 6$ frequency appear along with $n = 6$ bursts.The $n = 4$ bursts appear coincidentally with the $n = 5$ bursts as in the base case, but less often, at higher frequencies and at lower amplitudes.

Although the initial $n = 5$ bursts appear in rapid succession, only 1 burst per sawtooth cycle reaches the same amplitude of $\tilde{B}_{\theta,n=5} = 1.7$ G as in the base case. The $n = 6$ bursts have amplitude $\tilde{B}_{\theta,n=6} < 1$ G. The $n = 4$ bursts have a similar

Figure 5.12: Wavelet spectrograms of $n = 5$ and $n = 6$ bursts in a standard plasma. As q evolves, the $n = 5$ bursts begin to downchirp, and $n = 6$ bursts appear at 130 kHz.

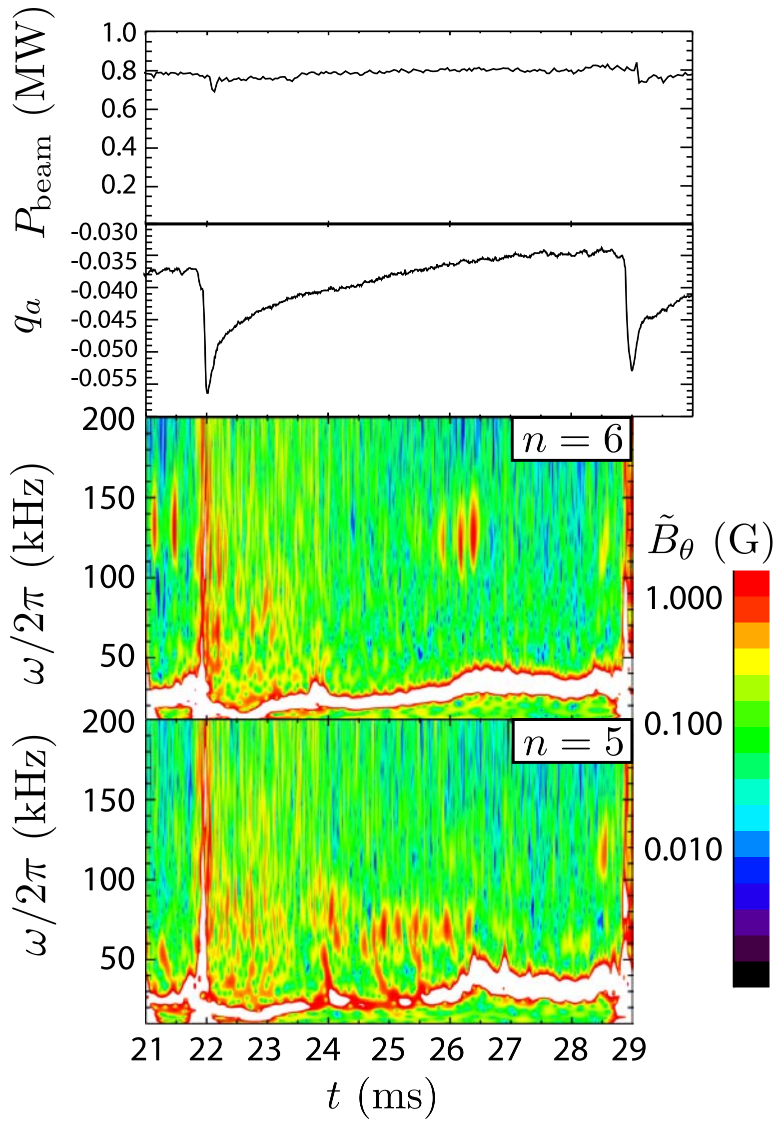

amplitude, $\tilde{B}_{\theta,n=4} < 1$ G, although their decreased prevalence suggests that they are at the margin of critical drive for instability.

Significantly more data was gathered with non-reversed plasmas than reversed plasmas. Nonetheless, the standard plasmas add some pieces of evidence for mode identification. The changing value of q_0 and q_a across the sawtooth cycle evidently

Figure 5.13: Continuum calculation with crossing of the $n = 4$, $n = 5$ and $n = 6$ modes marked. Resonant locations change significantly throughout the sawtooth cycle.

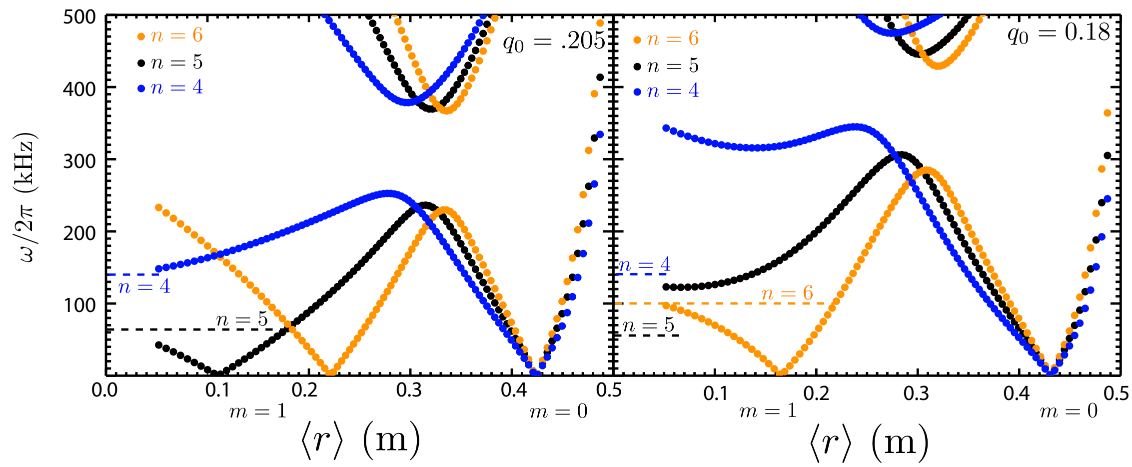

affects the modes. Initially, the $n = 5$ bursts occur at higher frequency. This behavior is in line with the picture presented for the base case, where the steepest gradient point has changed minimally but the Alfvén continuum has changed, Fig. 5.10 and Fig. 5.13. The zero point for the Alfvén continuum disappears with the $q = 0.2$ surface, so the $m = 1$ branch starts at higher frequency. Halfway through the cycle, the $n = 5$ bursts are followed by downward chirping, implying that their activity has become non-resonant. The $n = 6$ bursts come into resonance later in the sawtooth cycle, always appearing after q has decreased substantially from its value just after the sawtooth. As q decreases, the zero point and thus the $m = 1$ branch move closer to the core. Both behaviors can be explained by a $k_{\parallel fi}$ change for the beam ions, where $q_{fi} \propto q$ is changing across the sawtooth cycle, affecting ω_{res} and the resonant mode numbers.

5.2.3 Deeply Reversed Plasmas

Several effects that are relevant to bursting modes occur throughout the duration of PPCD. The edge safety factor decreases steadily from $q_a = -.04$ to $q_a < -.12$. The density n_e rises throughout PPCD, and the density profile becomes peaked in the core. The temperature T_e likewise increases steadily.

A typical deeply reversed shot with plasma parameters is shown from 10 to 25 ms, Fig. 5.14, during which the NBI is firing at full power. The Alfvén continuum for a deeply reversed plasma was shown in Fig. 4.11. Both $n = 5$ and $n = 6$ bursts appear, although they appear at low amplitude, $\tilde{B} \approx 0.1 - 0.2$ G. The downchirping $n = 5$ behavior from standard plasmas is present at the beginning of the PPCD period, but dies away and is replaced with a 160 kHz $n = 5$ mode at constant frequency. Low amplitude $n = 6$ bursts appear at 130 kHz, decreasing to 110 kHz throughout the duration. The $n = 6$ bursts begin to downchirp as well.

Although q_a is changing rapidly, q_0 is changing slowly, and thus $k_\parallel$ at the point of steepest fast ion pressure gradient is also changing slowly. The low amplitude and time-varying behavior of these modes makes ensemble analysis difficult with internal diagnostics. It is possible that because the burst modes are global but are not eigenmodes of the plasma, the increased shear from a steeper q profile has a weakening effect on the edge amplitudes. It is a notable result that burst modes, like the $n > 6$ tearing modes, are weaker during the PPCD period.

5.2.4 Helical Plasmas

EPMs have been seen on stellarators with NBI in the past [15]. Comparison to RFPs that have transitioned to a helical state is desired, and indeed RFX has found AEs that show no change during helical discharges [68]. However, bursting modes

Figure 5.14: Wavelet spectrograms of $n = 5$ and $n = 6$ bursts in a deeply reversed plasma. The bursts are weaker than in the standard and non-reversed cases.

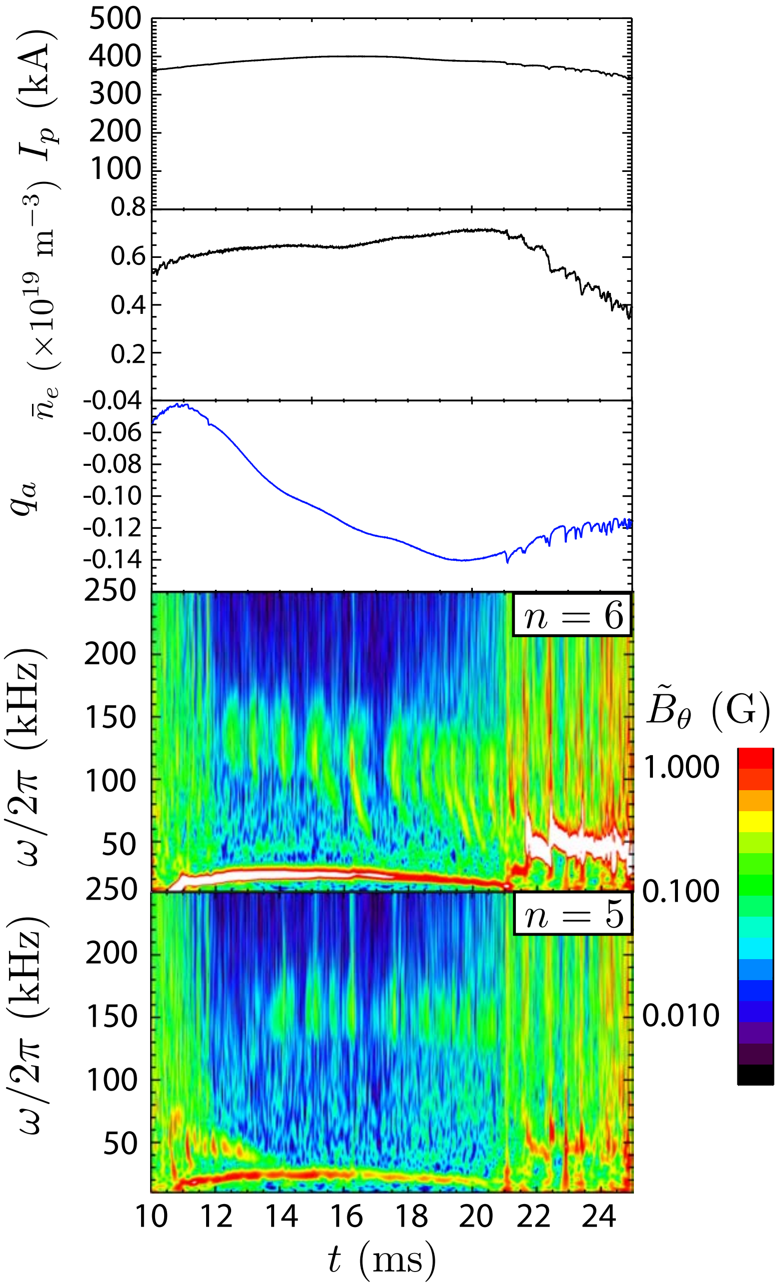

Figure 5.15: Fast ion confinement time vs. the helical mode amplitude. Image provided by Jay Anderson.

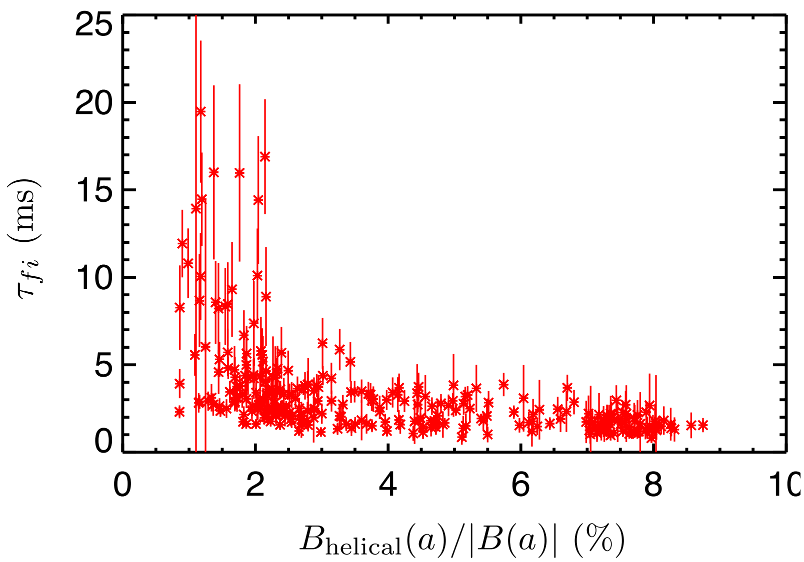

that persist throughout the duration of the SHAx state have not been seen on MST. The likely explanation for this behavior is that the fast ion confinement time drops significantly after the transition to SHAx, Fig. 5.15, as observed using the neutron detector. If the population of fast ions is not confined well in the core of the plasma, no fast ion pressure gradient exists to drive the EPMs.

Although no burst modes persist through the SHAx state, the $n = 5$ burst behavior changes as the plasma transitions. A typical shot with $I_p = 500$ kA, $q_a = 0$, from 20 to 30 ms is shown here Fig. 5.16, with the addition of a plot of the $n = 5$ tearing mode amplitude over time. As the helical axis develops, the $n = 5$ bursts increase in frequency before they are suppressed at SHAx onset. The $n = 4$ and $n = 5$ bursts disappear throughout the SHAx duration. However, as shown in Fig. 5.15, the fast ion confinement time is decreased substantially, changing the fast ion content and thus the fast ion gradient.

As shown in Fig. 4.18, the coremost $n = 5, m = 1$ branch of the Alfvén continuum rises in frequency up to 450 kHz in the helical equilibrium. The bursts do not scale

Figure 5.16: Wavelet spectrogram of $n = 5$ bursts in a plasma transitioning into SHAx. Bursts increase in frequency and weaken before terminating at SHAx onset.

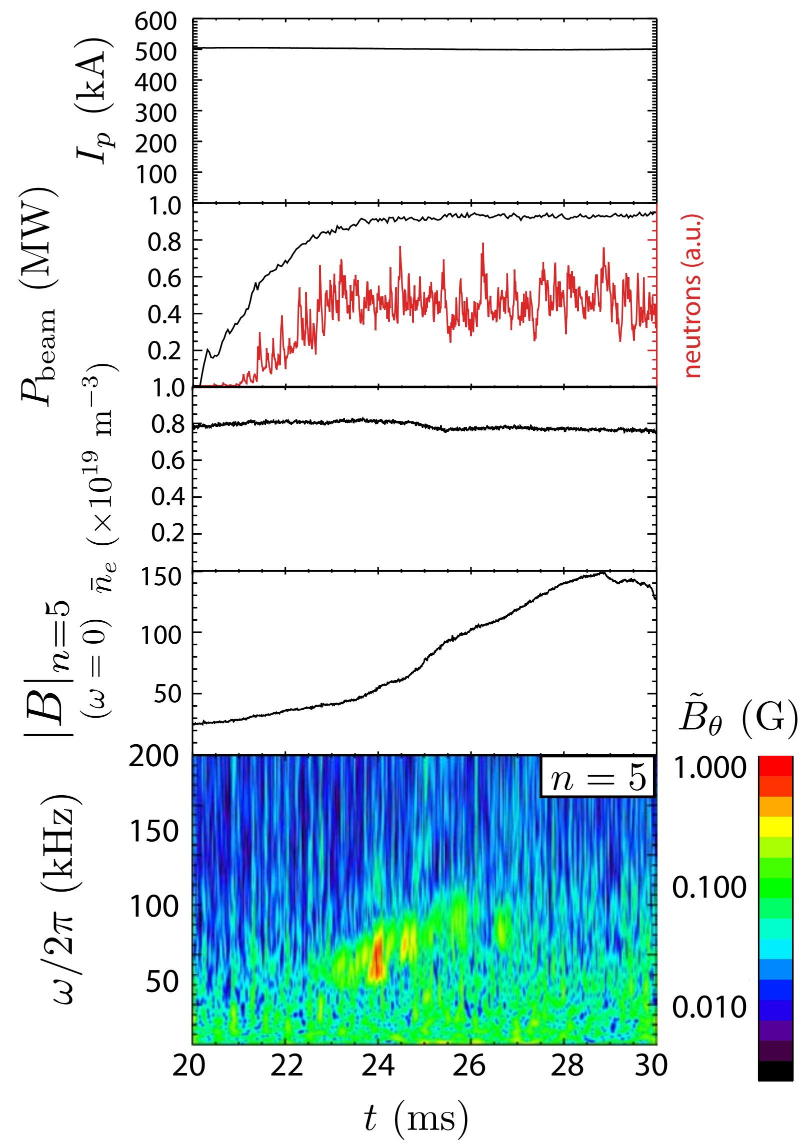

with magnetic field and scale only weakly with density, so the likely mechanism of frequency change is a modification to $k_{\|}$ caused by the helical shift of the magnetic axis. The rapid change to the q profile and the resonant surface could explain the change in $f_{n=5}$ during SHAx onset. Accurate modeling of the fast ion profile through the transition has not been done, as the magnetic fields are decreasing in stochasticity and shifting helically over time. Including fast ion deposition from NBI in this complex scenario has yet to be tackled with computation.

5.3 Macroscopic Effects on MST Plasmas

The observed EPMs have one important effect on MST plasmas: they redistribute fast ions. The beam-injected ions increase the coremost tearing mode rotation and decrease the coremost mode amplitude measured on edge magnetics, so fast ion redistribution couples secondarily to tearing mode suppression. The ANPA, described in Sec. 2.2.3 measures high pitch fast ion content in the plasma core, but no other measures of the fast ion distribution function are utilized on MST at present. An external neutron detector is used as a proxy for total fast ion content.

During neutral beam injection, the phase velocity v_ϕ of the tearing modes is increased, Fig. 5.17. This enhancement is reversed when the beam is injected counter to I_p (which sets the tearing mode rotation direction), implying that continuous injection of ions applies a torque in the direction of injection. The core tearing mode amplitude measured by the magnetic coils, $\tilde{B}_{\theta\,\mathrm{r.m.s.}}$, decreases at the same time. Preliminary theoretical work suggests that the injected ions act as a parallel current in the core of the plasma, driving down q_0 and decreasing the width over which the coremost tearing mode is resonant. The neutron flux approximates the fast ion content of the plasma, and both mode suppression and rotation enhancement scale

Figure 5.17: Core tearing mode ($n = 5$) amplitude and velocity during NBI. Image provided by Jay Anderson.

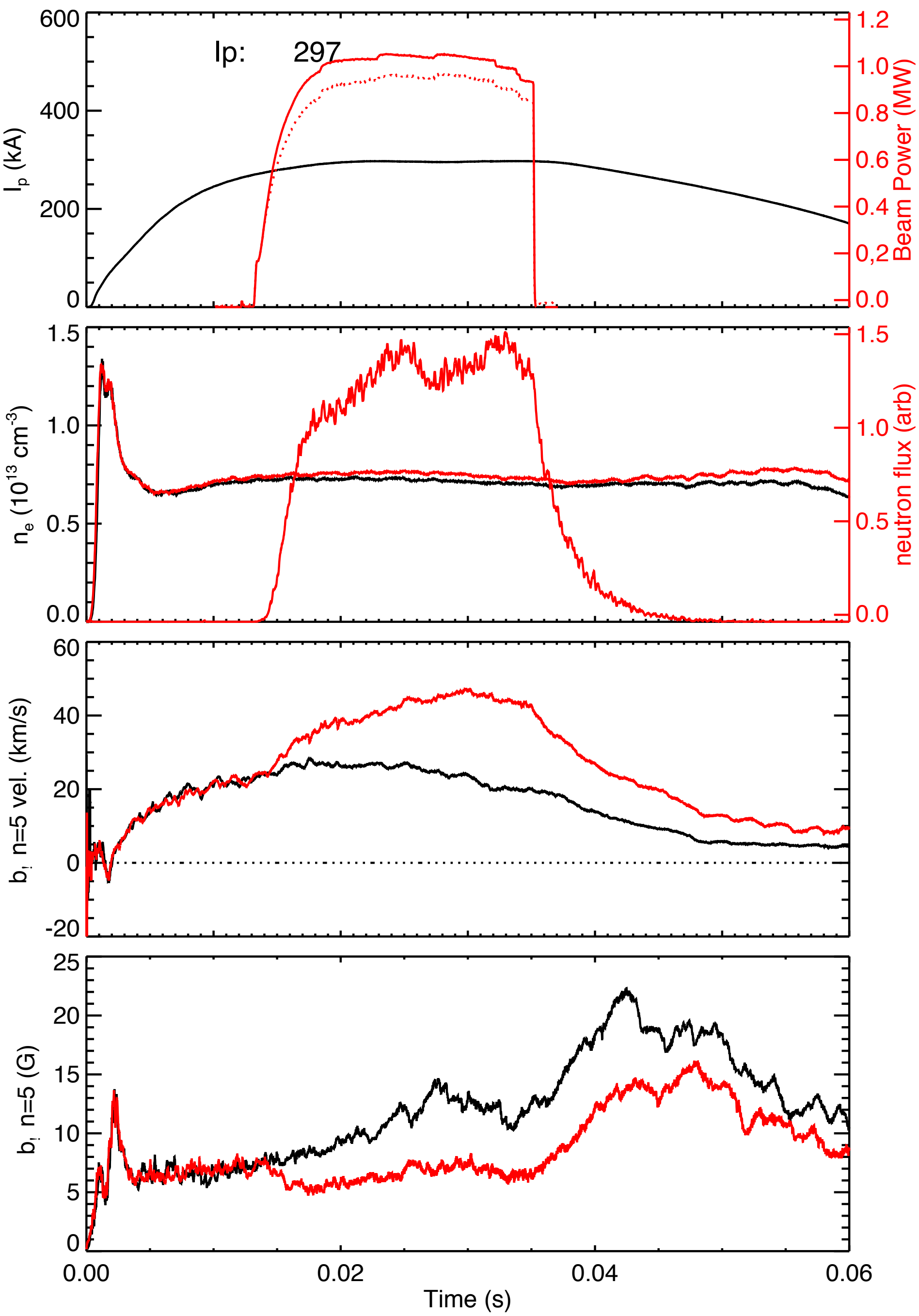

Figure 5.18: Bicoherence, ANPA signal and tearing mode amplitude for a burst ensemble. The $n = 5$ tearing mode suppression decreases during the bursts as the ANPA signal drops. From [69]

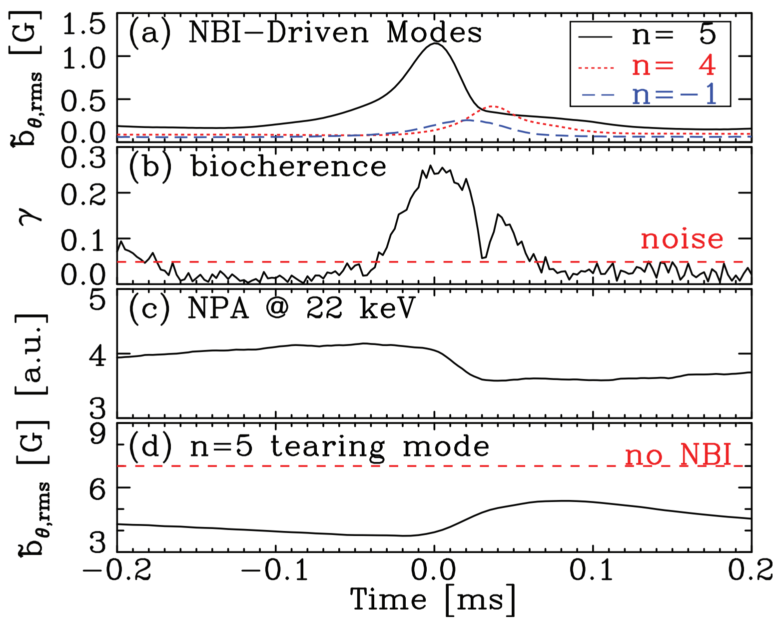

with the neutron flux.

An ensemble of 1000 bursts was performed by the FIR Interferometry-Polarimetry group, Fig. 5.18. The r.m.s. amplitude of the $n = 5$, $n = 4$ and $n = -1$ bursts was compared with the ANPA measurement of 22 keV high-$v_{\|}$ fast ions and the r.m.s. amplitude of the coremost tearing mode. The bicoherence of the three burst modes is also plotted. At the point when bicoherence peaks, the ANPA signal drops and tearing mode suppression is relaxed. The coincident effects indicate that fast ion redistribution, the coupling of several EPMs, and the reduction in tearing mode suppression are linked. The coupling of $n = 4$ and $n = 5$ is the primary coupling, allowing ions to be convected outward from the core. The $n = 1$ likely energizes as a result of that coupling.

The burst cycle repeats as the high pitch passing fast ion density builds up again in the core. The plasma rotation and tearing mode amplitude flatten after a period

Figure 5.19: Comparison of beam currents to burst amplitudes, neutron signal, ANPA signal, and tearing mode suppression. From [70]

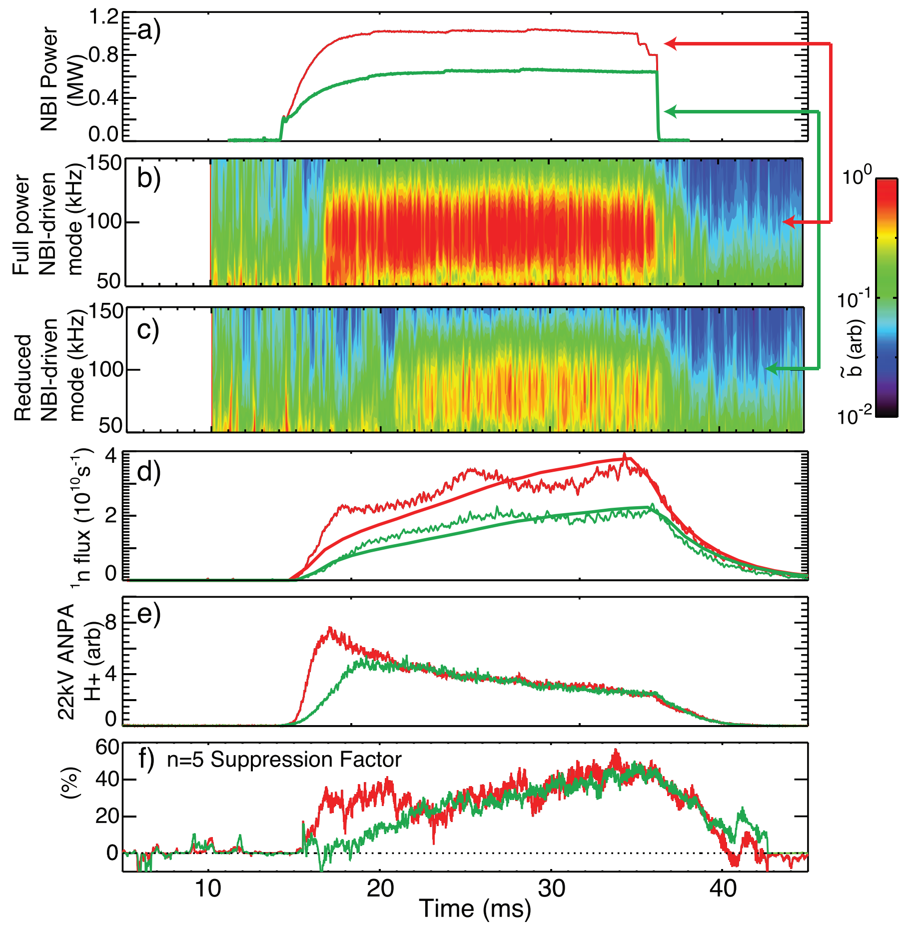

of time set by the beam current, Fig. 5.19. The neutron signals and core-localized 22 keV ions asymptotically approach steady-state values[70]. While the ANPA H+ signal measures the core-localized fast hydrogen ions, the neutron signal measures total deuterium content. It is evident that the small amount of injected fast deuterium (3%) asymptotically approaches a maximum while the on-axis hydrogen content asymptotes to a minimum. While the total fast ion content may be increasing, the ions deposited on-axis are being redistributed to different pitches and radii. The fast ion population and EPMs form a limit cycle that constrains the shape of the fast ion distribution function. The tearing mode amplitude is set by a competition between the suppression from fast ions and the drive from current on axis. The flattening of the rotation speed likely also requires eddy currents in the conducting shell to complete the picture. The continuous torque from the beam allows the rotation to exceed the "normal" maximum set by braking from eddy currents [71].

5.4 Internal Characteristics

The internal measurements taken by the FIR Interferometry-Polarimetry group complete the known picture of the EPMs at the time of writing. The interferometer resolves $\tilde{n}_e(R)$ along its 11 chords, giving a picture of the structure of density fluctuations associated with the burst mode. The polarimeter measures the fluctuations in Faraday rotation $\tilde{\Psi}(R)$ due to vertical magnetic field perturbations. 1000 events are ensembled together from correlation with the magnetic coils to produce plots of $\tilde{n}_e(R)$ and $\tilde{\Psi}(R)$.

The line-averaged values for $\tilde{n}_e(R)$ and $\tilde{\Psi}(R)$ of the ensembled $n = 5$ bursts are shown in Fig. 5.20. Both $\tilde{n}_e$ and $\tilde{\Psi}$ peak in the core, inboard of the magnetic axis. The asymmetry in density is similar to the asymmetry seen on TFTR[72], where a smaller multi-chord interferometer measured fast ion-driven TAE modes excited in the afterglow of beam injection. In that case, the magnetic fluctuations were symmetric about the axis. In the MST case, both magnetic and density fluctuations are asymmetric. From the $R - R_0 = -0.32$ m location, the estimated chord averaged burst magnetic amplitude has a lower bound of $\tilde{b}_z > 0.6$ G, roughly consistent with the point-measured amplitude at the magnetic coils of $\tilde{b}_{z,\mathrm{rms}} = \tilde{B}_{\theta,\mathrm{peak}}(a)\cos(241^\circ)/\sqrt{2} = 0.6$ G. In the core, $\tilde{n}_e = 0.3 \times 10^{17}$ m^{-3} is expected to be dominantly compressional, switching to advection in the edge where the phase between $\tilde{n}_e$ and $\tilde{\Psi}$ changes sign. The phase flip of perturbations through the core confirms the $m = 1$ character ob-

Figure 5.20: Interferometry and Polarimetry measurements of the $n = 5$ mode structure. From [69]

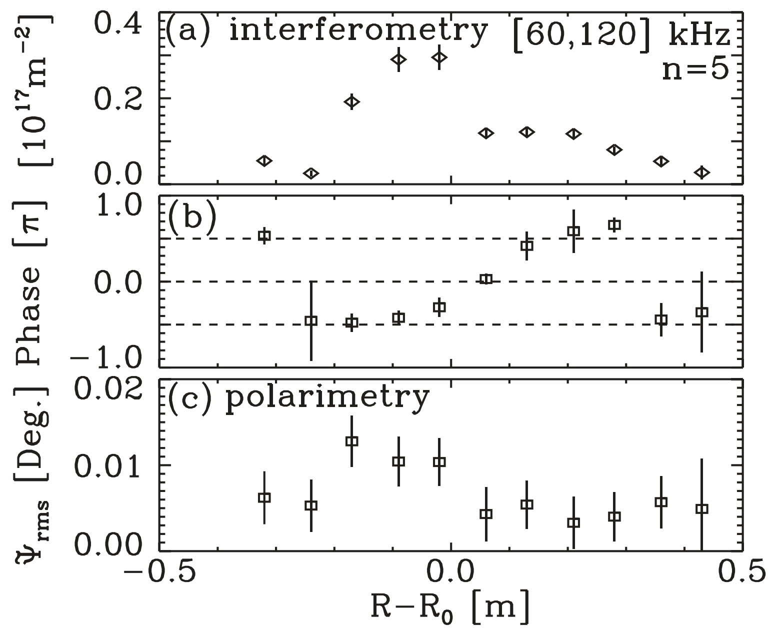

served by magnetics.

Although the $n = 4$ and $n = -1$ bursts are not large enough to resolve internal magnetic perturbations, their density perturbations for all the burst modes are resolvable. The $\tilde{n}_e$ amplitude is plotted as a function of time and $R - R_0$, Fig. 5.21. The $n = 5$ mode has the same radial resonance as shown in Fig. 5.9 ($\sim$ 15 cm), with its peak at $R - R_0 \approx -12$ cm from the magnetic axis. The $n = -1$ mode is asymmetrically outboard at $R - R_0 = +18$ cm slightly later in time, mirroring the $n = 5$. Finally, the $n = 4$ appears in the core with a less pronounced outboard asymmetry of $R - R_0 = +7$ cm.

The internal measurements support the distribution function depletion picture presented earlier, Fig. 5.10, but generate new questions. The strongest perturbations to both $\tilde{n}_e$ and $\tilde{b}_z$ are located in the core, confirming it as the location of resonance. The $n = 5$ mode is located farther from the core, as in the continuum picture. As

Figure 5.21: Interferometry measurements of the asymmetry of $n = 5$, $n = 4$ and $n = -1$ in time. From [69]

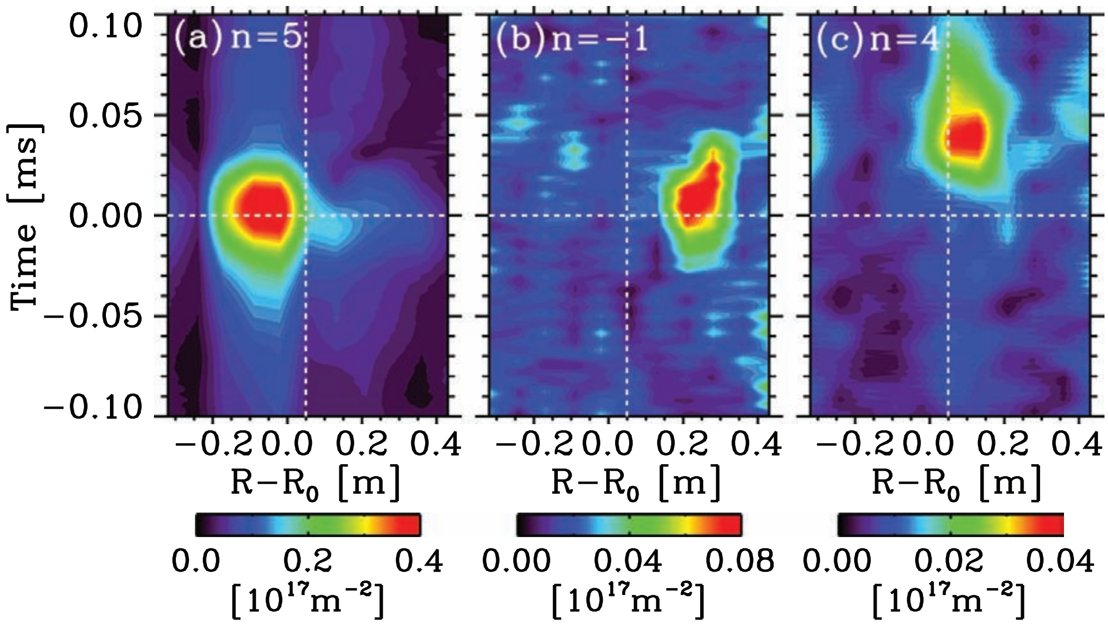

it depletes fast ions, the beam ion pressure gradient steepens, exciting the $n = 4$ and $n = -1$ modes. The asymmetry of both $n = 5$ and $n = 4$ modes is as of yet unexplained.

5.5 Summary

Spatial Fourier decomposition is used to generate $\dot{B}(t)$ with $n = 0 - 15$ signals for $\dot{B}_\theta$ and $m = 0 - 3$ signals for $\dot{B}_\theta$ and $\dot{B}_\phi$. Wavelet transforms are performed on these time traces to obtain $\mathbf{B}_[\tau, \langle f \rangle_s]$ maps for each $\dot{B}$ signal, using the wavelet-determined frequencies to separate $\dot{\tilde{B}} = \omega \tilde{B}$. An event-tagging routine identifies EPM bursts and tags them for ensemble analysis.

A large number of scenarios have been analyzed for non-reversed plasmas. Bursts with $n = 5$ appear regularly during NBI, each followed by an $n = 4$ burst ≈ 40 μs later. The $n = 5$ bursts scale with beam ion velocity v_B while the $n = 4$ bursts scale with v_A. The $n = 5$ bursts have poloidal mode number $m = 1, 0$, $\tilde{B} \approx 2$ G, and Doppler-shifted $f = 90$ kHz. The $n = 4$ bursts have poloidal mode number $m = 1$, $\tilde{B} \approx 0.5$ G, and Doppler-shifted $f = 140$ kHz. The altered q and n_e profiles in standard and deeply reversed plasmas bring the $n = 6$ modes into resonance while retaining the $n = 5$ modes. The bursts move to higher frequency during the transition to SHAx, and terminate before the SHAx flat-top period.

Core tearing mode amplitudes are reduced by the presence of beam ions, while tearing mode rotation is enhanced. ANPA data confirms that fast ions are redistributed or lost at each burst, reducing tearing mode suppression. The $n = 5$ and $n = 4$ bursts have different spatial localizations, and energize the $n = -1$ through 3-wave coupling. The overall behavior supports a picture whereby the distribution function of fast ions is peaked in the core with large fast ion pressure gradient. This gradient destabilizes the $n = 5$, which redistributes ions, enhancing the gradient in the core. This enhancement subsequently destabilizes the $n = 4$.

Chapter 6

Conclusion

This work has presented the first observation of beam-driven instabilities in Madison Symmetric Torus, a reversed-field pinch. Examination of the characteristics of the observed modes was informed by the generation of Alfvén continua and eigenmode solutions for a variety of plasmas, including those with a helical axis. A crucial component of that endeavor was the adaptation of stellarator equilibrium solution and Alfvén mode calculation routines for use on the RFP. Current and future work relies heavily on the extensive diagnostic suite available on MST, which has been catalogued and assessed for its viability both for the generation of equilibria and for observing Alfvénic-frequency magnetic fluctuations.

The observed bursts were evidently not Alfvén eigenmodes, as their frequencies are far too low to match the frequencies for gaps in the Alfvén continuum. The case is made that they are energetic particle modes resulting from a fast ion density gradient due to neutral beam injection. Although the distribution function cannot be measured exactly, the dependence of burst frequencies on the resonant locations of the Alfvén continuum is strong evidence for fast-ion-determined resonance. Additionally, the picture of resonant mode appearing at steep points in the distribution function, and subsequently flattening it, corresponds with the clustered multiple-n bursts robustly observed. The apparent Alfvénic scaling of the highest-frequency mode may be explained by a competition of damping and drive, although the possibility is open for it to be an AE. The internal characteristics of the bursts and the plasma reaction to them give credence to this picture.

This work is relevant both to fusion science and to RFP science because particle-wave instabilities are an inevitability with neutral beam injection or fusion products. The high shear of the RFP raised questions about whether beam-driven instabilities could appear, but indeed they have. Both beams and fusion reactions will create a core-localized population of fast ions that can drive instability, ejecting the fast ions themselves and limiting the total population of fast particles in the device. The observed EPMs are not only a consideration for all discussions of fusion RFPs and NBI on the RFP, but they will also be the primary focus of many experimental and computational studies in the future.

Future Work

The primary necessity in pushing the understanding of the EPMs further is an adequate modeling code for the wave-particle interaction. Hybrid kinetic-MHD codes exist and have been used in the past to model this interaction. Examples are MH3D[73], MEGA[74], GYRO, GENE, NIMROD[75] and TAEFL[76]. Several of them suffer from previously-mentioned issues because they function in toroidal flux. Several attempts have been made to entice the developers of these codes to tackle the RFP problem, but advances have been slow to-date. The work of adapting and applying such a code to the observed EPMs is the logical next step. A full orbit code is also under development to determine the characteristic frequencies of particles injected by the neutral beam. It is planned to be coupled to beam deposition modeling in order to describe the expected fast particle population and resonances.

Measurement efforts to include $\tilde{T}_e$ and $\tilde{\phi}$ in the picture of the EPM bursts are underway. A full-diagnostic campaign to accurately diagnose the bursts using all terms indicated in 2.3 should be undertaken. Greater resolution or the inclusion of new diagnostics for internal measurements will also clarify the picture further. Finally, an advanced diagnostic to measure the distribution function such as FIDA[77] would greatly aid determination of the instability drive.

AE3D and Stellgap are close to handling the reversal surface. The last iteration included an additional pressure term and handled the reversal surface correctly, but contained a bug that introduced a periodic variation into its eigenmode structures, rendering it unusable. The amelioration of that issue should result in an answer to the question of whether eigenmodes couple across the reversal surface.

V3FIT reconstruction is continually improving. It will be benchmarked against MSTFIT equilibria in the near term. The process of determining initial conditions for each reconstruction is also currently being refined. Accurate modeling of the conducting shell within V3FIT is also underway so that the reconstruction can be freed from MSTFIT inputs.

Bibliography

[1] M. Zarnstorff, M. Bell, M. Bitter, R. Goldston, B. Grek, R. Hawryluk, K. Hill, D. Johnson, D. McCune, H. Park, A. Ramsey, G. Taylor, and R. Wieland, Physical Review Letters **60**, 1306 (1988).

[2] J. B. Taylor, Physical Review Letters **33**, 1139 (1974).

[3] D. Jassby, Nuclear Fusion **17**, 309 (1977).

[4] J. K. Anderson, A. Almagri, B. Chapman, V. Davydenko, P. Deichuli, D. D. Hartog, C. Forest, G. Fiksel, A. Ivanov, D. Liu, M. Nornberg, J. Sarff, N. Stupishin, and J. Waksman, Transactions of Fusion Science and Technology **59**, 27 (2011).

[5] K. Wong, Plasma Physics and Controlled Fusion **41**, R1 (1999).

[6] W. Heidbrink, Physics of Plasmas **15**, 055501 (2008).

[7] J. Berkowitz, H. Grad, and H. Rubin, (1958).

[8] K. Miyamoto, *Controlled Fusion and Plasma Physics* (Taylor and Francis, 2007).

[9] V. D. Shafranov, Journal of Nuclear Energy: Plasma Physics **5** (1963).

[10] K. Harafuji, T. Hayashi, and T. Sato, Journal of Computational Physics **81**, 169 (1989).

[11] H. Alfvén, Nature **150**, 406 (1942).

[12] W. Heidbrink, E. Strait, E. Doyle, G. Sager, and R. Snider, Nuclear Fusion **31**, 1635 (1991).

[13] K. Wong, R. Fonck, S. Paul, D. Roberts, E. Fredrickson, R. Nazikian, H. Park, and M. Bell, Physical Review Letters **66**, 1874 (1991).

[14] E. Fredrickson, N. Gorelenkov, R. Bell, J. Menard, A. Roquemore, S. Kubota, N. Crocker, and W. Peebles, Nuclear Fusion **46**, S926 (2006).

[15] K. Toi, K. Ogawa, M. Isobe, M. Osakabe, D. Spong, and Y. Todo, Plasma Physics and Controlled Fusion **53**, 024008 (2011).

[16] R. Dexter, D. Kerst, T. Lovell, S. Prager, and J. Sprott, Fusion Technology **19**, 131 (1991).

[17] T. Biewer, C. Forest, J. Anderson, G. Fiksel, B. Hudson, S. Prager, J. Sarff, and J. Wright, Physical Review Letters **91**, 045004 (2003).

[18] J. J. Koliner, Physical Review Letters **109**, 115003 (2012).

[19] G. Fiksel, B. Hudson, D. D. Hartog, R. Magee, R. O'Connell, and S. Prager, Physical Review Letters **95**, 125001 (2005).

[20] S. Assadi, *Measurement of Magnetic Turbulence Structure and Nonlinear Mode Coupling of Tearing Fluctuations in the Madison Symetric Torus Reverse Field Pinch Edge*, Ph.D. thesis, UW-Madison (1992).

[21] H. Nyquist, Transactions in AIEE **47**, 617 (1928).

[22] C. Rader and N. Brenner, IEEE Transactions in Acoustics, Speech and Signal Processing **24**, 264 (1976).

[23] A. Hansen, *Kinematics of Nonlinearly Interacting MHD Instabilities in a Plasma*, Ph.D. thesis, UW-Madison (2000).

[24] J. Anderson, *Measurement of the Electrical Resistivity Profile of the Madison Symmetric Torus*, Ph.D. thesis, UW-Madison (2001).

[25] J. King, *First-order finite-Larmor-radius effects on magnetic tearing and relaxation in pinch configurations*, Ph.D. thesis, UW-Madison (2011).

[26] T. Tharp, *Measurements of Nonlinear Hall-Driven Reconnection in the Reversed Field Pinch*, Ph.D. thesis, UW-Madison (2010).

[27] H. Stephens, *Electron Temperature Structures Associated With Magnetic Tearing Modes in the Madison Symmetric Toru*, Ph.D. thesis, UW-Madison (2010).

[28] M. McGarry, *PROBING THE RELATIONSHIP BETWEEN MAGNETIC AND TEMPERATURE STRUCTURES WITH SOFT X-RAYS ON THE MADISON SYMMETRIC TORUS*, Ph.D. thesis, UW-Madison (2013).

[29] R. Lorenzini, F. Auriemma, A. Canton, and L. Carraro, Physics of Plasmas (2006).

[30] S. Eilerman, J. Anderson, J. Reusch, D. Liu, and G. Fiksel, Review of Scientific Instruments **83**, 10D302 (2012).

[31] D. Brower, W. Ding, S. Terry, J. Anderson, and T. Biewer, Review of Scientific Instruments (2003).

[32] J. Reusch, *Measured and Simulated Electron Thermal Transport in the Madison Symmetric Torus Reversed Field Pinch*, Ph.D. thesis, UW-Madison (2011).

[33] R. Magee, *Ion energization during tearing mode magnetic reconnection in a high temperature plasma*, Ph.D. thesis, UW-Madison (2011).

[34] D. Craig, D. D. Hartog, G. Fiksel, V. Davydenko, and A. Ivanov, Review of Scientific Instruments **72**, 1008 (2001).

[35] S. Kumar, A. Almagri, D. Craig, D. D. Hartog, and M. Nornberg, Physics of Plasmas **20**, 056501 (2013).

[36] L. Lao, H. S. John, Q. Peng, J. Ferron, W. Meyer, E. Strait, T. Taylor, K. You, and C. Zhang, (2005).

[37] J. Ko and J. Klabacha, Review of Scientific Instruments **83**, 10D513 (2012).

[38] J. Reardon, G. Fiksel, C. Forest, A. Abdrashitov, V. Davydenko, A. Ivanov, S. Korepanov, S. Murachtin, and G. Shulzhenko, Review of Scientific Instruments **72**, 598 (2001).

[39] J. Waksman, *NEUTRAL BEAM HEATING OF A REVERSED-FIELD PINCH IN THE MADISON SYMMETRIC TORUS*, Ph.D. thesis, UW-Madison (2013).

[40] J. Lei, D. Demers, K. Connor, and P. Schoch, Review of Scientific Instruments **72**, 564 (2001).

[41] A. Melnikov, L. Eliseev, R. Jiménez-Gómez, E. Ascasibar, C. Hidalgo, A. Chmyga, and A. Komarov, Nuclear Fusion **50**, 084023 (2010).

[42] S. Hirshman and P. Merkel, Computer Physics Communications **43**, 143 (1986).

[43] S. Lazerson and I. Chapman, Plasma Physics and Controlled Fusion **55**, 044004 (2013).

[44] J. Hanson, S. Hirshman, S. Knowlton, L. Lao, E. Lazarus, and J. Shields, Nuclear Fusion **49**, 075031 (2009).

[45] P. Moroz, Physical Review Letters **77**, 651 (1996).

[46] W. Cooper, J. Graves, and A. Pochelon, Physical Review Letters **105**, 035003 (2010).

[47] M. Gobbin, D. Bonfiglio, A. Boozer, A. Cooper, D. Escande, S. Hirshman, J. Lore, R. Lorenzini, L. Marrelli, P. Martin, E. Martines, B. Momo, N. Pomphrey, I. Predebon, M. Puiatti, R. Sanchez, G. Spizzo, D. Spong, and D. Terranova, Physics of Plasmas **18**, 062505 (2011).

[48] P. Martin, L. Marrelli, G. Spizzo, P. Franz, P. Piovesan, I. Predebon, T. Bolzonella, S. Cappello, and A. Cravotta, Nuclear Fusion **43**, 1855 (2003).

[49] D. Spong, R. Sanchez, and A. Weller, Physics of Plasmas **10**, 3217 (2003).

[50] D. Spong, E. D'Azevedo, and Y. Todo, Physics of Plasmas **17**, 022106 (2010).

[51] A. Salat and J. Tataronis, Physics of Plasmas **8**, 1200 (2001).

[52] S. Kruger, C. Hegna, and J. Callen, University of Wisconsin Center for Plasma Theory and Computation Report (1998).

[53] D. Terranova, D. Bonfiglio, A. Boozer, A. Cooper, M. Gobbin, and S. Hirshman, Plasma Physics and Controlled Fusion **52**, 124023 (2010).

[54] F. Auriemma, P. Zanca, W. Bergerson, B. Chapman, W. Ding, D. Brower, P. Franz, P. Innocente, R. Lorenzini, B. Momo, and D. Terranova, Plasma Physics and Controlled Fusion **53**, 105006 (2011).

[55] W. Bergerson, F. Auriemma, B. Chapman, W. X. Ding, P. Zanca, D. Brower, P. Innocente, L. Lin, R. Lorenzini, E. Martines, B. Momo, J. Sarff, and D. Terranova, Physical Review Letters **107**, 255001 (2011).

[56] P. Zanca and D. Terranova, Plasma Physics and Controlled Fusion **46**, 1115 (2004).

[57] E. Martines, R. Lorenzini, B. Momo, D. Terranova, P. Zanca, A. Alfier, F. Bonomo, A. Canton, A. Fassina, P. Franz, and P. Innocente, Plasma Physics and Controlled Fusion **53**, 035015 (2011).

[58] L. Carraro, P. Innocente, F. Auriemma, R. Cavazzana, A. Fassina, P. Franz, M. Gobbin, I. Predebon, A. Ruzzon, G. Spizzo, D. Terranova, T. Bolzonella, A. Canton, S. D. Bello, L. Grando, R. Lorenzini, L. Marrelli, E. Martines, M. Puiatti, P. Scarin, L. Carraro, P. Innocente, F. Auriemma, R. Cavazzana, A. Fassina, A. Soppelsa, M. Valisa, L. Zanotto, and M. Zuin, Nuclear Fusion **53**, 073048 (2013).

[59] D. Terranova, L. Marrelli, J. Hanson, S. Hirshman, M. Cianciosa, and P. Franz, Nuclear Fusion **53**, 113014 (2013).

[60] B. Chapman, J. Anderson, T. Biewer, D. Brower, S. Castillo, P. Chattopadhyay, C. Chiang, D. Craig, D. D. Hartog, G. Fiksel, P. Fontana, C. Forest, S. Gerhardt, A. Hansen, D. Holly, Y. Jiang, N. Lanier, S. Prager, J. C. Reardon, and J. Sarff, Physical Review Letters **87**, 205001 (2001).

[61] W. Ding, D. Brower, B. Deng, A. Almagri, D. Craig, G. Fiksel, V. Mirnov, and S. Prager, Physics of Plasmas **13**, 112306 (2006).

[62] C. Torrence and G. Compo, Bulletin of the American Metereological Society (1997).

[63] R. Yan and R. Gao, IEEE Instrumentation and Measurement Magazine , 35 (2009).

[64] L. Chen, R. White, and M. Rosenbluth, Physical Review Letters **52**, 1122 (1984).

[65] W. Heidbrink, M. V. Zeeland, M. Austin, K. Burrell, N. Gorelenkov, G. Kramer, Y. Luo, M. Makowski, G. McKee, C. Muscatello, R. Nazikian, E. Ruskov, W. Solomon, R. White, and Y. Zhu, Nuclear Fusion **48**, 084001 (2008).

[66] N. Gorelenkov, M. V. Zeeland, H. Berk, N. Crocker, and D. Darrow, Physics of Plasmas **16**, 056107 (2009).

[67] W. Chen, X. Ding, Q. Yang, X. Ji, and Y. Zhang, Physical Review Letters **105**, 185004 (2010).

[68] S. Spagnolo, M. Zuin, F. Auriemma, R. Cavazzana, E. Martines, M. Spolaore, and N. Vianello, Nuclear Fusion **51**, 083038 (2011).

[69] L. Lin, W. Ding, D. Brower, J. Koliner, S. Eilerman, J. Reusch, J. Anderson, M. Nornberg, J. Sarff, J. Waksman, and D. Liu, Physics of Plasmas **20**, 030701 (2013).

[70] J. K. Anderson, A. Almagri, D. D. Hartog, S. Eilerman, C. Forest, J. J. Koliner, V. V. Mirnov, L. Morton, M. Nornberg, E. Parke, J. Reusch, J. Sarff, J. Waksman, V. Belykh, V. Davydenko, A. Ivanov, S. Polosatkin, Y. Tsidulko, L. Lin, D. Liu, G. Fiksel, H. Sakakita, D. Spong, and J. Titus, Physics of Plasmas **20**, 056102 (2013).

[71] B. Chapman, R. Fitzpatrick, D. Craig, P. Martin, and G. Spizzo, Physics of Plasmas **11**, 2156 (2004).

[72] R. Nazikian, G. Kramer, Z. Cheng, N. Gorelenkov, H. Berk, and S. Sharapov, Physical Review Letters **91**, 125003 (2003).

[73] L. Sugiyama and W. Park, Physics of Plasmas **7**, 4644 (2000).

[74] Y. Todo, K. Shinohara, M. Takechi, and M. Ishikawa, Physics of Plasmas **12**, 012503 (2005).

[75] C. Kim, Journal of Fusion Energy **27**, 61 (2008).

[76] D. Spong, E. Bass, W. Deng, W. Heidbrink, Z. Lin, B. Tobias, M. V. Zeeland, M. Austin, C. Domier, and N. Luhmann, Physics of Plasmas **19**, 082511 (2012).

[77] C. Muscatello, W. Heidbrink, D. Taussig, and K. Burrell, Review of Scientific Instruments **81**, 10D316 (2010).